Title

Automated Clustering of White Matter Fibers in Diffusion MRI and Voxelwise Spectral Diffusional Connectivity

Author

Jin, Yan

Publication Date

2014

Peer reviewed|Thesis/dissertation

UNIVERSITY OF CALIFORNIA

Los Angeles

Automated Clustering of White Matter Fibers in Diffusion MRI and Voxelwise Spectral Diffusional Connectivity

A dissertation submitted in partial satisfaction of the

requirements for the degree Doctor of Philosophy

in Biomedical Engineering

by

Yan Jin

2014

ABSTRACT OF THE DISSERTATION

Automated Clustering of White Matter Fibers in Diffusion MRI

and Voxelwise Spectral Diffusional Connectivity

by

Yan Jin

Doctor of Philosophy in Biomedical Engineering

University of California, Los Angeles, 2014

Professor Daniel B. Ennis, Co-Chair

Professor Paul M. Thompson, Co-Chair

To understand factors that affect brain connectivity and integrity, it is beneficial to automatically cluster white matter (WM) fibers into anatomically recognizable tracts. Whole brain tractography, based on diffusion-weighted MRI, generates vast sets of fibers throughout the brain; clustering them into consistent and recognizable bundles can be difficult as there are wide individual variations in the trajectory and shape of WM pathways. Here I propose a novel

automated tract clustering algorithm based on label fusion – a concept from traditional intensity-based segmentation. Streamline tractography generates many incorrect fibers, so this top-down approach extracts tracts consistent with known anatomy, by mapping multiple hand-labeled atlases into a new dataset. Then, I fuse clustering results from different atlases, using a mean distance fusion scheme. To compute population statistics, I develop a point-wise correspondence method to match, compare, and average WM tracts across subjects.

The complete workflow is demonstrated in two large-scale population studies. In one study, the major 17 tracts were extracted from 105-gradient high angular resolution diffusion images (HARDI) of 198 young normal twins to show the 3-D genetic heritability profile for each tract. In the other study, the fornix tracts of 210 participants were segmented from the Alzheimer's Disease Neuroimaging Initiative (ADNI) database to study its relationship with cognitive decline.

Besides studying the local connectivity with fiber clustering, I also investigate whole brain connectivity from a different perspective. Many connectivity studies parcellate the brain into regions and count fibers extracted between them. The resulting network analyses require validation of the tractography, as well as region and parameter selection. I propose a mathematical formulation based on studying the eigenvalues of the Laplacian matrix of the diffusion tensor field at the voxel level. This voxelwise matrix has over a million parameters, but I derive the Kirchhoff complexity and eigen-spectrum through elegant mathematical theorems, without heavy computation. These novel measures were used to estimate the voxelwise connectivity in multiple biomedical applications such as Alzheimer's disease and intelligence prediction.

The dissertation of Yan Jin is approved.

Ricky K. Taira

Luminita A. Vese

Yonggang Shi

Daniel B. Ennis, Committee Co-Chair

Paul M. Thompson, Committee Co-Chair

University of California, Los Angeles

2014

Dedicated to

my father JIN, Hanchen

and

my mother FENG, Wei

with love

TABLE OF CONTENTS

LIST OF FIGURES

Chapters 2. Fiber Alignment and Spectral Clustering

Chapter 3. Multi-atlas Label Fusion Clustering

Chapter 4. Genetic Heritability

Chapter 5. Automated Multi-atlas Labeling of the Fornix and its Integrity in Alzheimer's Disease

Chapter 6. Voxelwise Spectral Diffusional Connectivity

LIST OF TABLES

Chapters 2. Fiber Alignment and Spectral Clustering

Chapter 3. Multi-atlas Label Fusion Clustering

Chapter 4. Genetic Heritability

Chapter 5. Automated Multi-atlas Labeling of the Fornix and its Integrity in Alzheimer's Disease

Chapter 6. Voxelwise Spectral Diffusional Connectivity

ACKNOWLEDGEMENTS

Committee Members:

- Dr. Paul M. Thompson (Co-Chair)
- Dr. Daniel B. Ennis (Co-Chair)
- Dr. Yonggang Shi
- Dr. Arthur W. Toga
- Dr. Nader Pouratian
- Dr. Ricky K. Taira
- Dr. (Henry) Sung-Cheng Huang
- Dr. Luminita A. Vese

Colleagues:

- Dr. Junning Li
- Dr. Liang Zhan
- Dr. Neda Jahanshad
- Dr. Shantanu Joshi
- Dr. Boris A. Gutman
- Dr. Xue Hua
- Marina Barysheva
- Talia M. Nir
- Christina P. Boyle

Office:

- Grace Liang-Franco
- Melinda Ly
- Diana Kapadia
- Jonathan L. Pierce
- Joseph Franco
- Yama Nawabi
- Petros Petrosyan
- Tracey Wang
- Amanda He

Funding Agencies:

The twin study was supported by Grant R01 HD050735 from the National Institutes of Health and by Grant 496682 from the National Health and Medical Research Council, Australia. The Alzheimer's Disease Neuroimaging Initiative (ADNI) (NIH Grant U01 AG024904) is funded by the National Institute on Aging, National Institute of Biomedical Imaging and Bioengineering, and through generous contributions from the following: BioClinica, Biogen Idec, Bristol-Myers Squibb, Eisai Inc., Elan Corporation, GE Healthcare, Genentech, Innogenetics N.V., Janssen Pharmaceuticals, Johnson and Johnson, Eli Lilly and Company, IXICO PLC., Merck & Co., Meso Scale Diagnostics, NeuroRx Research, Novartis AG, Pfizer Inc., Piramal Group, Hoffmann-La Roche Inc., Laboratoires Servier, Synarc Imaging, Takeda Pharmaceuticals LLC., as well as nonprofit partners Canadian Institutes of Health Research, the Alzheimer's Association, and Alzheimer's Drug Discovery Foundation, with participation from the U.S. Food and Drug Administration. Private sector contributions to ADNI are facilitated by the Foundation for the National Institutes of Health. The grantee organization is the Northern California Institute for Research and Education, and the study is coordinated by the Alzheimer's Disease Cooperative Study at the University of California, San Diego. ADNI data are disseminated by the Laboratory for Neuro Imaging at the University of Southern California.

VITA

EDUCATION

09.2009-03.2014

Doctoral student, Biomedical Engineering, University of California, Los Angeles (UCLA)

RESEARCH EXPERIENCE

09.2009-03.2014

Graduate Student Researcher, Laboratory of Neuro Imaging, UCLA

PROFESSIONAL EXPERIENCE

03.2007-09.2009

Software Quality Assurance Engineer, TeraRecon, Inc., San Mateo, CA

AWARD

10.2010-09.2011

UCLA NeuroImaging Training Program Fellowship

SELECTED PUBLICATIONS

1. **Y. Jin**, Y. Shi, L. Zhan, B.A. Gutman, G.I. de Zubicaray, K.L. McMahon, N.G. Martin, M.J. Wright, A.W. Toga, and P.M. Thompson, "Automatic Clustering of White Matter Fibers in Brain Diffusion MRI with its Application to Genetics," *NeuroImage*, 2014.

2. J. Li*, **Y. Jin***, Y. Shi, I.D. Dinov, D.J. Wang, A.W. Toga, and P.M. Thompson, "Voxelwise Spectral Diffusional Connectivity and its Applications to Alzheimer's Disease and Intelligence Prediction," *Medical Image Computing and Computer Assisted Intervention* (*MICCAI*), Nagoya, Japan, LNCS 8149, pp. 655-662, 2013. (*: These two authors contributed equally to this work).

3. **Y. Jin**, Y. Shi, L. Zhan, G.I. de Zubicaray, K.L. McMahon, N.G. Martin, M.J. Wright, and P.M. Thompson, "Labeling White Matter Tracts in HARDI by Fusing Multiple Tract Atlases with Applications to Genetics," *IEEE International Symposium on Biomedical Imaging* (*ISBI*), pp. 508-511, San Francisco, USA, 2013.

4. **Y. Jin**, Y. Shi, L. Zhan, J. Li, G.I. de Zubicaray, K.L. McMahon, N.G. Martin, M.J. Wright, and P.M. Thompson, "Automated Population HARDI White Matter Tract Clustering by Label Fusion of Multiple Tract Atlases," *Multimodal Brain Image Analysis* (*MBIA*) on *MICCAI*, Nice, France, LNCS 7509, pp. 147-156, 2012.

5. **Y. Jin**, Y. Shi, S.H. Joshi, N. Jahanshad, L. Zhan, G.I. de Zubicaray, K.L. McMahon, N.G. Martin, M.J. Wright, A.W. Toga, and P.M. Thompson, "Heritability of White Matter Fiber Tract Shapes: A HARDI Study of 198 Twins," *MBIA* on *MICCAI*, Toronto, Canada, LNCS 7012, pp. 35-43, 2011.

6. **Y. Jin**, Y. Shi, N. Jahanshad, I. Aganj, G. Sapiro, A.W. Toga, and P. Thompson, "3D Elastic Registration Improves HARDI-derived Fiber Alignment and Automated Tract Clustering," *IEEE ISBI*, pp. 822-826, Chicago, USA, 2011.

ORAL PRESENTATIONS

1. **Y. Jin**, Y. Shi, L. Zhan, A.W. Toga, G.I. de Zubicaray, K.L. McMahon, N.G. Martin, M.J. Wright, and P.M. Thompson, "Three-dimensional Genetic Profiles of White Matter Fiber Tracts in HARDI with Automated Multi-atlases Fusion Labeling," *The Annual Meeting of Society for Neuroscience* (*SFN*), San Diego, CA, USA, 2013.

2. **Y. Jin**, Y. Shi, L. Zhan, J.A. Brown, S.Y. Bookheimer, A.W. Toga, G.I. de Zubicaray, K.L. McMahon, N.G. Martin, M.J. Wright, and P.M. Thompson, "Automatic HARDI White Matter Tract Labeling with Multiple Atlas Fusion," *The Annual Meeting of the Organization for Human Brain Mapping* (*OHBM*), Beijing, China, 2012.

ABSTRACT

1. **Y. Jin**, Y. Shi, L. Zhan, G.I. de Zubicaray, K.L. McMahon, N.G. Martin, M.J. Wright, and P.M. Thompson, "Automated Labeling of White Matter Tracts in HARDI: Tract Heritability in Twins," *The Annual Meeting of OHBM*, Seattle, WA, USA, 2013.

CHAPTER 1

Introduction

Diffusion-weighted magnetic resonance imaging (DT-MRI) (Basser *et al*., 1994) is a powerful non-invasive brain imaging technique introduced in (Le Bihan *et al*., 1986; Merboldt *et al*., 1985; Taylor *et al*., 1985). DT-MRI measures water diffusion in tissues, and provides biologically and clinically relevant information on white matter (WM) integrity and connectivity not available from other imaging modalities. It is increasingly used to study pathology and connectivity of WM pathways in the living brain (Thomason *et al*., 2011; Jahanshad *et al*., 2012*a*; Daianu *et al*., 2013).

Recently, DT-MRI has been extended to more sophisticated models of local diffusion, such as high angular resolution diffusion imaging (HARDI) (Tuch, 2004), diffusion spectrum imaging (Wedeen *et al*., 2005), or even hybrid imaging where large numbers of angular samples are collected at several diffusion weightings (Zhan *et al*., 2011). With these imaging protocols, we can more accurately reconstruct fibers that mix and cross.

Tractography is a method to reconstruct the pathways of major WM fiber bundles, by fitting a curved path through the directional diffusion data at each voxel. Deterministic tractography (Mori *et al*., 1999; Conturo *et al*., 1999; Basser *et al*., 2000) recovers fibers emanating from a seed voxel by following the principal direction of the diffusion tensor or the dominant direction of the diffusion orientation distribution function (ODF). However, deterministic tractography has

limitations: it depends on the choice of initial seed points and can be sensitive to the estimated principal directions. To overcome those drawbacks, probabilistic tractography methods have been proposed (Behrens *et al*., 2003; Parker *et al*., 2003*a*; Aganj *et al*., 2011). They can be computationally more intensive but can be more robust to partial volume averaging effects and uncertainties in the underlying fiber direction, which are inevitable due to imaging noise.

Several approaches have been developed to study brain connectivity using whole-brain tractography. Jahanshad *et al*. (2011) computed a whole-brain connectivity matrix based on streamline tractography and anatomical parcellation. Network-based analysis of this matrix can identify factors that affect the interconnectedness of regions in the brain. For example, Ingalhalikar *et al.* (2013) revealed connectivity pattern differences between males and females. Prasad *et al*. (2011) applied a probabilistic WM atlas to extract major fiber bundles and represented them using a "maximum density" path. A mean curve was used to represent each bundle in each subject. Fractional anisotropy (FA) values, and other indices of diffusion, can be compared along this path across a population, using 'along-tract' statistics (Corouge *et al*., 2006; Colby *et al*., 2011).

Obviously it is important to accurately identify WM structures and fibers from whole-brain tractography. If fibers are grouped into bundles, the results can offer valuable insight on how disease affects the integrity of particular WM tracts (Price *et al*., 2007, 2008). *Clustering* methods can group fibers obtained from tractography into organized bundles or tracts, enabling large population studies of disease and genetic effects on tract integrity, or even tract shapes.

One simple yet practical strategy selects anatomically well-known WM tracts that interconnect anatomical regions of interest (ROIs) (Wakana *et al*., 2007; Zhang *et al*., 2010). 3-D models of tracts can facilitate large-scale population studies (Yushkevich *et al*., 2008; Brouwer *et al*., 2010). Even so, the final results often need substantial manual intervention to help screen out false positive fibers.

Automatic fiber clustering would accelerate and empower population studies, so long as the results are accurate and reliable. A typical framework for fiber clustering defines a pairwise similarity/distance between each pair of fibers in a large set of candidate fibers, to group them into separate and distinct tracts. Many different fiber similarity metrics have been proposed, such as the mean vector and the covariance matrix of fiber points (Brun *et al*., 2004), the number of points shared within the same voxel (Jonassan *et al*., 2004), an associativity vector (Wang *et al*., 2012), the average mean distance (Gerig *et al*., 2004; Xia *et al*., 2005; O'Donnell *et al*., 2006), Hausdorff distance (Gerig *et al*., 2004; Xia *et al*., 2005), and Mahalanobis distance (Maddah *et al*., 2008), etc. Also, various clustering algorithms have been advocated, such as hierarchical clustering (Gerig *et al*., 2004; Xia *et al*., 2005; Visser *et al*., 2010), expectation-maximization (Wang *et al*., 2012), fuzzy *c*-means (Li *et al*., 2010), *k*-nearest neighbors (Ding *et al*., 2003), normalized cuts (Brun *et al*., 2004), dual rooted graphs (Tsai *et al*., 2007), and spectral clustering (O'Donnell and Westin, 2007; Wassermann *et al*., 2008).

If clustering algorithms have no anatomical information to guide them, tracts may not correspond to any anatomically familiar subdivisions. There is also no guarantee that the same

basic sets of bundles will be generated again in datasets from new subjects, making it hard to compare results from one study to the next. Also, a user typically needs to specify the number of clusters or a threshold to decide when to stop merging or splitting clusters. Clustering results can vary drastically when different numbers of clusters are specified. "Bottom-up" methods cluster fibers into larger groups until major tracts are aggregated, but they may not efficiently filter out erroneous fibers buried in the large number of streamlines (100,000-1,000,000) generated by whole-brain tractography.

Recent hybrid approaches extract the well-known WM tracts using a combination of prior information from an anatomically-labeled atlas and similarity-based clustering. Wassermann *et al*. (2010) proposed a Gaussian process framework to generate a fiber 'dendrogram' and selected which ones to merge through a query system based on parcellated volumetric information. Li *et al*. (2010) clustered tracts via anatomical ROI guidance, and then passed them through similarity-based fuzzy *c*-means clustering. Guevara *et al*. (2012) implemented a two-level (intra-subject and inter-subject) centroid-based average-link hierarchical clustering. The resulting clusters were manually labeled to form a multi-subject WM atlas. A new tractography data set was similarly segmented and the clusters were labeled using a supervised classification based on the atlas.

The large number of false positive fibers produced by streamline-based tractography hinders large population studies. An atlas-based top-down clustering method resolves this, by requiring that all subjects' WM tracts fall within a pre-defined set of shapes or regions. Even so, an atlas

based on one individual subject's anatomy is not sufficient to capture the variability of individual WM tracts. One classical solution is called multi-atlas labeling or *label fusion*. This has commonly been applied to label brain structures on standard anatomical MRI (Rohlfing *et al.*, 2004; Hackemann *et al.*, 2006; Lotjonen *et al.*, 2010; Sabuncu *et al.*, 2010; Chou et al., 2007, 2008, 2009).

In traditional image segmentation, a deformable atlas may be used, in which an atlas is non-rigidly registered to the image to be labeled. The resulting deformation may then be used to map the training labels onto the new image. Multiple atlases and registrations may also be used to transfer multiple training labels to the new subject's space. The final labeling can be obtained by applying a weighting approach to the labels transferred from different atlases. Label fusion has two advantages: 1) it is easier to accommodate large individual variations in anatomy if one does not have to rely on a single atlas; 2) multiple registrations improve robustness against occasional registration failures and non-global minima of the registration cost function. The same idea can also improve voxel-based or tensor-based morphometry (Leporé *et al*., 2008*b*).

CHAPTER 2

Fiber Alignment and Spectral Clustering

Before I introduce the multi-atlas label fusion clustering technique, I would like to present my preliminary work about how 3-D elastic registration improves fiber alignment and automated spectral clustering.

2.1 Introduction

A typical framework for spectral clustering is first to define a similarity metric (commonly based on distance) and a similarity matrix between all pairs of fibers. The eigenvectors of this similarity matrix are calculated. Finally, a clustering algorithm - for example, k-means - classifies the fibers in the spectral space spanned by the first k eigenvectors (k is the cluster number, usually defined manually). Some classic clustering work has been presented by O'Donnell and Westin (2007) and Wassermann *et al*. (2008).

It is highly desirable to cluster fiber tracts into groups consistently in a large population study. An open question, which we address here, is whether this clustering is more successful when fibers have already been pre-aligned across subjects, via deformable image registration. For all of the clustering methods mentioned above, diffusion-weighted images are usually only linearly registered across subjects (O'Donnell and Westin, 2007; Ziyan *et al*., 2012). Surprisingly, non-rigid registration is rarely used before clustering. Here we use a variety of distance and overlap

metrics to test whether non-rigid (3-D elastic) registration of diffusion data can improve the alignment of embedded tracts. We also assess, in turn, whether the improved fiber alignment may facilitate clustering. The overall goal of this work is to improve the power of multi-subject analysis of diffusion imaging data, and improve the automation of large-scale tract-based studies.

2.2 Methods

2.2.1 Subjects and Image Acquisition

High angular resolution diffusion imaging (HARDI) images were acquired as part of a larger study of 374 young adults with a 4 Tesla Bruker Medspec MRI scanner. T1-weighted images were acquired with an inversion recovery gradient echo sequence with parameters: T1/TR/TE=700/1500/3.35 ms, flip angle=8°, slice thickness=0.9mm, and a 256x256x256 acquisition matrix. HARDI images were acquired by single-shot echo planar imaging with parameters: TR/TE=6090/91.7ms, 23cm FOV, and a 128x128x55 acquisition matrix. Axial slice thickness =1.79mmx1.79mmx2mm. 105 volumes of images were acquired for each subject: 11 with no diffusion sensitization, that is, T2-weighted *b0* volumes and 94 diffusion-weighted volumes (b = 1159 s/mm^2). As they were recruited for a large genetic study, the subjects were 120 young adult monozygotic twins, 90 same-sex dizygotic twins, and 164 mixed-sex dizygotic twins. The genetic aspects were not pursued in this paper, so the subjects were just treated as individuals. All subjects were right-handed and had no history of head injury or mental illness.

2.2.2 Registration

Image registration was conducted in four steps (Jahanshad *et al*., 2010):

Step I: Each subject's anatomical T1-weighted image and set of HARDI images were linearly aligned to the Colin27 high-resolution single-subject template (Holmes *et al*., 1998).

Step II: After eddy current correction with FSL software (http://fsl.fmrib.ox.ac.uk/fsl/), the voxel-wise average of each subject's 11 *b0* images was elastically registered to the same subject's aligned T1-weighted images using inverse-consistent elastic registration (Leow *et al*., 2007). This step used mutual information as a cost function for an elastic deformation model implemented using the spectral method (Fast Fourier Transform). To correct for EPI-related distortions, the resulting 3-D deformation fields (which had a 32x32x32 resolution in the frequency domain) for each subject were applied to the rest of the 94 HARDI volumes. Following EPI distortion correction, fractional anisotropy (FA) was computed from the 105-gradient HARDI images using FSL. The rest of the registration steps used distortion-corrected FA images.

Step III: We created a geometrically-centered, minimal deformation target (MDT) from a randomly selected set of 32 subjects' FA maps using a nonlinear viscous fluid registration (Leporé *et al*., 2008*a*), which allows large deformations without causing singularities in the deformation field (i.e., regions of non-positive Jacobian determinant). All the FA images of each subject were then registered to the MDT by elastic registration (Leow *et al*., 2007). The resulting

finer-scale 64x64x64 resolution deformation fields were used to align all subjects' FA images into the same coordinate space.

Step IV: Finally, to better align white matter regions of interest, the MDT and each subject's FA images were thresholded to include only the regions where FA>0.25. Individual thresholded FA images were once again registered to the thresholded MDT, using a third set of 3-D 64x64x64 resolution deformation fields. We found in our prior work (Jahanshad *et al*., 2010) that this iterative registration process leads to good alignment of FA maps for statistical studies.

2.2.3 Tractography

We then performed whole-brain tractography with a global probabilistic approach that uses the Hough transform as a voting procedure (Aganj *et al*., 2011). We first generated a large number of initial seed points inside the brain. From each initial point, as many passing curves as possible were considered (this could depend on the data resolution and available computational resources). A score was assigned to each curve based on the normalized and dimensionless orientation distribution function (ODF) estimator in *q*-ball imaging (Aganj *et al*., 2010), and also considering the FA along the path. Curves with the highest scores were picked as the fibers that passed through each seed point. We extracted fibers for each subject from the linearly aligned HARDI images (after step I in **Section 2.2.2**) and saved the coordinate points of each fiber in a text document, as a look-up table for later nonlinear alignments.

2.2.4 Spectral Clustering

We used the spectral clustering method described in (von Luxburg, 2007). A similarity matrix (the fiber similarity) was constructed based on the distances between fibers. We used the metric in (O'Donnell and Westin, 2007) to calculate the distance between fibers i and j. First, we found the closest point on fiber j for each point on fiber i and stored the distance. The distance was averaged after computing distances from all the points on fiber i. We denote it as d_{ij}. Spectral clustering requires a symmetric matrix. Therefore, we took the average of the directed distances d_{ij} and d_{ji}.As a result, the distance between two fibers became undirected. Then, a Gaussian kernel was applied to convert the distance to a similarity measure $A_{ij} = exp(-d_{ij}^2/\sigma^2)$. σ determines the range of distances over which fibers may be considered similar. We chose $\sigma = 5$ voxels, for this study.

An astronomical number of fibers are available when performing multi-subject clustering. To shorten the computation time, we defined a neighborhood (e.g., 5 voxels) around the coordinate points along a fiber. We only calculated the distances between the fibers that crossed this neighborhood of the specified fiber. Other fibers were classified as having no connection with this particular fiber. Next, a normalized graph Laplacian matrix was created, defined as $L = I - D^{-1/2}AD^{1/2}$, where I is the identity matrix and D is a diagonal matrix, whose diagonal elements are the sum of each row of A_{ij}. By manually setting the cluster number k, the first k generalized eigenvectors of $Lu = \lambda Du$ were computed.

Finally, the k-means algorithm was used to cluster the points (which represent individual fibers) in the space spanned by the k eigenvectors. **Figure 2-1** shows an example clustering result when $k = 10$ by running the algorithm as described above.

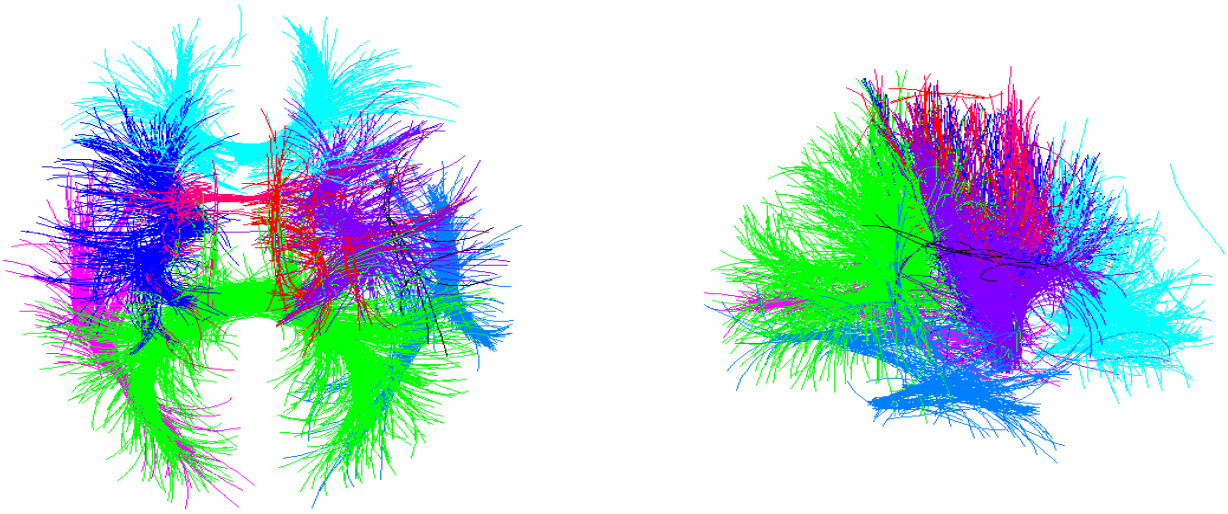

Figure 2-1. A representative result of spectral clustering in 4-Tesla 105-gradient HARDI data from one individual subject (with $k = 10$ clusters). Each cluster is labeled with a separate color. *Top* and *side* views of the brain are shown. Several major tracts are evident, including the *forceps major,* which runs through the splenium of the back of the corpus callosum (*green*), and the fibers running in the callosal *genu* (*light blue*).

2.2.5 Non-rigid Fiber Warping

Before performing multi-subject clustering, we also warped the fibers from all subjects by applying the deformation fields generated in **Section 2.2.2**. We applied all deformation mappings in sequence through tri-linear interpolation. An illustration is shown in **Figure 2-2**.

2.2.6 Evaluation

Two metrics were selected to evaluate the performance of non-rigid image registration on fiber alignment. We used the mean distance between the "corresponding" fibers of the two subjects and the percentage of the fibers that had a "better match" after warping. The "corresponding" fibers refer to the two individual fibers in each of two different subjects with the shortest distance between each other. The fiber distance is defined as the mean of the distances from the coordinate points over one curve to the nearest points on the other curve. It is symmetrized by taking the average of two directed distances between the two curves. This is detailed in **Section 2.2.4**. These corresponding fibers do not necessarily form part of an overall one-to-one mapping of all the fibers between the two subjects. We calculated the mean distance of all the corresponding fibers within these two subjects and used it as an index of registration quality. A "better match" means that a closer corresponding fiber from the other subject is found for a particular fiber in one subject.

To evaluate how fiber warping affected the population clustering, we calculated overlap percentages for the fibers within the same clustered bundle (e.g., the *forceps major* which runs through the posterior region of the corpus callosum) using different neighborhood sizes for the group clustering. The overlap percentage is defined as 100 times the following fraction

$$\frac{\text{fibers clustered to a specific bundle with nbhd } i \cap \text{with nbhd } j}{\text{fibers clustered to a specific bundle with nbhd } i \cup \text{with nbhd } j}$$

where nbhd i and j are the neighborhoods (e.g., 5-voxel neighborhoods) used to compute the similarity matrix in **Section 2.2.4**. Presumably, different neighborhood sizes will produce

different clustering results. The overlap percentages before and after warping were compared (see **Section 2.3.2**) to assess how stable the population clustering results were after fiber warping.

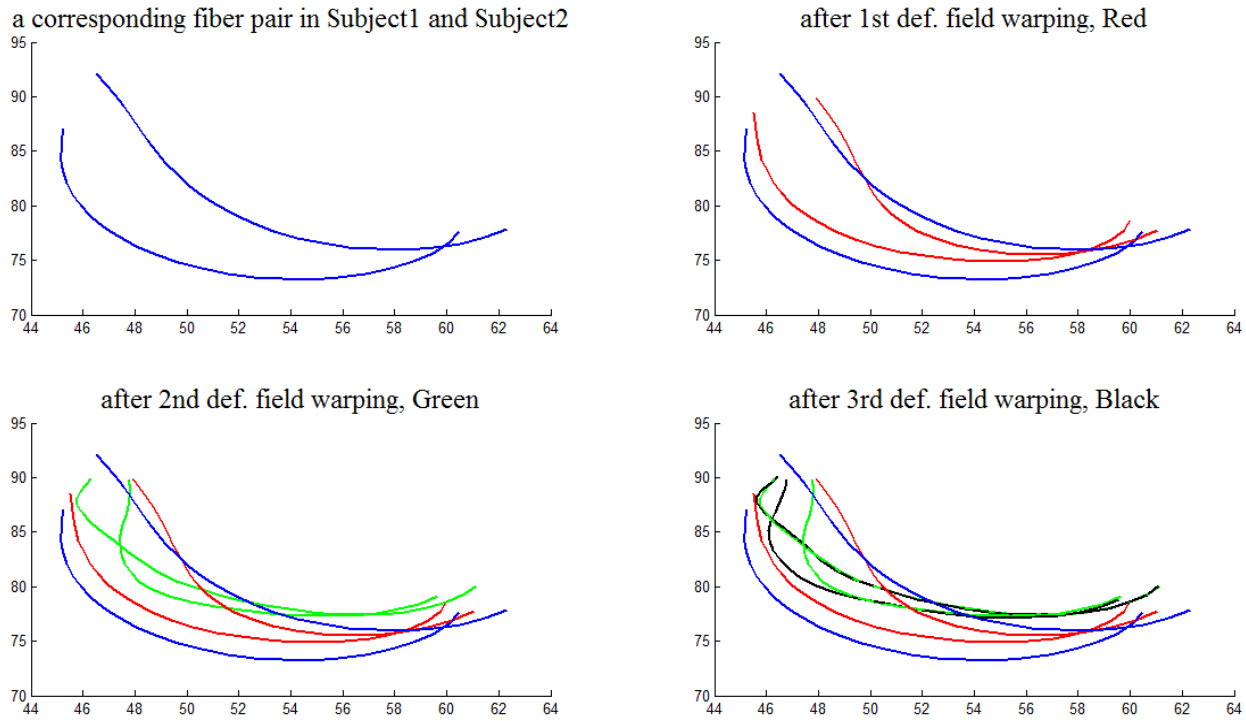

Figure 2-2. Two "corresponding" fibers are shown (*blue colors, top left;* "corresponding" is defined in **Section 2.2.6**). These are then warped, step by step, through the three deformation fields generated in the registration step.

2.3 Results

To make computations easier, two groups, with a total of 20 subjects were selected from the HARDI database of 374 subjects to perform a sample population clustering analysis. Ten subjects were randomly selected and the other ten were those whose deformation fields in the registration step had the greatest magnitude on average across the brain. There were no twin

pairs within either group to avoid any genetic influence (artificial resemblance) in the warping results.

2.3.1 Fiber alignment

In **Table 2-1**, quantitatively, we show that fiber alignment is indeed improved after using the information from 3-D elastic image registration. For each subject, we first calculated the average distances between "corresponding" fibers (defined in **Section 2.2.6**) with every other subject in the population of each group, and then took the mean of these average distances within a group as group mean distance (G.M.D.). We calculated it both before and after warping. We also counted the percentages of "better matched" (also defined in **Section 2.2.6**) fibers after warping between that subject and every other subject. Next, a group mean of these percentages was taken as the mean better matched fiber (B.M.F.) percentage for that group. As a result, the G.M.D. between corresponding fibers from one subject to the others was shortened from 2.44 voxels to 2.05 voxels, giving a *p*-value of 2.14×10^{-8} in a paired *t*-test. These statistics were derived for the randomly selected group – a significant 16% improvement. We also analyzed results for the subjects with the greatest anatomical deviation from the mean template, as computed from the deformation maps. For this "most highly deviating" group the G.M.D. dropped from 2.89 voxels to 2.27 voxels with a *p*-value 2.27×10^{-7}, according to a paired *t*-test. Interestingly, a *p*-value 9.95×10^{-4} in a separate *t*-test between the improvements in the two groups indicated that elastic fiber warping was more helpful for the set of subjects whose images deviated more. This is in line with common sense: the method is genuinely better aligning tracts in those with greater initial deviations. On average, the majority of fibers were better aligned (i.e., found a B.M.F. in

another subject) after non-rigid warping in both the randomly selected subgroup (by 70%) and the "most highly deviating" group (by 73%).

To visualize these effects, **Figure 2-3** shows the same fibers for all ten subjects in the most anatomically deviating group in a particular cluster before and after elastic warping. Clearly, the overall path of the fiber set is "tidier", after warping, and more obviously clustered.

Table 2-1. Mean fiber matching distances and the percentages of better matched fibers (after versus before warping) from one particular subject to the rest of the sample population.

Group	G.M.D.[1] between corresponding fibers (voxel)			Improv-ed Pct. of G.M.D.	Group Mean B.M.F.[2] Pct.
	Pre-warp	Post-warp	*p*-value of *t*-test		
Randomly Selected Subjects	2.44	2.05	2.14×10^{-8}	16%	70%
Most Highly Deviating Subjects	2.89	2.27	2.27×10^{-7}	21%	73%

[1] G.M.D. = Group Mean Distance

[2] B.M.F. = Better Matched Fibers

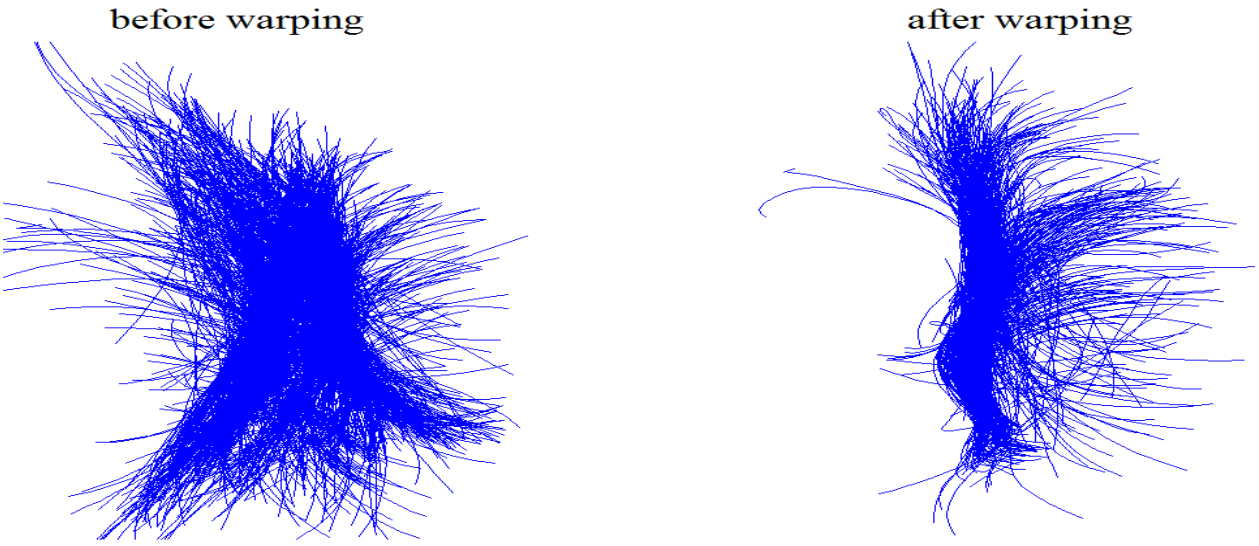

Figure 2-3. The same fibers of all 10 subjects in the most anatomically deviating group in one cluster are shown, before (*left*) and after (*right*) 3-D elastic warping.

2.3.2. Clustering Robustness

The overlap percentages (defined in **Section 2.2.6**) for the fibers belonging to the *forceps major* - which travels through the posterior region of the corpus callosum - were calculated for different neighborhood sizes. The neighborhood size is a free parameter needed to compute the similarity matrix for clustering. Taking the 2.5-voxel neighborhood as a reference, we compared it to other neighborhood sizes, by assessing the overlap percentages for each subject from the population clustering results. The mean across the group and the *p*-values of the paired *t*-tests assessing improvements due to warping are shown in **Table 2-2**. For both groups, we saw significant improvements based on the *p*-values. Therefore, fiber warping does generate more robust results, even when different parameters are used in the clustering algorithm.

Figure 2-4 shows the *forceps major* bundle in the posterior region of corpus callosum in a representative subject, before and after elastic fiber warping.

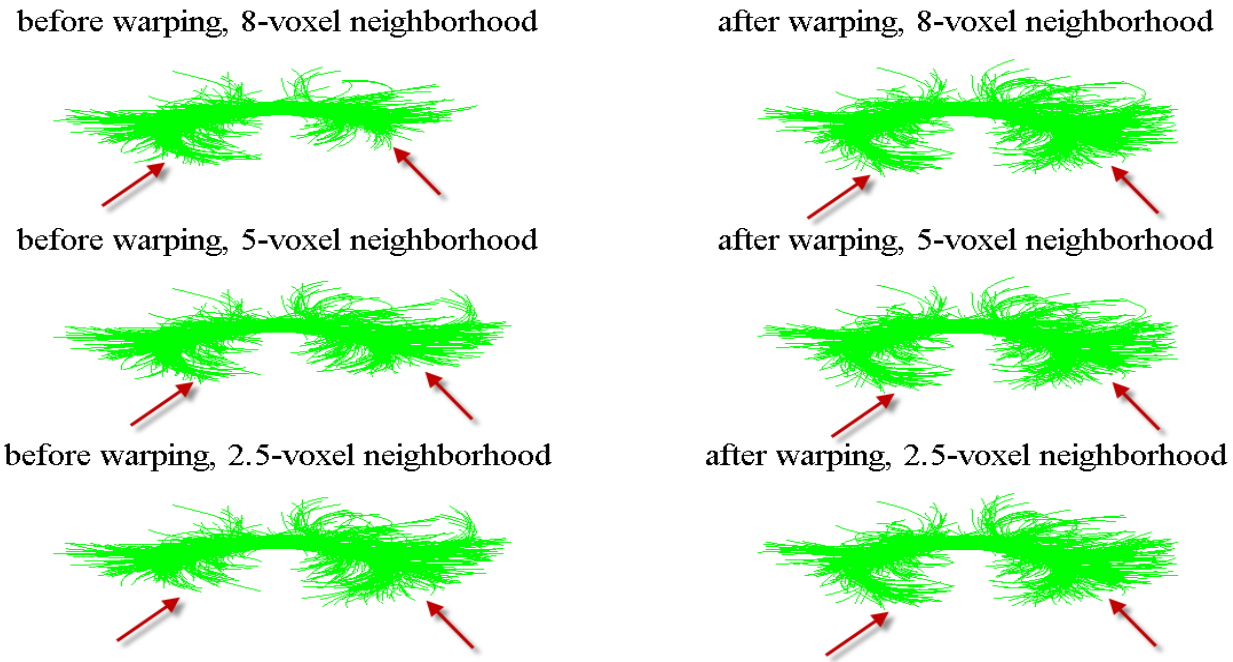

Figure 2-4. *Top* views of fibers clustered as the *forceps major* at the back of corpus callosum, using different neighborhood sizes in the spectral clustering method. Arrows point to the regions with different levels of consistency in clustering results with and without fiber warping.

Table 2-2. The mean overlap percentages of fibers in the *forceps major* in the posterior region of the corpus callosum, when different neighborhoods were used to compute the similarity matrix used for clustering (the 2.5-voxel neighborhood was considered as the reference).

Group	Mean Overlap Percentage			
	5 vs. 2.5-voxel neighborhood		8 vs. 2.5-voxel neighborhood	
	Pre-warp	Post-warp	Pre-warp	Post-warp
Randomly Selected Subjects	58%	68%	51%	62%
p-value of *t*-test	1.18×10^{-6}		9.59×10^{-9}	
Most Highly Deviating Subjects	93%	96%	69%	95%
p-value of *t*-test	0.026		2.67×10^{-6}	

2.4 Discussion

In this preliminary work, we showed that the information obtained from nonlinear registration of HARDI may be used to improve fiber alignment for clustering in multi-subject studies. Improved fiber alignment can lead to more robust clustering, even under reasonable variations in the algorithm parameters.

The spatial resolution of the deformation fields in this work was lower than the image resolution, which made interpolation necessary to calculate the fiber positions after warping. In future, we will assess whether fiber alignment would be further improved by running the elastic registration on a finer computational grid. This would avoid interpolation, and may align features more precisely. The spatial regularity of the applied deformation field is also relevant, and

higher-dimensional registrations are not necessarily better. With higher frequency warping, a fiber may become increasingly twisted. This may eventually adversely affect the curvature and smoothness of the original fiber. In the future, we will investigate whether higher-dimensional deformations, with higher spatial frequencies, would further improve fiber alignment, or whether there is an optimal intermediate trade-off.

In this work, we only took advantage of information obtained by registering scalars derived from the diffusion tensor images, which typically have lower resolution than T1-weighted images. Naturally, registration based on a combination of both HARDI and T1-weighted images may further improve fiber alignment (Studholme *et al*., 2007). Nevertheless, based on our work, non-rigid fiber warping seems to be a beneficial step before performing clustering in population studies.

CHAPTER 3

Multi-atlas Label Fusion Clustering

3.1 Overview

Here we extend label fusion to fiber clustering and introduce a multi-atlas framework to automatically extract anatomically meaningful white matter (WM) tracts. First, whole-brain tractography was generated, as a basis to perform clustering (**Section 3.2**). Then, we manually constructed a number of WM fiber tract atlases, consisting of several major WM tracts. The regions of interest (ROIs) of a single-subject standard template were warped to our manual atlases through registration and the tracts were extracted using a look-up table and manually edited (**Section 3.3**). In contrast to prior "bottom-up" methods, we used the WM tracts in multiple hand-labeled atlases as prior anatomical information. To cluster tracts in a new subject, the corresponding tracts from our manual atlases were warped to that subject's space and a multi-level fiber clustering scheme was applied to label the tracts (**Section 3.4**). Our "top-down" approach transfers tract labels by selecting only fibers similar to the corresponding tracts in the atlases, based on a similarity measure. This eliminates many false positive fibers hidden in the ~1,000,000 fibers per subject produced by streamline tractography. Multiple atlases adapt to the variability of tract shapes in new subjects. This reduces the number of outliers and picks fibers that can be incorrectly omitted when registering a single atlas to the whole-brain tractography in a new subject. Finally, we used label fusion to combine the clustered results from individual atlases (**Section 3.5**). These steps are summarized in **Figure 3-1**.

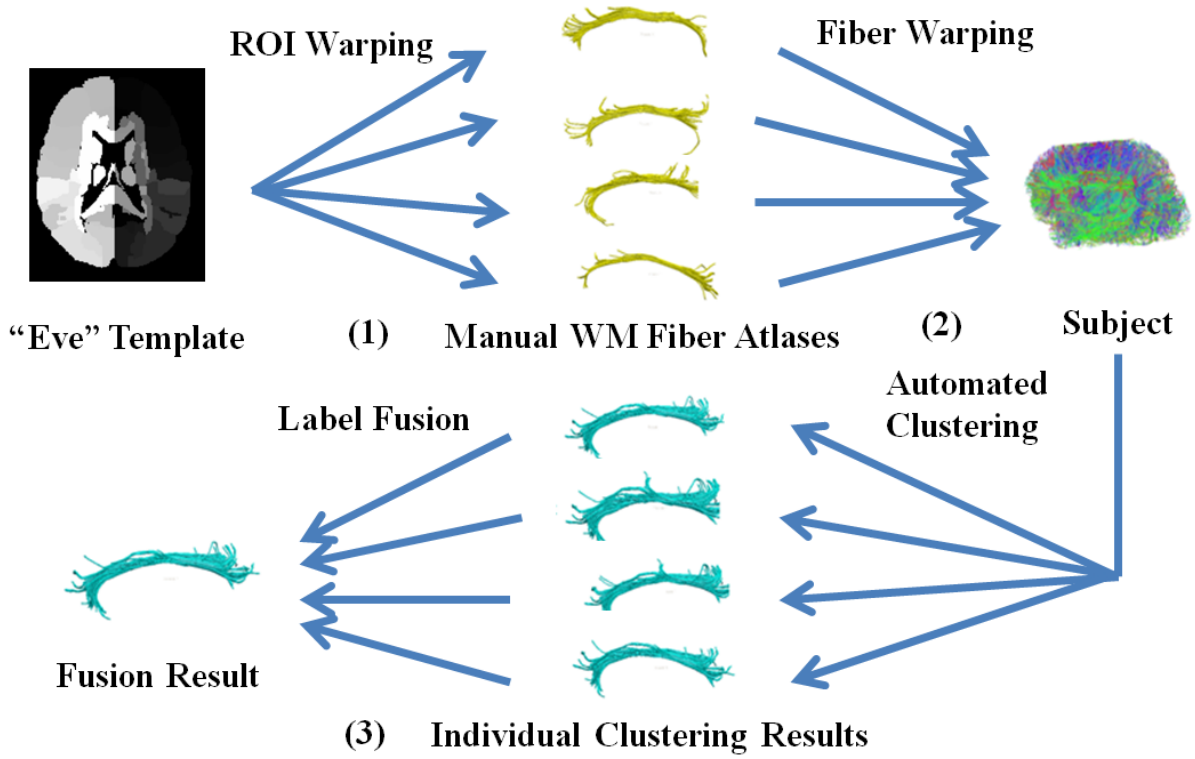

Figure 3-1. Flow chart of steps in our fiber clustering framework. (1) Manual WM atlases were constructed through warped ROI extraction from a standard template; (2) A multi-level fiber clustering scheme was used to label tracts in new subjects; (3) Final results were created by fusing individual results from step (2).

3.2 Tractography

We performed whole-brain tractography with Camino (http://cmic.cs.ucl.ac.uk/camino/), an open source software package that uses either streamline or probabilistic methods to reconstruct fiber paths. It uses a spherical harmonic (SH) representation to represent the diffusion orientation distribution functions (ODF); this can be more robust to noise and may even be more accurate for detecting fiber crossings than the original numerical *q*-ball reconstruction method (Descoteaux *et al*., 2007). Explicitly, the SH basis may be expressed as follows:

$$Y_l^m(\theta,\varphi) = \sqrt{\frac{(2l+1)(l-m)!}{4\pi(l+m)!}} P_l^m(cos\theta) e^{im\varphi} \quad (3.1)$$

where l denotes the order, m denotes the phase factor, $\theta \in [0,\pi]$, $\varphi \in [0,2\pi]$, and P_l^m is an associated Legendre polynomial. Signal at each gradient direction may be approximated as a linear combination of a modified version of this SH basis. We used the 6th order (l=6) SH series to reconstruct ODF for our high angular resolution diffusion imaging (HARDI) data and a maximum of 3 local ODF maxima (where fibers mix or cross) were set to be detected at each voxel.

Next, we performed fiber tracking with a probabilistic algorithm, called the 'Probabilistic Index of Connectivity' (PICo) (Parker *et al*., 2003*b*), in Camino. At first, we created a simulated data set for diffusion probability density function (PDF) calibration, based on the signal-to-noise ratio of our dataset. Then, based on different diffusion distribution uncertainty models (Bingham or Watson), simulated data was reconstructed to generate a look-up table, which was in turn used to produce the PDF estimates of the actual data from the derived local ODF maxima. Seed points were chosen at those voxels whose fractional anisotropy (FA) values were greater than 0.4. Monte Carlo simulation was used to generate fibers proceeding from the seed points throughout the entire brain. Streamline fiber tracing followed the voxel-wise PDF profile with the Euler interpolation method for 10 iterations per each seed point. The maximum fiber turning angle was set to 40°/voxel, and tracing stopped at any voxel whose FA was less than 0.2.

3.3 White Matter Tract Atlas Construction

We randomly selected five subjects (none were members of the same twin pair, three males and two females) from our HARDI data set (see **Chapter 4** for details) and constructed WM tract atlases. In this context, atlas means a hand labeled representation of the fibers in a subject. The FA images of all the atlases were registered to a single-subject template called the "Type II Eve Atlas" (a 32-year old healthy female) (Oishi *et al*., 2009). The entire brain of the "Eve" template was parcellated using 130 bilateral ROIs (Zhang *et al*., 2010).

The labeled template ROIs were re-assigned to the five registered atlases, respectively, by warping them with the deformation fields generated by Advanced Neuroimaging Tools (ANTs) (Avants *et al*., 2008, http://picsl.upenn.edu/software/ants/). Fibers that traversed the ROIs were extracted according to the look-up table in Zhang *et al*. (2010). For example, the corticospinal tract was extracted from fibers passing between the precentral gyrus and the cerebral peduncle. Finally, each tract was manually edited to remove visible outliers. We rounded the floating point coordinate locations along a fiber to the location of the closest voxel. For a given tract, there is a certain set of ROIs that it is expected to intersect – this may be two or more. If any of the fiber's discrete lattice points fell into the ROI, we would consider that this fiber traversed the ROI; otherwise, it didn't. A fiber must traverse all the required ROIs for a given tract to be considered as a candidate member of that tract, or it will be discarded. There was no ambiguity in deciding whether a fiber belonged to a tract or not, because it was counted as traversing the set of expected ROIs or not.

Currently, each atlas is comprised of 17 major WM tracts: left (L) / right (R) corticospinal tract (CST), L/R anterior thalamic radiation (ATR), L/R cingulum (CGC), L/R inferior fronto-occipital fasciculus (IFO), L/R inferior longitudinal fasciculus (ILF), L arcuate fasciculus (part of the superior longitudinal fasciculus) (ARC), and six segments of the corpus callosum – projecting to both frontal lobes (CC-FRN), precentral gyri (CC-PRC), postcentral gyri (CC-POC), superior parietal lobes (CC-PAR), temporal lobes (CC-TEM), and occipital lobes (CC-OCC) (Hofer *et al*., 2006). We did not include the right arcuate fasciculus as not all subjects had this tract in its entirety (Catani *et al*., 2007), and that would have made statistical analysis difficult. **Figure 3-2** shows all 17 WM tracts that we created and views of overlaid tracts from different angles (*back, left side, and bottom* views).

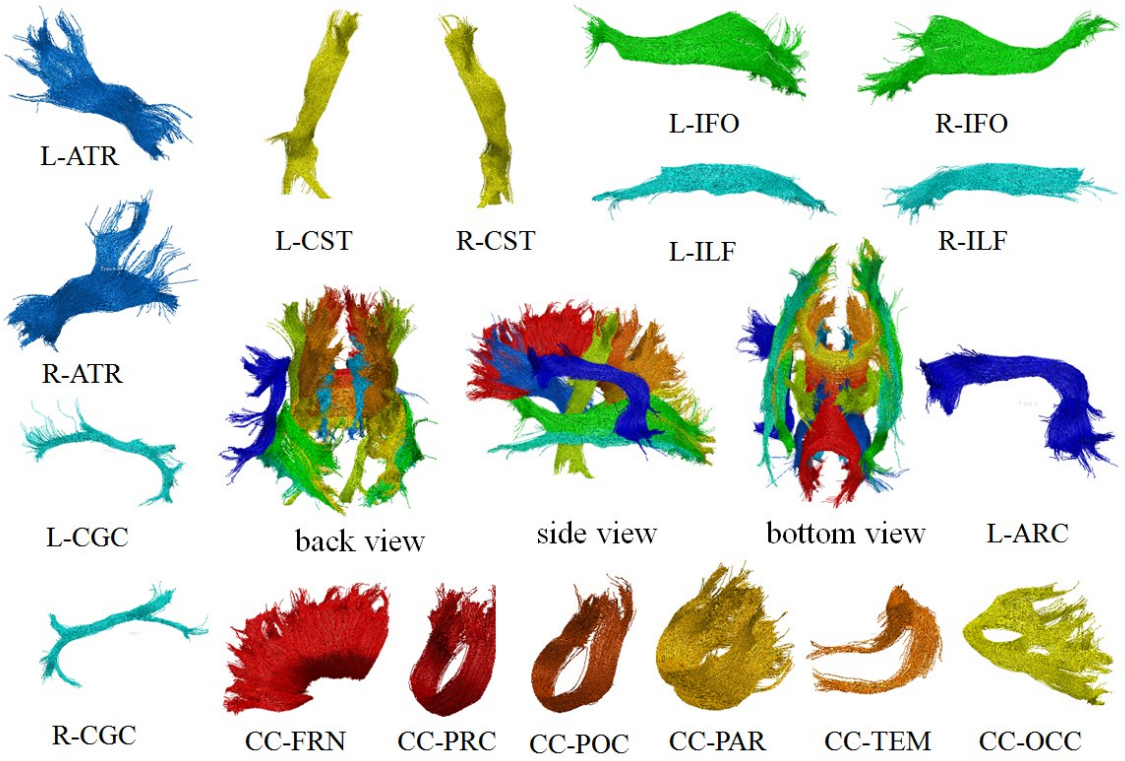

Figure 3-2. A representative WM fiber atlas computed, and manually edited, from 4-Tesla 105-gradient HARDI data, showing the 17 major tracts. We created these, with manual editing, in 5 subjects and propagated the tracts into new subjects. The tracts on the left side and the corpus callosum segments are viewed from the left, while the tracts on the right are viewed from the right. *Back, left side,* and *bottom* views of tract overlays are shown in the middle of the figure.

3.4 Multi-level Fiber Clustering

For each test subject (i.e., each new data set to be labeled), whole-brain tractography was extracted using Camino as well. We designed a multi-stage fiber clustering scheme to pick out appropriate candidate fibers for each tract.

3.4.1 Length-based Clustering

Image noise and limits in image resolution cause whole-brain tractography to generate many implausible short-length streamlines. All of our target fiber bundles are major tracts, so it was reasonable to assume that no component fiber is shorter than 35 mm. Streamlines shorter than this were removed. Of course this leads to some arbitrary limit in the types of tracts surveyed, and we have to concede that some true short fibers may be suppressed as well as many false ones.

3.4.2 ROI-based Clustering

The labeled "Eve" template ROIs were re-assigned to the subjects in our data set with the ANTs registration. Fibers that did not traverse the ROIs for a particular tract were removed. This reduced the number of detected fibers from around a million to a few hundreds or thousands of fibers of interest.

A few previous studies showed reliable and reproducible clustering results with either manual ROI placement (Wakana *et al*., 2007) or automated placement (Zhang *et al*., 2010). In our workflow, this step was also helpful to ease the computation when further refining the results in the next step (**Section 3.4.3**). With the automated ROI placement, we could effectively reduce the number of fibers of interest for a particular tract. Since it was a standard procedure consistently applied to all the subjects in our dataset, it established a basis to compare subjects for population studies.

3.4.3 Distance-based Clustering

After applying ROI constraints and the filters above, most of the short and obviously erroneous fibers were removed. To eliminate the remaining false fibers (see **Figure 3-3**) we implemented a geometry-based clustering algorithm to select only those streamlines whose shapes and locations were similar to those of manually constructed WM atlases in **Section 3.3**.

First, we registered the test subject's FA image to the FA image of each tract atlas using ANTs. Each atlas's tracts were then warped to the subject space with the corresponding deformation fields generated from the FA registration.

We defined a fiber distance metric to decide the subject's fibers that should be included in any individual warped atlas tract. For any pair of fibers γ_i and γ_j, we defined the symmetric Hausdorff distance (Gerig *et al*., 2004):

$$d_H\left(\gamma_i, \gamma_j\right) = \max(\mathrm{d}_{H'}(\gamma_i, \gamma_j), \mathrm{d}_{H'}(\gamma_j, \gamma_i)) \tag{3.2}$$

where $\mathrm{d}_{H'}$ is the asymmetric Hausdorff distance.

$$\mathrm{D}_{H'}\left(\gamma_i, \gamma_j\right) = \max_{x\in\gamma_i}\min_{y\in\gamma_j}||x - y|| \tag{3.3}$$

$||.||$ is the Euclidean norm and the ordered pair $\left(\gamma_i, \gamma_j\right)$ indicates an asymmetric distance from γ_i to γ_j. x's and y's are the coordinate points along fibers γ_i and γ_j, respectively.

Initial fuzzy fiber labeling based on each individual atlas was performed simply by aggregating fibers passing within a neighborhood of each atlas fiber, and setting the appropriate label. **Figure 3-3** illustrates how the right corticospinal tract is parsed out from the original whole-brain tractography following the multi-level fiber clustering steps.

3.5 Fiber Label Fusion

We chose the Hausdorff distance metric for the fiber clustering phase to select only streamlines with similar geometric shapes, and lying in the same region as the atlas tracts. However, due to the WM variability of individual atlases, different atlases may 'nominate' different candidates. We extended the well-established label fusion concept from traditional structural image segmentation to the WM fiber space. We defined a mean fiber distance to rank the fibers nominated by individual atlases. For each fiber, the mean fiber distance was defined as:

$$d_{mean} = \frac{\sum_{d_i<d_{cutoff}} d_i + \sum_{d_i>d_{cutoff}} d_{sup}}{n} \tag{3.4}$$

where d_i is the Hausdorff distance between an unlabeled subject's fiber and the i-th atlas, d_{cutoff} is the empirical cutoff threshold chosen in **Section 3.4.3**, d_{sup} is the upper bound Hausdorff distance within which a subject fiber can be possibly considered a candidate for a given tract, and n is the number of atlases. We ranked all the candidate fibers from different atlases based on their d_{mean}'s. The smaller its d_{mean}, the higher its rank. For each particular tract, a fusion percentage was defined to include fibers whose d_{mean}'s were among the top

specified percentage. For example, if we set the fusion percentage as 90%, this means that we keep 90% fibers whose ranks are among the top 90% according to their d_{mean}'s and throw away the rest.

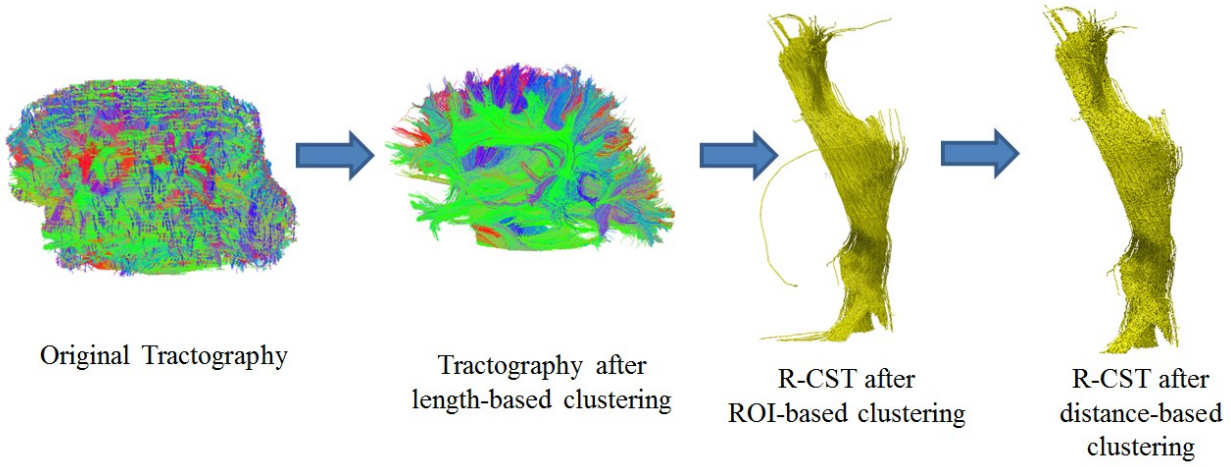

Figure 3-3. Here we show how many of the streamlines generated by the original tractography are filtered to form the corticospinal tract, step by step, through multi-level fiber clustering.

3.6. Results

3.6.1. Cluster Visualization

Figure 3-4 shows how we obtained one example tract - the left arcuate fasciculus - in a test subject – a new subject whose scan was not used to create the fiber atlases. The first row shows the atlas (hand-labeled) versions of the tract. The second row shows the different candidates for this tract in the same test subject, based on using each atlas to decide which fibers it should contain (**Section 3.4.3**). The final result for this tract was obtained by applying the label fusion scheme in **Section 3.5**. It is not hard to see that the label fusion process can help to eliminate

outliers, and it can also add missing fibers to a single candidate labeling of the tract. A manually edited segmentation result is also included for comparison (see the *right bottom panel*).

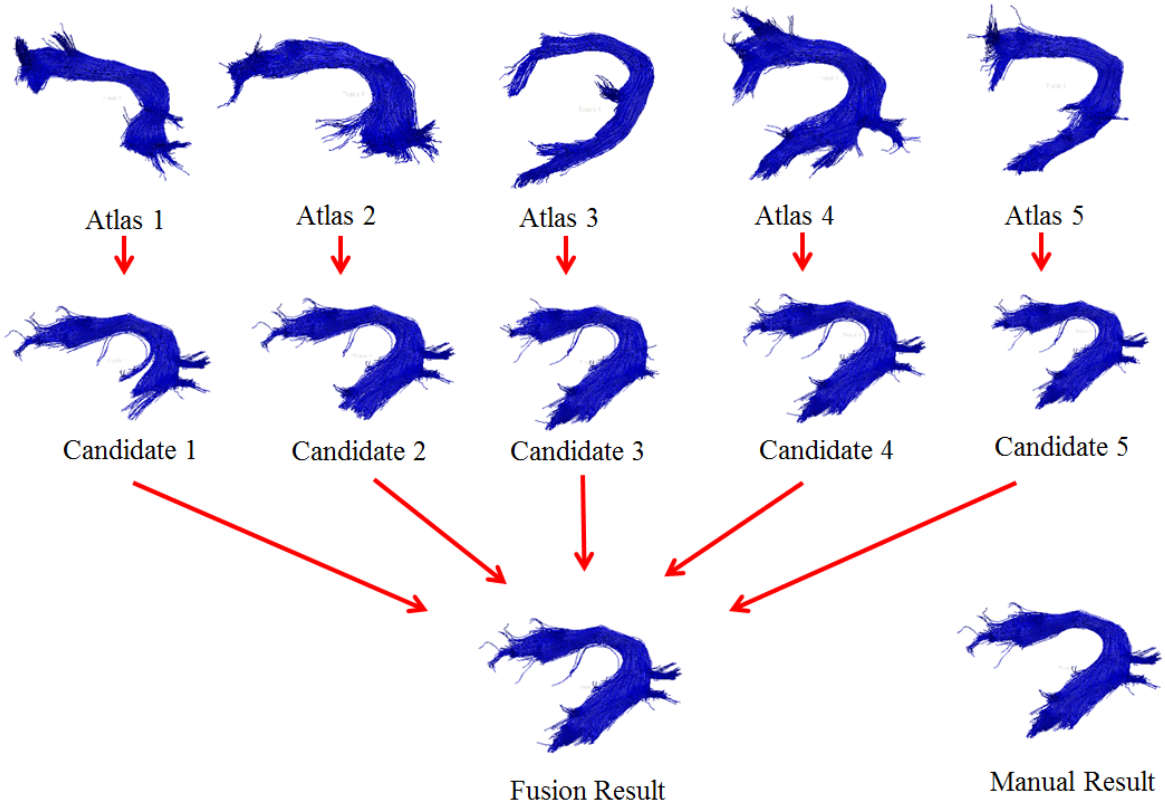

Figure 3-4. Label fusion result obtained from the five manually labeled atlases for the left arcuate fasciculus (in *blue*) in a test subject (viewed from *the left*). A manual segmentation is included for comparison at the *bottom right*.

Figures 3-5 and **3-6** show the label fusion results for the 17 segmented tracts in four randomly selected subjects. Despite individual variations, the overall tract shapes are consistent across the population. **Figure 3-7** shows the combined WM fiber clustering results for the four test subjects. The types of tracts and their colors are as in **Figure 3-2**. The average fiber number in our full set of clustering results is ~40,000 per subject, or roughly 1/10th of the fibers from the

initial tractography. There are three factors that affect how many fibers are included in the final results. First, in this work, we mainly focused on 17 major anatomically well-known white matter tracts. Therefore, only those tracts are shown in **Figure 3-7**. Many other less-known tracts are not shown and could be added in future work, although it might be more challenging to reliably find smaller tracts in the mix of all the other major pathways. Second, streamline whole-brain tractography generates large numbers of false positive fibers and those need to be removed for our ultimate goal – population studies. Last, fiber clustering may show enormous individual variation when applied across a population. However, to perform an effective population study, we only included fibers whose shape shares the most common characteristics throughout the population for each tract. This was our intent when we built our manually constructed atlases. Clearly we would need to admit that some clinically interesting variation is missed by focusing on a set of standard tracts. But finding additional consistent tracts across subjects is challenging and runs the risk of including false positives.

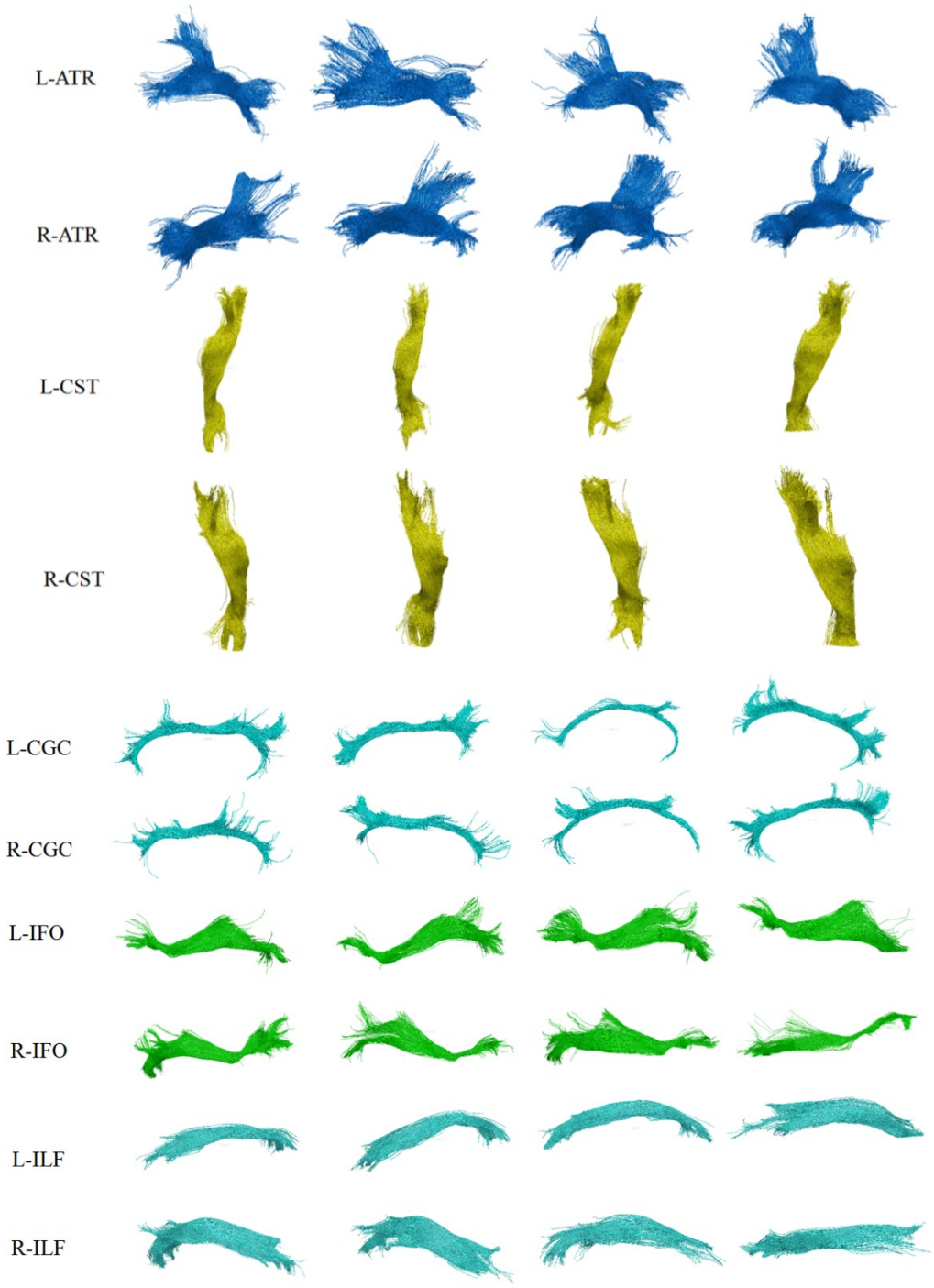

Figure 3-5. Clustering results in four randomly selected subjects for the left and right anterior thalamic radiations (L/R-ATR), the left and right corticospinal tracts (L/R-CST), the left and right cingulums (L/R-CGC), the left and right inferior fronto-occipital fasciculi (L/R-IFO), and the left and right inferior longitudinal fasciculi (L/R-ILF). Tracts on the left side are viewed from *the left*, while the tracts on the right are viewed from *the right*.

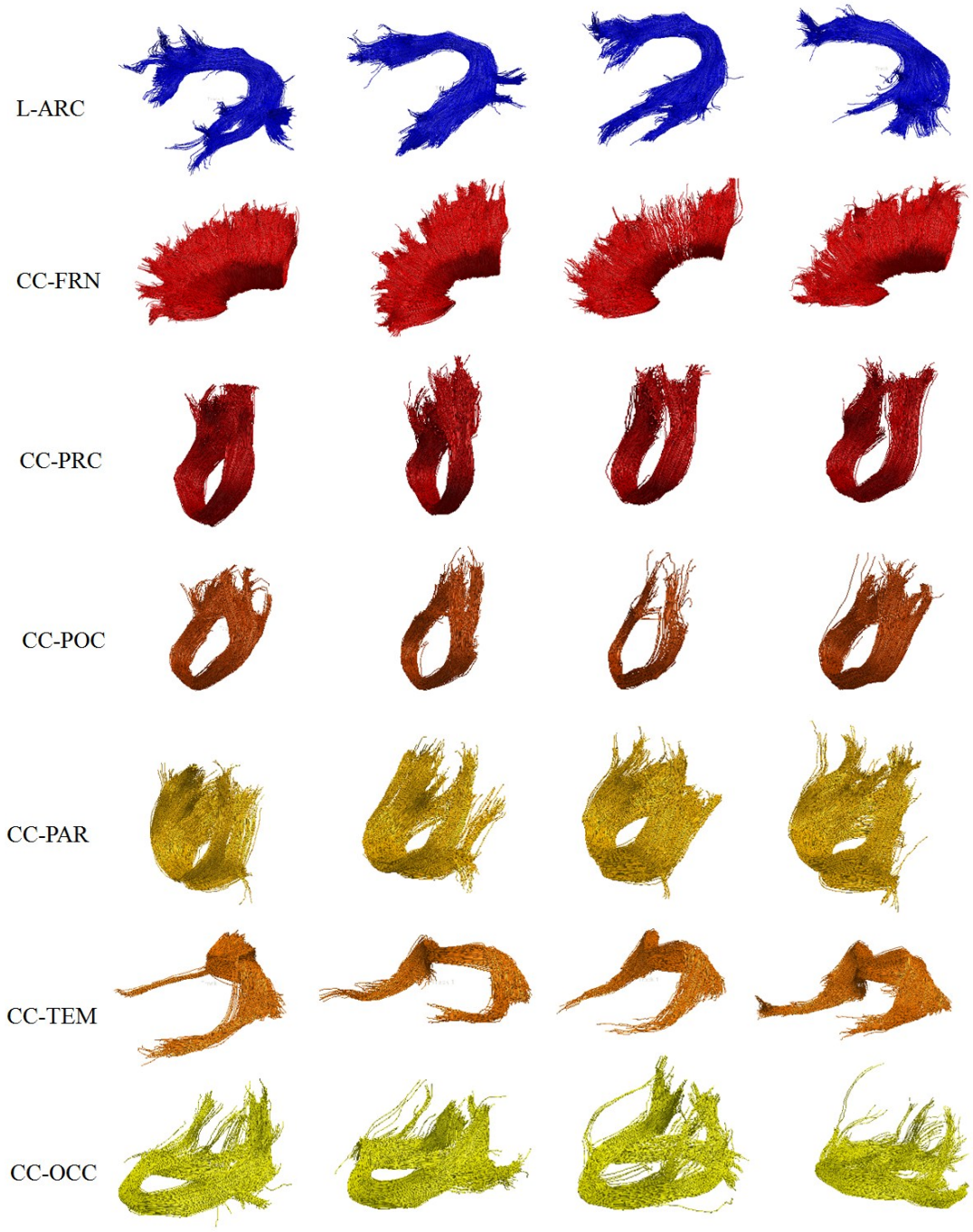

Figure 3-6. Clustering results - for the same four subjects as in **Figure 3-5** - for the left arcuate fasciculus (L-ARC) and six segments of the corpus callosum – projecting to both frontal lobes (CC-FRN), precentral gyri (CC-PRC), postcentral gyri (CC-POC), superior parietal lobes (CC-PAR), temporal lobes (CC-TEM), and occipital lobes (CC-OCC). All the tracts are viewed from *the left*.

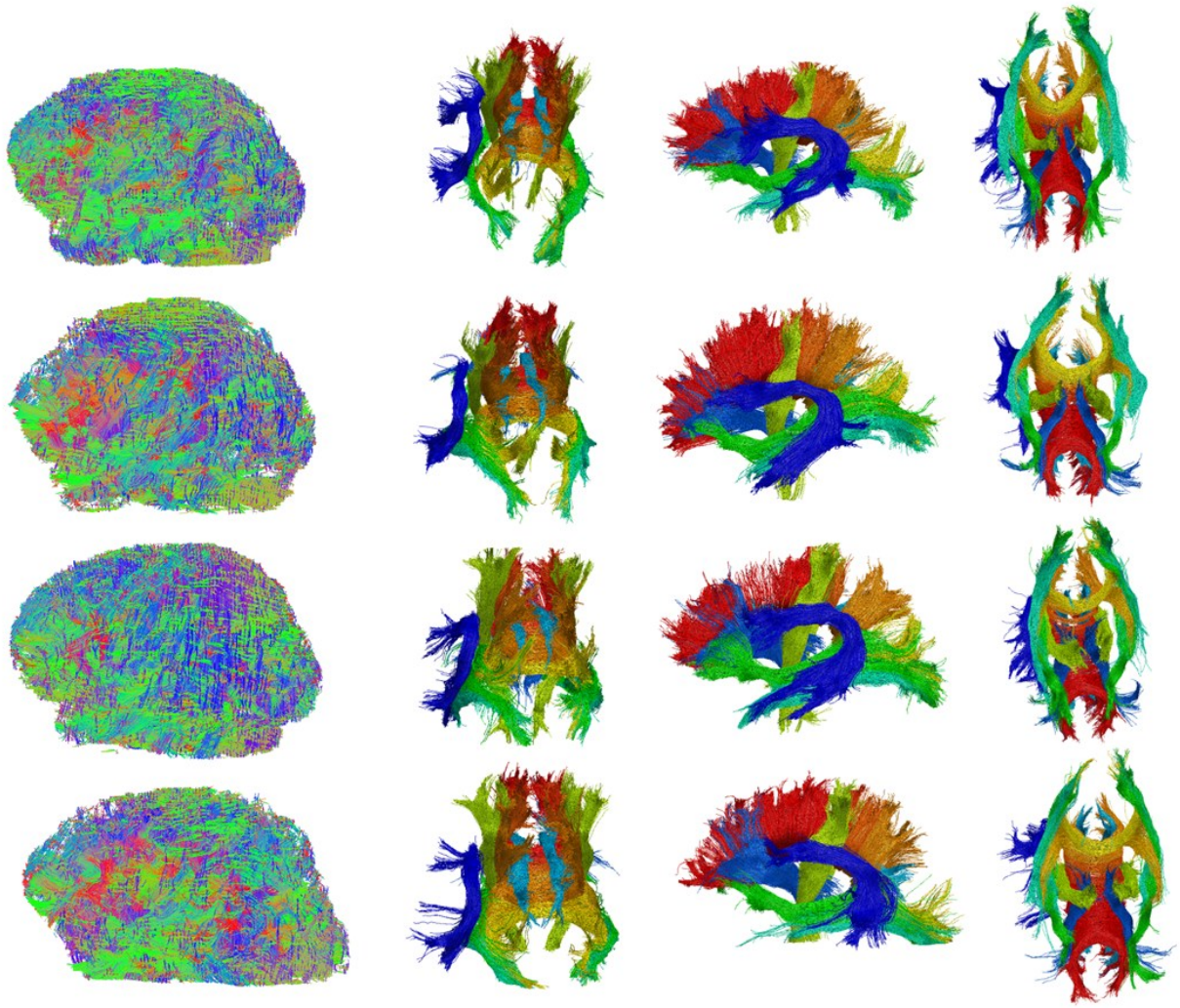

Figure 3-7. *Back*, *left side*, and *bottom* views of the same four subjects' (in **Figure 3-5** and **Figure 3-6**) compositional fiber clustering results are shown. The original whole-brain tractography (the leftmost column) is included for comparison, clearly showing the utility of the data reduction.

3.6.2. Quantitative Validation

To quantitatively evaluate the proposed framework, we converted each of the fiber tracts to a binary image, where voxels that the tracts cross were marked as 1, and 0 otherwise. Then we used the Dice coefficient to assessing the overlap or agreement between two tracts, defined as:

$$D(a,b) = \frac{2*(V(a) \cap V(b))}{V(a)+V(b)} \quad (3.5)$$

where $V()$ is the volume of the region that the tract penetrates.

Due to the wide variability between different tracts, we need to tune the parameters of our algorithm to optimize its performance. We have two key parameters to adjust. One is the Hausdorff distance threshold used to select fibers for each tract per atlas (d_{cutoff} in Equation (3.4)), and the other is the percentage of fibers included in the final label fusion stage described in **Section 3.5**.

In addition to the 5 subjects we used for our manually constructed atlases, we randomly selected another 7 subjects (non-twin pairs, three males and four females) from our data set (12 in total) and manually segmented the 17 tracts mentioned in **Section 3.3**. Initially, we tuned d_{cutoff} and the fusion percentage with the leave-one-out method using the 5 manually labeled atlases. We first used a loose Hausdorff distance bound ($d_{cutoff} = d_{sup}$ in Equation (3.4)), 15 mm, to select the candidate fibers for each tract per atlas so that all the true fibers were included without introducing too many false fibers. Then we optimized the percentage threshold for inclusion in label fusion from 20% to 100% (in increments of 5%) to obtain the optimal percentage (the best Dice coefficients against manual segmentation). Next, we varied the Hausdorff distance threshold (d_{cutoff}) from 3 mm to 15 mm (in increments of 1 mm) to decide the optimal distance, while the optimal fusion percentage was used from the previous step. The optimal parameters for each tract are shown in **Table 3-1**. The optimized parameters were then

applied to the seven randomly selected subjects as the test data. **Figure 3-8** compares the average Dice coefficients of all clustered tracts between the training data set and the test data. The error bars stand for the standard deviation of the Dice coefficients for each tract. Not surprisingly, the training data outperformed the test data for almost all the tracts, except for the left fronto-occipital fasciculus (L-IFO). **Figure 3-9** shows the average Dice coefficients for all tracts with our label fusion method and ROI-only clustering (based on the look-up table in Zhang *et al*., 2010), against manual segmentation for the test subjects only. Overall, our algorithm outperformed the ROI method for every tract, and also gave a smaller variance, especially for those tracts that have unclear or loose ROI constraints (CGC, ILF, and CC-TEM).

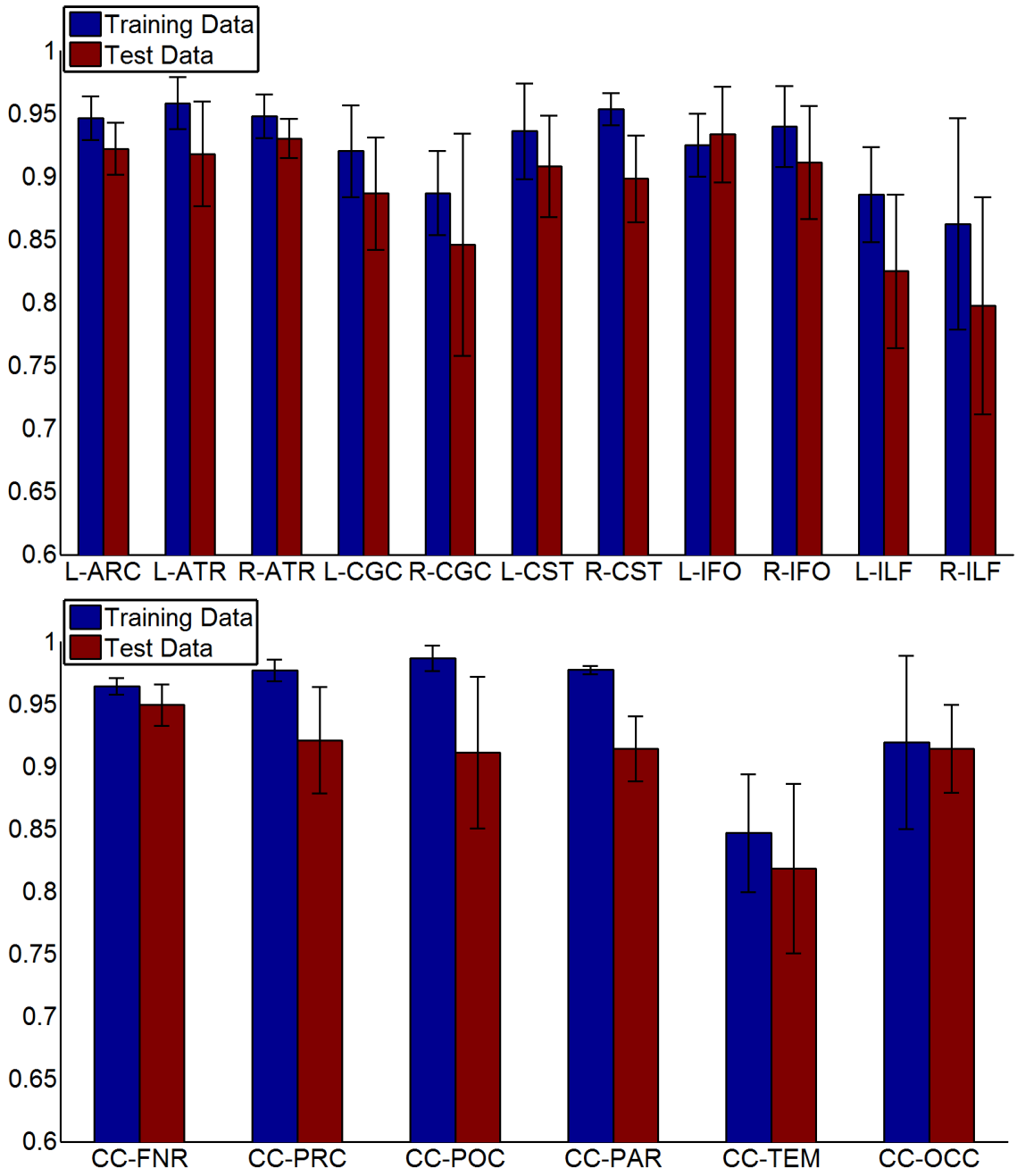

Figure 3-8. Average Dice coefficients of all the tracts described in **Section 3.3** for the training data set (five manually constructed atlases by the leave-one-out test) and the test data set (the average of seven randomly selected subjects from our data set) using our label fusion method against manual segmentation. The general pattern of coefficients above 0.8 indicates good agreement of automatically segmented and hand-segmented tracts.

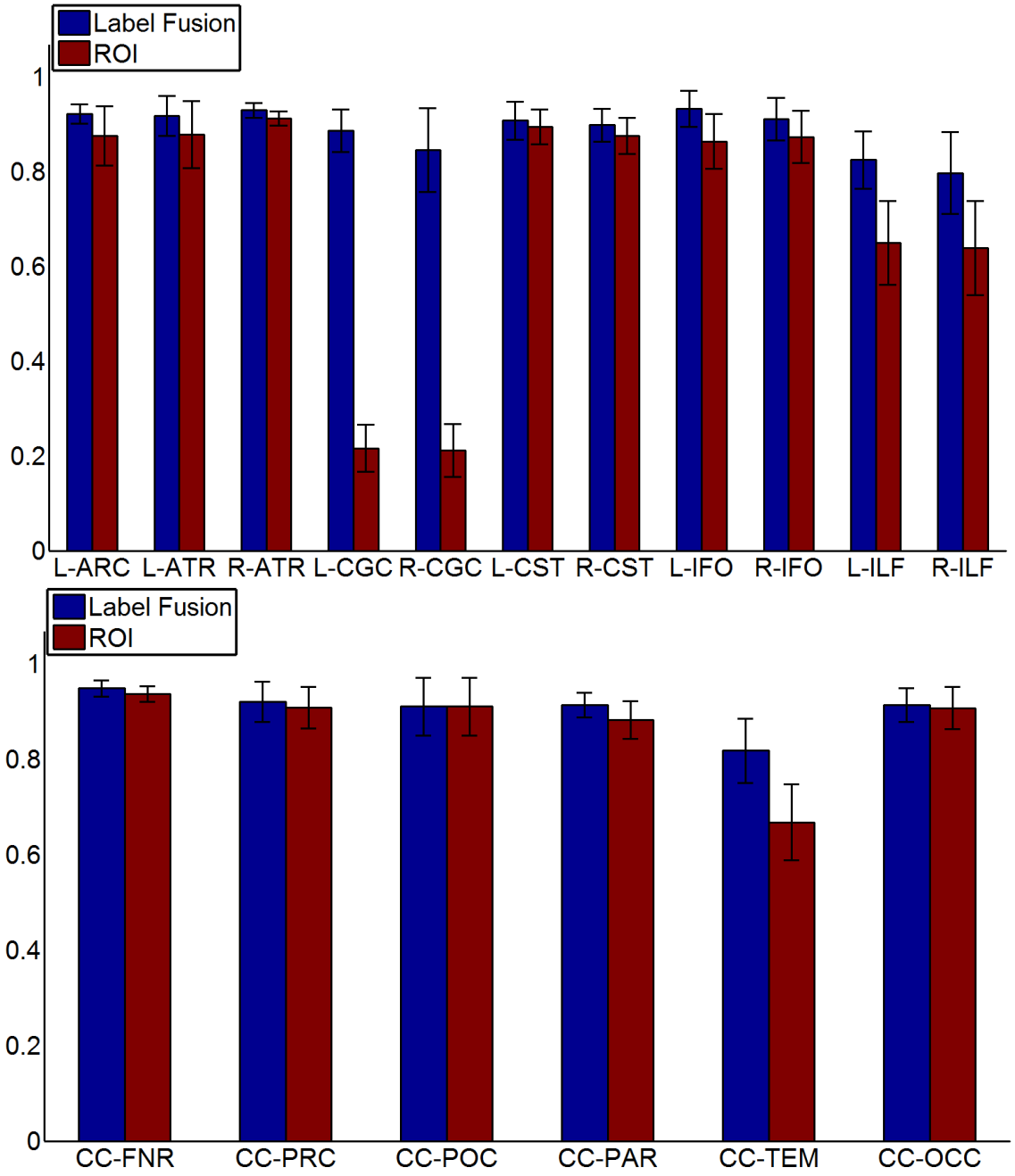

Figure 3-9. The average Dice coefficients of all the tracts described in **Section 3.3** for our label fusion method and the ROI method against manual segmentation. The label fusion method universally performs very well (dark blue bars), even when the ROI method (red) performs poorly.

Table 3-1. The values of the clustering distance threshold and the fusion percentage for each tract described in **Section 3.3** that were used to cluster the 198 subjects in our data set.

Tract Name	L/R-ATR	L/R-CGC	L/R-CST	L/R-IFO	L/R-ILF	L-ARC	CC-FRN	CC-PRC	CC-POC	CC-PAR	CC-TEM	CC-OCC
d_{cutoff} (mm)	12	12	12	12	12	12	12	12	12	12	12	12
Fusion Pct. (%)	100	85	95	95	70	95	90	95	100	95	45	100

3.6.3. Clustering Parameter Selection

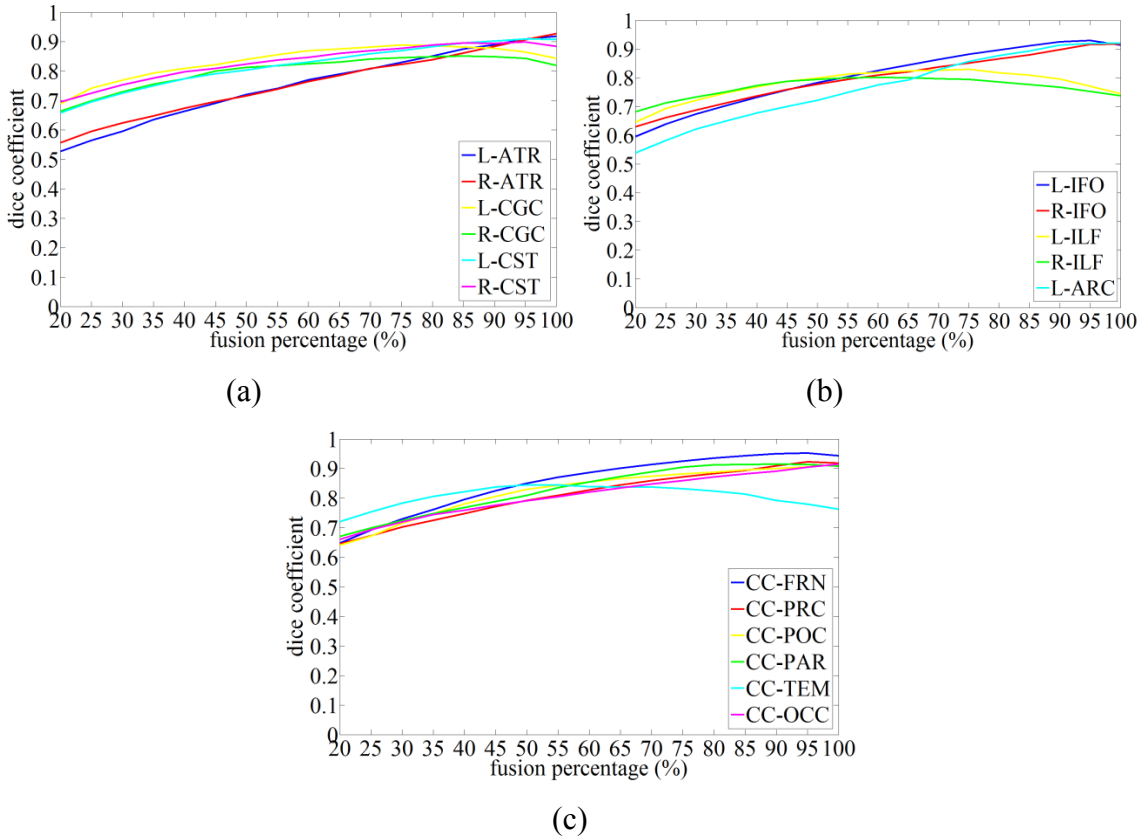

Figure 3-10. Changes in the average Dice coefficients are shown, over the seven test subjects against the fusion percentages that were applied in the label fusion stage (**Section 3.5**) for all the tracts described in **Section 3.3**.

To rationalize our choice of the two key parameters, the fusion percentage and the clustering distance threshold (d_{cutoff}), here we examined how the clustering performance varied with these two parameters. **Figures 3-10(a-c)** show the changes in the average Dice coefficients over the 7 test subjects used for each tract, respectively, when the fusion percentages increase from 20% to 100%, that is, choosing the top 20% to 100% ranked candidate fibers obtained from the 5 manually constructed atlases, based on the mean clustering distance defined in Equation (3.4), where $d_{cutoff} = d_{sup}$ = 15mm.

A high fusion percentage leads to fewer missing or false negative fibers from the candidates obtained from other manually constructed atlases. However, a high fusion percentage will also include more false positive fibers from all the candidates. Tracts that have helpful constraints based on ROIs (ATRs, CGCs, CSTs, IFOs, L-ARC, CC-FRN, CC-PRC, CC-POC, CC-PAR, and CC-OCC) usually have fewer false positives in each candidate. Therefore, the benefit of reducing the false negatives tends to overwhelm the gain in false positives when the fusion percentage goes up. Dice coefficients increase until they hit plateaus between 85% and 100%; however, for those tracts whose ROI constraints are relatively loose (IFOs and CC-TEM), the plateaus come much sooner when the fusion percentages are still relatively low (less than 70%). This is because eliminating more false positive fibers in each candidate is more critical for maintaining a high Dice coefficient. The percentages listed in **Table 3-1** were therefore adopted for all the subjects in our data set.

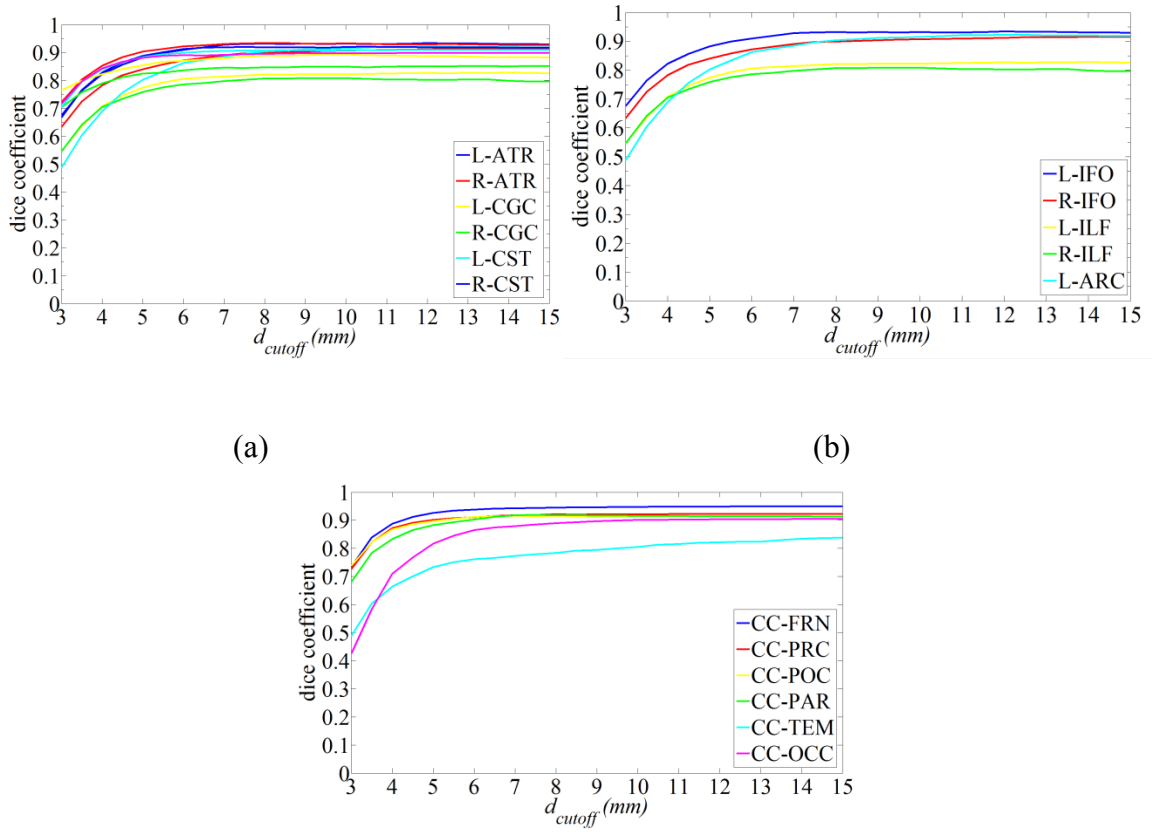

Figure 3-11. The changes of the average Dice coefficient in seven test subjects versus the clustering distance threshold (d_{cutoff}) (**Section 3.4.3**) for all the tracts described in **Section 3.3**. Here, the optimal values of the fusion percentage (shown in **Table 3-1**) were selected.

Figure 3-11(a-c) show the change of the average Dice coefficients versus the cutoff clustering distances d_{cutoff}, when the fusion percentages are fixed at the values listed in **Table 3-1**. It seems that the average Dice coefficients become stable after d_{cutoff} > 10mm. This is probably because a smaller d_{cutoff} is too conservative and excludes too many true fibers. Hence, we chose d_{cutoff} = 12mm uniformly for all the tracts, which corresponded to the percentage of fibers eliminated during manual labeling of the atlases for the given tract.

3.6.4. Label Fusion vs. Single Atlas

Label fusion-based segmentation methods take advantage of the information of multiple atlases and generally outperform methods that only use a single atlas. We listed the mean Dice coefficients against manual segmentation between label fusion clustering and single atlas clustering in **Table 3-2**. The parameters of label fusion clustering were chosen as in **Table 3-1**. The mean Dice coefficients were computed over the 7 test subjects chosen in **Section 3.6.2**. For comparison, we calculated Dice coefficients using a single atlas out of the 5 manually constructed atlases with d_{cutoff} = 12mm. The single-atlas mean Dice coefficients were averaged over all the 5 atlases and all the 7 test subjects (35 combinations) per tract. **Table 3-2** justifies fusing multiple atlas results in cases where the performance of a single atlas is well below the average performance of all the five atlases.

Table 3-2. The average Dice coefficients and their standard deviations over the seven test subjects against manual segmentation for label fusion on the five manually labeled atlases and only a single atlas being used (the average was computed over the five atlases).

Mean Dice ± Standard Deviation						
Tract Name	L-ATR	R-ATR	L-CGC	R-CGC	L-CST	R-CST
Label Fusion	0.92 ± 0.04	0.93 ± 0.02	0.88 ± 0.04	0.85 ± 0.09	0.91 ± 0.04	0.90 ± 0.03
Single Atlas Avg.	0.88 ± 0.05	0.90 ± 0.05	0.88 ± 0.04	0.84 ± 0.08	0.91 ± 0.04	0.89 ± 0.04
Tract Name	L-IFO	R-IFO	L-ILF	R-ILF	L-ARC	
Label Fusion	0.93 ± 0.04	0.91 ± 0.04	0.82 ± 0.06	0.80 ± 0.09	0.92 ± 0.02	
Single Atlas Avg.	0.92 ± 0.04	0.89 ± 0.06	0.80 ± 0.04	0.78 ± 0.09	0.86 ± 0.06	
Tract Name	CC-FRN	CC-PRC	CC-POC	CC-PAR	CC-TEM	CC-OCC
Label Fusion	0.95 ± 0.02	0.92 ± 0.04	0.91 ± 0.06	0.91 ± 0.03	0.81 ± 0.07	0.91 ± 0.04
Single Atlas Avg.	0.95 ± 0.02	0.92 ± 0.05	0.90 ± 0.06	0.91 ± 0.03	0.81 ± 0.06	0.89 ± 0.05

3.6.5. Number of Atlases

How many atlases should be used in the label fusion scheme is always an open question. Among other examples, Chou *et al*. (2007, 2008, 2009) studied this for the case of lateral ventricular segmentation on standard anatomical MRI. In our case, we performed an experimental analysis to explore the choice of atlas number. We used the twelve subjects (including the five atlases) in **Section 3.6.2** in our analysis. The five atlases plus two more additional subjects formed our atlas pool. We calculated the average dice coefficients between

the clustering results of the rest of the five subjects against their manual segmentations while we used 1, 2, 3, 5, and 7 atlases from our pool. The atlas selection was random. The clustering parameters were chosen as the same as those in **Table 3-1**. The results are shown in **Table 3-3**. The Dice coefficients of L-ATR and R-ATR increased 8%~9% from a single atlas to two atlases and continued going up as more atlases were used. For R-CGC, L-ILF, CC-TEM, and CC-OCC, the Dice coefficients seemed to be benefited with more atlases, too. Overall, the Dice coefficients approaches stable after three atlases, while more atlases didn't decrease the Dice coefficients. However, by considering our small test sample size and balancing the tradeoff between stability and computation cost, five atlases may be suitable to be representative of our data set. Based on the validation results in **Section 3.6.2**, the five atlases we selected could effectively cluster the tracts for new subjects in our data set.

Table 3-3. The average Dice coefficients over five test subjects against manual segmentation for different numbers of atlases applied.

Mean Dice Coefficients					
# of Atlases	1	2	3	5	7
L-ARC	0.901	0.897	0.906	0.914	0.920
L-ATR	0.833	0.908	0.910	0.919	0.919
R-ATR	0.829	0.898	0.927	0.928	0.927
L-CGC	0.872	0.883	0.875	0.878	0.878
R-CGC	0.859	0.880	0.876	0.870	0.877
L-CST	0.921	0.917	0.914	0.911	0.911
R-CST	0.899	0.903	0.902	0.903	0.902
L-IFO	0.933	0.940	0.938	0.934	0.930
R-IFO	0.911	0.910	0.910	0.902	0.906
L-ILF	0.797	0.797	0.815	0.811	0.823
R-ILF	0.800	0.786	0.789	0.794	0.797
CC-FRN	0.943	0.947	0.946	0.946	0.945
CC-PRC	0.916	0.914	0.913	0.912	0.913
CC-POC	0.903	0.901	0.903	0.903	0.903
CC_PAR	0.908	0.902	0.906	0.908	0.907
CC-TEM	0.782	0.787	0.796	0.797	0.829
CC-OCC	0.897	0.911	0.911	0.912	0.911

3.7 Discussion

It is obvious that tract clustering quality is influenced by the quality of tractography. A better tractography algorithm that produces fewer false fibers makes clustering easier and more accurate. The whole-brain tractography methods place seeds throughout the brain and produce streamlines in a short period of time. However, many false fibers are created, for example, in the left and right inferior longitudinal fasciculi and the temporal segment of the corpus callosum, as there are multiple fiber crossings in the regions traversed by those tracts. Since our purpose was to perform large scale population studies, we were inclined to be more conservative and keep only fibers that form a consistent tract shape across the population. When we picked a

representative sample for a particular tract, we followed the same principle. For example, the cingulums have many branches along their way from the frontal lobe to the temporal lobe. We removed those branches in our representative tract samples for population studies. It is not practical to find corresponding fibers for those branches across the population. We only studied the common areas across most subjects.

While our methods achieved robust performance in fiber clustering, it is important to note there are many parameters that could be tuned in whole-brain tractography, which no doubt could potentially affect the final clustering results. First, tractography is based on mathematical input models, such as tensor, ODF, fiber orientation density (Tournier *et al*., 2004), etc.; then, tractography can be deterministic or probabilistic (e.x. PICo); next, in terms of tracking algorithms, it can be fiber assignment by continuous tracking (FACT) (Mori *et al*., 1999), Euler (Basser *et al*., 2000), Runge-Kutta (Basser *et al*., 2000), tensor deflection (TEND) (Lazar *et al*., 2003), etc.; as to interpolation algorithms, it may be nearest-neighbor, linear, TEND, etc..; finally, multiple stopping criteria can be chosen, such as masking, fiber maximum turning angle, the lowest anisotropy to terminate tracking, etc.. Furthermore, there are many tractography software packages available for brain imaging research (DTI Studio, Diffusion Toolkit, Camino, MRtrix, etc.). Each package might produce slightly different tractography results. Because of the lack of ground truth, the problem of selecting the parameters and software packages for optimal clustering performance needs more dedicated exploration and will be important future work.

In our multi-level fiber clustering algorithm (**Section 3.4**), non-linear FA registration was used to align fibers between the atlases and the subjects. Ideally, an ODF-based registration method might be used to reorient the fibers between different spaces. However, such a registration scheme would have much larger cost in terms of computing resources and time (a few hours per registration) if it were performed on a large-scale, as in the label fusion scheme. In contrast, FA registration takes only around 5 minutes per registration on our data set. Moreover, we have found that fiber alignment is indeed improved significantly with FA-based elastic registration (**Chapter 2** or Jin *et al*., 2011*a*).

It is always difficult to compare different clustering algorithms quantitatively as we lack ground truth for both the tractography and the white matter segmentation. Even though their relative accuracy is hard to assess, it is easier to point to some conceptual similarities and differences among the various approaches that have been proposed for tract clustering. Many "bottom-up" methods (e.g., Gerig *et al*., 2004; Xia *et al*., 2005; O'Donnell and Westin, 2007; Maddah *et al.*, 2008; Visser *et al*., 2010) use the relationship between neighboring fibers in one single subject and apply standard clustering algorithms to segment the tracts individually. These methods can assign each and every extracted fiber to a class, which means all the fibers are retained and represent WM variability in an individual. Even so, they do not necessarily yield a method to match tracts across subjects – a step commonly needed for large-scale population studies. In other words, if clustering is applied independently to data from numerous individuals, there may be no easy way to match the tracts across subjects or find correspondences. On the other hand, "top-down" methods (Wakana *et al*., 2007; Li *et al*. 2010; Zhang *et al*., 2010) impose ROI constraints to effectively filter out a massive number of false positive streamlines generated

by tractography. The tracts segmented may also have a clearer anatomical interpretation, as known ROIs are used to define them. This then offers a common set of tracts, enabling population studies. Still other methods (Maddah *et al.*, 2008; Wassermann *et al*. 2010; Wang *et al*., 2012; Guevara *et al*. 2012) were driven by elegant mathematical/statistical models. However, many of these methods have not been used or widely tested in clinical research.

The contribution of our paper is to take account of individual variability by constructing multiple white matter atlases. A top-down method is also used to extract anatomically meaningful tracts. We will also propose a novel fiber correspondence scheme to show how to use our clustering results to answer real-world biological questions (**Chapter 4** and **Chapter 5**).

CHAPTER 4

Genetic Heritability

4.1. Introduction

The relationship between genetics, brain structure, and function has long been debated in various disciplines such as medicine, sociology, education, and neuroscience. How is the brain influenced by nature (genetics) and nurture (environment)? Many studies have addressed this question from different perspectives. In early structural MRI studies of twins, Thompson *et al*. (2001) and Wright *et al.* (2002) created 3-D maps and regional estimates of genetic effects on cortical gray matter measures, and parcellated regions of interest. More recently, Hulshoff *et al*. (2006) found that there is some overlap in the genes that affect regional brain measures (such as gray and white matter densities) and intelligence.

Most prior studies regarding heritability of brain structures were based on T1-weighted anatomical MRI; however, T1-weighted MRI cannot provide information on white matter fiber tracts in the brain. For two decades, diffusion tensor imaging (DTI) has been increasingly used to study pathology and connectivity of white matter pathways. DTI offers directional information on the diffusion of water molecules in brain tissue. Fractional anisotropy (FA), as a measure of microstructural directionality, tends to be higher when fiber tracts are more directionally coherent. Recent genetic analyses of DTI have found moderately high heritability for several diffusivity measures including the FA (Chiang *et al*., 2011), which is also widely considered a measure of fiber integrity. Specific genes have recently been discovered that influence FA

(Braskie *et al*., 2011). Structural equation models and heritability analyses have also been extended to handle the full diffusion tensor (Lee *et al*., 2010), and orientation density functions (ODFs) that represent the diffusion process (Leporé *et al*., 2010).

The major disadvantage of voxel-based analysis of FA values is that their subtle subvoxel effects that occur along a fiber tract cannot be observed, and tract geometry is overlooked. It is impossible to relate the geometric characteristics of tract shape to genetics solely from an FA map. Most recently, Brouwer *et al.* (2010) assessed genetic and environmental influence on fiber tracts in children by constructing average fiber bundles based on manually defined regions of interest; nevertheless, the manual seeding of tracts makes it hard to analyze a large dataset, and limits the coverage to a few tracts.

We illustrate our method to study tract heritability based on the clustering results from our algorithm (**Chapter 3**). As individual WM fiber tracts are highly variable in shape, it can be difficult to find corresponding fibers that belong to the same tract across a population. Recent studies examined the skeleton of tracts, with methods such as tract-based spatial statistics (TBSS) (Smith *et al*., 2007; Bodini *et al*., 2009) or the average fiber tracts (Brouwer *et al*., 2010; Prasad *et al*., 2011) to perform statistical analyses of diffusion parameters in a large population. Nevertheless, these approaches do not always retain the full 3-D profile of information from the tracts. To address this, we use a point-wise tract correspondence method to study clustered tract parameters in 3-D. We calculate heritability statistics from corresponding tract points to

understand genetic influences on the brain's tracts, and to demonstrate a practical use of our entire workflow.

4.2 Subjects and Image Acquisition

We analyzed a dataset from 198 healthy young adult twins (mean age: 23.2 +/- 2.1SD) from 99 families in Australia. All twins were right-handed. No subjects had any major medical condition or psychiatric illness. All subjects were evaluated to exclude any pathology known to affect brain structure. Diffusion imaging was available in 99 complete pairs – 62 monozygotic pairs (21 male-only pairs) and 37 same-sex dizygotic twin pairs (12 male-only pairs).

High angular resolution diffusion imaging (HARDI) scans were acquired with a 4T Siemens Bruker Medspec MRI scanner, using single-shot echo planar imaging with parameters: TR/TE = 6090/91.7ms, 23cm FOV, and a 128x128 acquisition matrix. Each 3-D volume consisted of 55 2-mm axial slices, with no gap, and 1.79x1.79mm^2 in-plane resolution. 105 image volumes were acquired per subject: 11 with no diffusion sensitization, i.e., T2-weighted b_0 volumes, and 94 diffusion-weighted volumes (b = 1159 s/mm^2). The raw HARDI images were corrected for eddy-current induced distortions with FSL (www.fmrib.ox.ac.uk/fsl/). The gradient table that represented the diffusion scanning angles was adjusted accordingly.

4.3. Methods

4.3.1. Fiber Matching

To perform group studies, we first need to establish some kind of correspondence between fibers of the segmented tracts across the population. For each tract, we chose a representative sample among our manually constructed atlases. The representative sample was then projected into individual new subject space as follows. After applying the registration warp (**Section 3.4.2)** to the representative tract, we defined the corresponding point in the new subject space for each point in the sample tract. The corresponding point was defined as the point in the new subject tract closest to the warped sample point, if such a point exists within a given neighborhood, or the original sample projection, if not. An illustration of fiber matching is shown in **Figure 4-1.**

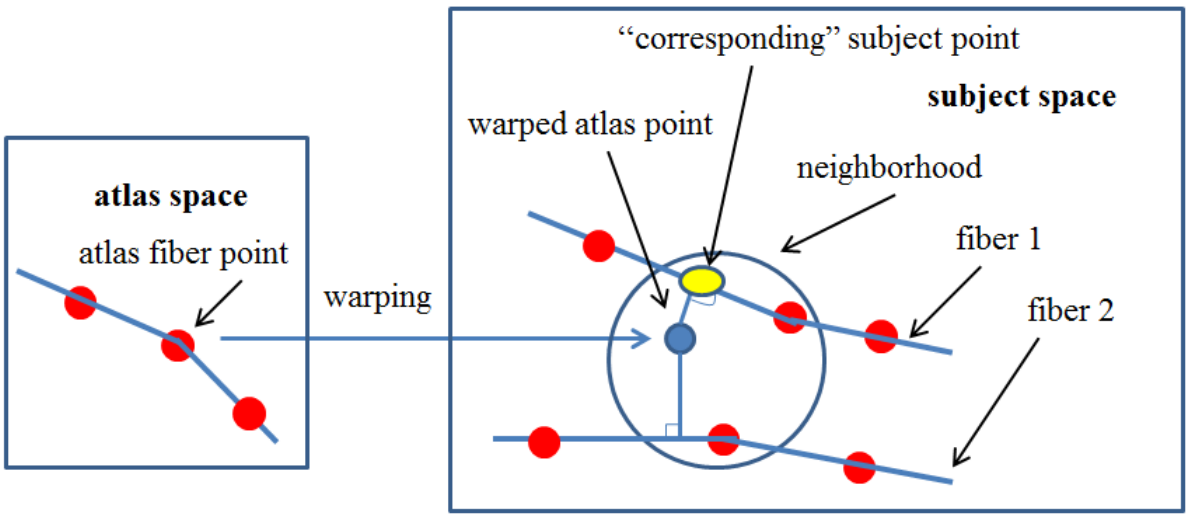

Figure 4-1. An illustration of tract projection**.**

4.3.2. Genetic Analysis

Monozygotic (MZ) twins share 100% of their genetic variants whereas dizygotic (DZ) twins share, on average, 50% of their genes. A simple and widely-used estimate of heritability in twin studies is to assess how much the intra-class correlation for MZ twin pairs (r_{MZ}) exceeds the DZ twin correlation (r_{DZ}). Falconer's heritability statistic (Falconer and Mackay, 1996) is defined as:

$$h^2 = 2(r_{MZ} - r_{DZ}) \tag{4.1}$$

The statistic estimates the proportion of the overall variance due to genetic differences among individuals. Of course more sophisticated structural equation models can be used, but here the main purpose was just to give an example of a statistical manipulation of the tracts, to compute a statistic of interest. Jin *et al*. (2011*b*) used the mean and the standard deviation of the Euclidean distances between individual fibers and the mean curve for a particular tract as metrics, where the mean distance is related to the tract thickness. Here, interpolated FA values at corresponding tract points (from **Section 4.3.1**) were used to calculate intra-class correlations r_{MZ} and r_{DZ}.

To account for the multiple comparisons problem that arises when testing a statistical hypothesis at every fiber point, the false discovery rate (FDR) was used (Benjamini and Hochberg, 1995) at the conventional 5% level to provide corrected critical p values for the maps of r_{MZ} and r_{DZ} in Falconer's heritability statistic. r_{MZ} and r_{DZ} whose associated p values were larger than 0.05 were set to 0. The Falconer's heritability statistic h^2 was computed from r_{MZ} and r_{DZ} at points whose p-value passed FDR.

4.4. Results

4.4.1 Genetic Analysis

For each tract, we selected a representative example among our 12 subjects with manually segmented tracts in **Section 3.6.2**. We projected the tract representation to the remaining 197 subjects, following **Section 4.3.1.** The search range was a 10-mm radius sphere. The FA values at sub-voxel fiber points were used to calculate r_{MZ} and r_{DZ} for a particular tract. Falconer's heritability statistic on FA was computed from Equation (4.1). To make the computation easier, we uniformly resampled each fiber at 15 equidistant points and reduced the number of fibers in the representative tract, ensuring that the region enclosing the original tract was still covered entirely by the remaining fibers.

Figure 4-2, **4-3**, and **4-4** show Falconer's heritability statistics on FA after correcting for multiple comparisons with FDR. As heritability must be positive and lies between 0 and 1, Falconer's heritability statistics were set to 0 if their estimator was negative and 1 if it was greater than 1. Locations in red show greater genetic influence than those in blue. The percentages of points with high genetic influence (set arbitrarily to $h^2 > 0.7$) for each tract described in **Section 3.3** are also listed in **Table 4-1**. Genetic factors tend to have greater influence on the tracts on the left side than the right side (ATR, CGC, CST, and ILF), except for the IFO.

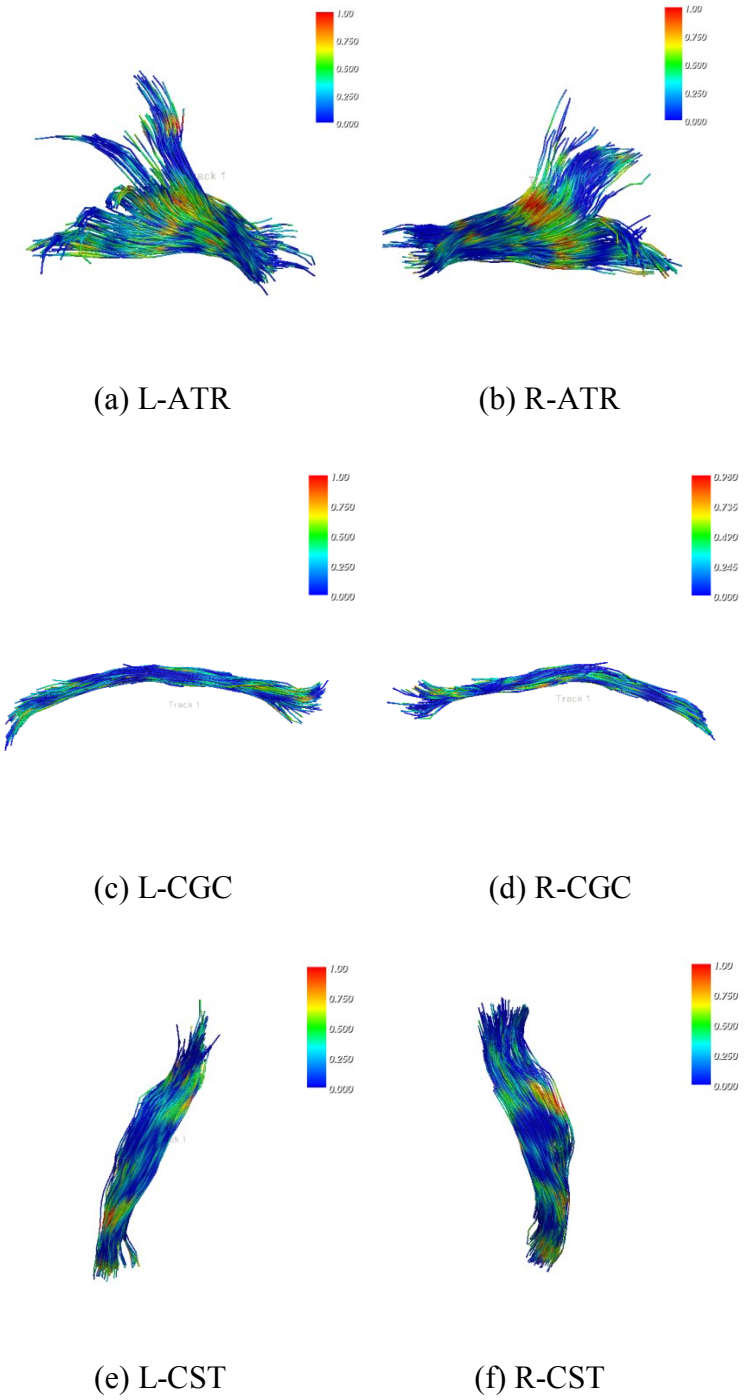

(a) L-ATR (b) R-ATR

(c) L-CGC (d) R-CGC

(e) L-CST (f) R-CST

Figure 4-2. Color maps of Falconer's heritability statistic on FA for (a) the left anterior thalamic radiation, (b) the right anterior thalamic radiation, (c) the left cingulum, (d) the right cingulum, (e) the left corticospinal tract, and (f) the right corticospinal tract. Warmer colors show regions with higher genetic influence ($h^2 \sim 1$). Tracts on the left side are viewed from *the left*, while the tracts on the right are viewed from *the right*.

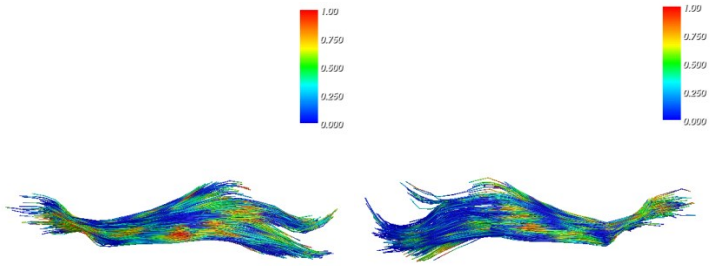

(a) L-IFO (b) R-IFO

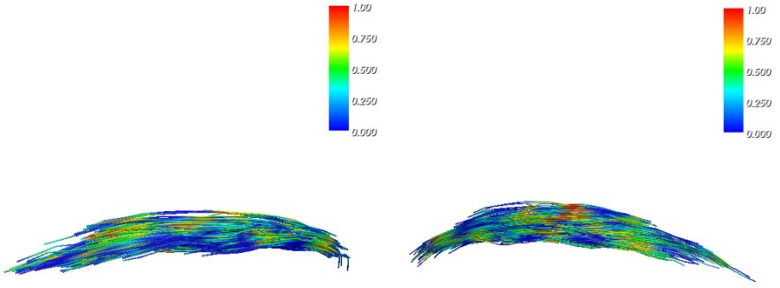

(c) L-ILF (d) R-ILF

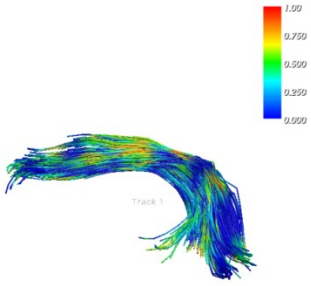

(e) L-ARC

Figure 4-3. Color maps show Falconer's heritability statistic on FA for (a) the left inferior fronto-occipital fasciculus, (b) the right inferior fronto-occipital fasciculus, (c) the left inferior longitudinal fasciculus, (d) the right inferior longitudinal fasciculus, and (e) the left arcuate fasciculus. Warmer colors show regions with higher genetic influence ($h^2 \sim 1$). Tracts on the left side are viewed from *the left*, while the tracts on the right are viewed from *the right*.

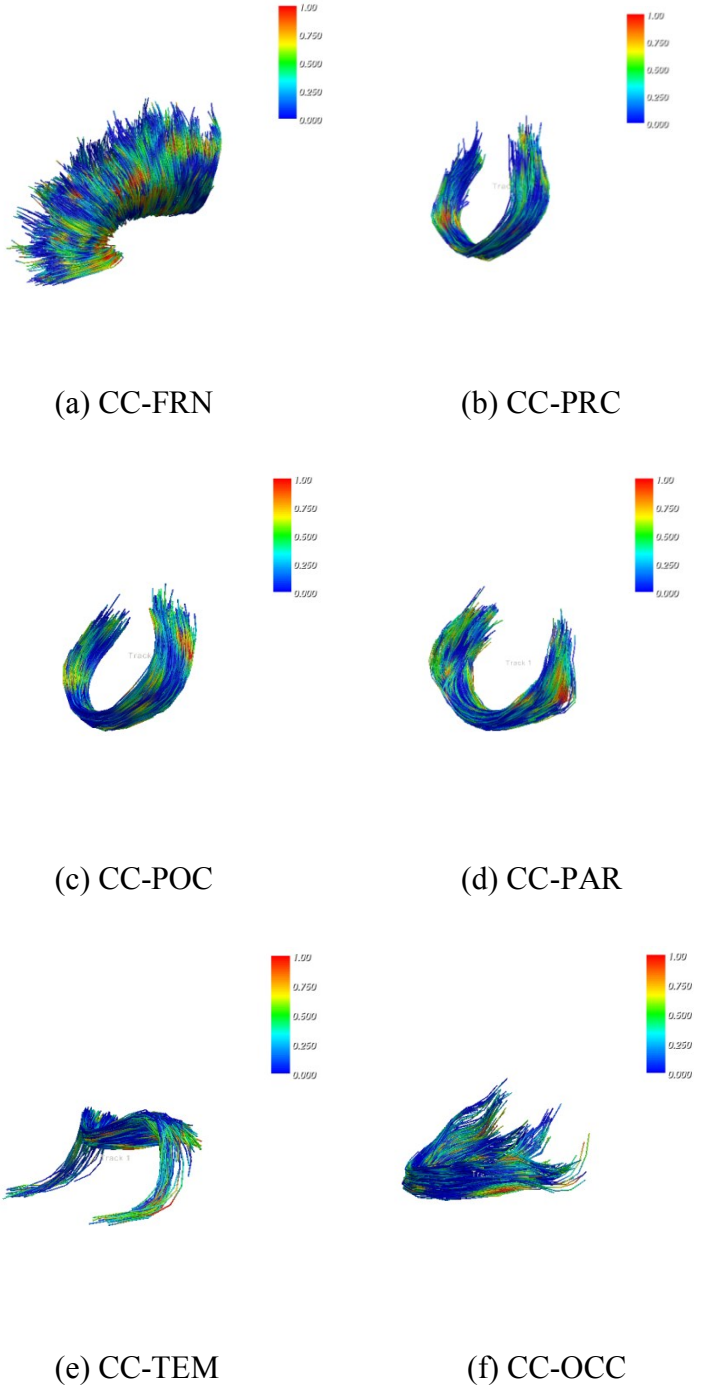

(a) CC-FRN (b) CC-PRC

(c) CC-POC (d) CC-PAR

(e) CC-TEM (f) CC-OCC

Figure 4-4. Color maps of Falconer's heritability statistic on FA for the six segments of the corpus callosum – projecting to both (a) frontal lobes, (b) precentral gyri, (c) postcentral gyri, (d) superior parietal lobes, (e) temporal lobes, and (f) occipital lobes. Warmer colors show regions with higher genetic influence ($h^2 \sim 1$). All of the corpus callosum segments are viewed from *the left*.

Table 4-1. The percentage of fiber points in all clustered tracts where high genetic influence is detected (arbitrarily set to $h^2 > 0.7$). The high genetic influence detected in the frontal regions of the corpus callosum (CC-FRN) may reflect its generally higher FA, which tends to lead to higher SNR for statistical analysis.

Tract Name	L-ATR	R-ATR	L-CGC	R-CGC	L-CST	R-CST	L-IFO	R-IFO	L-ARC
Pct. (%)	8.6	7.1	4.2	1.2	7.8	4.5	15.4	13.6	7.8
Tract Name	L-ILF	R-ILF	CC-FRN	CC-PRC	CC-POC	CC-PAR	CC-TEM	CC-OCC	
Pct. (%)	7.7	11.2	17.5	7.9	6.2	4.6	5.6	6.8	

4.4.2. Stability Analysis

Falconer's heritability statistic is defined as twice the difference between the MZ intra-class correlation and the DZ intra-class correlation as described in Equation (4.1). The intra-class correlations are associated with the variances between and across members of pairs of twins in each group. One important consideration is that the estimated heritability (or any other statistic) needs to be robust to the details of parameter selection – for example, it may change as the interpolated FA values of the corresponding fibers points change if different radii of sphere are chosen to find corresponding points for each tract across the population. We evaluated the stability of Falconer's heritability statistic for each tract by computing the percentage of fiber points whose Falconer's heritability statistics change by less than 0.2 (this is admittedly arbitrary) when changing the radius of the sphere used to search for corresponding points across the population (those familiar with the tract-based spatial statistics (TBSS) method will note that a similar dependency may arise for the cross-subject correspondences used in TBSS). **Table 4-2** lists the stability of Falconer's heritability statistics for all clustered tracts when the radius of the

search sphere changes from 5 mm to 10 mm to 15 mm. Overall, Falconer's heritability statistic is stable for most tracts except CC-TEM. Therefore, the results in **Section 4.4.1** do provide somewhat robust information on genetic influences for each tract. As the number of twin pairs increases, the Falconer's heritability should have tighter confidence limits. The relatively low stability of CC-TEM arises because the clustering result for the CC-TEM bundle has a large variance (its Dice coefficient in **Section 3.6.2** is also the lowest). This is perhaps due to the large variations in the tractography results in that area.

Table 4-2. The stability of Falconer's heritability statistic (the percentage of points in the tract whose Falconer's heritability statistic changes by less than 0.2) with changes in the spherical neighborhoods (radius 5-15 mm) used to find corresponding points for each tract over the individuals in our dataset.

Stability (%)	L-ATR	R-ATR	L-CGC	R-CGC	L-CST	R-CST	L-IFO	R-IFO	L-ARC
5mm vs. 10mm	89	90	91	90	89	86	81	81	87
15mm vs. 10mm	93	94	96	94	87	87	90	87	91
	L-ILF	R-ILF	CC-FRN	CC-PRC	CC-POC	CC-PAR	CC-TEM	CC-OCC	
5mm vs. 10mm	77	84	90	80	84	78	61	83	
15mm vs. 10mm	87	93	93	82	88	81	66	92	

4.5 Conclusion

Here we presented an automatic fiber clustering workflow that uses anatomical information from multiple manually made atlases. The top-down approach helps to suppress effects of false positive streamlines by placing constraints on locations and shapes of tracts through their Hausdorff distance to warped hand-labeled atlases. The candidates from multiple atlases are combined with a fusion strategy. The clustering results are illustrated visually and quantitatively validated for a randomly selected sample data set. The clustering results from our method were more accurate than those from the ROI-only method. We also showed an example of how to perform a group statistical analysis (a heritability study) by using the sub-voxel fiber diffusion information mapped onto the clustered tracts. The complete workflow provides us with a practical tool for future large population studies that may reveal how the brain is affected by genetic factors, and by a variety of psychiatric or neurological disorders such as Alzheimer's disease (**Chapter 5**).

Chapter 5

Automated Multi-atlas Labeling of the Fornix and its Integrity in Alzheimer's Disease

5.1. Introduction

Alzheimer's disease (AD) is a progressive, degenerative disorder that attacks the brain's nerve cells, or neurons, resulting in loss of memory, thinking and language skills, and behavioral changes. An estimated 26.6 million people worldwide and 5.2 million Americans of all ages have AD in 2013. It is the 6th leading cause of death in the United States overall and the 5th for those aged 65 and over. Amyloid-beta plaques and tau protein tangles in the brain are hallmarks of the disease. Cerebrospinal fluid measures of pathology or amyloid plaque imaging (e.g. 11C-PIB PET) may be good diagnostic markers and may also predict future decline. However, there is an effort to define cheaper and less invasive biomarkers, using MRI and its variants to assess perfusion, activation or fiber integrity. More recently, diffusion tensor magnetic resonance imaging (DTI) (Basser *et al*., 1994) has become a popular method to reconstruct the local profile of water diffusion in tissues, yielding information on white matter (WM) integrity and connectivity that is not available from standard anatomical MRI. Region-of-interest (ROI)-based voxel analyses have been used to identify AD-related abnormalities in the fronto-occipital fasciculi, the inferior longitudinal fasciculi, the cingulum, and the *forceps major* based on DTI-derived parameters, such as fractional anisotropy (FA) and measures of mean, radial, or axial diffusivity (Teipel *et al*., 2007). DTI may provide useful information for clinical diagnosis of AD, and can help in detecting fiber tract and network breakdown not visible on standard MRI.

Among those WM fiber tracts, the fornix is critical for normal cognitive functioning. It is the major output tract of the hippocampus, arching around the thalamus and connecting the medial temporal lobes to the hypothalamus. Even though it is well known that the hippocampal atrophy is associated with AD (Morra *et al*., 2008) and the fornix is the main white matter pathway to and from the hippocampus, the fornix is less well-studied as a predictor of cognitive impairment as AD progresses. This is mainly because the fornix is very hard to segment due to its small volume relative to the typical voxel size of MRI or DTI. Even so, because AD typically begins in the hippocampus and medial temporal lobes, it makes sense to evaluate the tracts innervating this crucial region, which is involved in both learning and memory. Prior studies either manually delineated ROIs for the fornix (Oishi *et al*., 2012) or automatically deformed a template onto each subject in a population (Fletcher *et al*., 2013). The 1-D mean FA of the main fornix body or the 2-D crest line of locally maximal FA intensities across voxels have been used in statistical analyses, such as tract-based spatial statistics, usually in small cohorts of subjects.

To overcome these limitations, here we take a different approach to automatically segment the fornix from 3-D whole-brain tractography. Based on the fornix ROI from a publicly available WM atlas (Oish *et al*., 2009), we first manually constructed five fornix atlases as prior anatomical information. Then, we transfered the tract label to new subjects by selecting only fibers that are similar to the corresponding fornix atlases, based on a similarity measure. Multiple atlases help to adapt to the variability of tract shapes in new subjects. Next, we used a label fusion scheme to fuse the clustered results obtained from individual atlases. Many fiber clustering methods have been proposed, but it is not always clear how to apply them to large-scale group studies, where voxel-based or ROI studies are still popular. Once we segmented the

fornix for each subject, in order to facilitate large-scale statistical analysis, we implemented a novel point-wise matching scheme to match fiber points across the population. To test the robustness of our algorithm, we applied it to a population study of a large cohort, of 210 participants. We studied the complete 3-D sub-voxel profile of the fornix in the population, at sub-voxel resolution. Our goal was to compare a variety of DTI-derived measures across among different groups in the cohort to demonstrate the utility of the algorithm for clinical research, and to define tract-based measures that are sensitive to disease progression.

5.2. Subjects and Data Acquisition

The diffusion weighted imaging (DWI) data of our subjects were downloaded from the Alzheimer's Disease Neuroimaging Initiative (ADNI) database (http://adni.loni.usc.edu). We performed an analysis of baseline DWI data from 210 participants (Age: 55-90; mean: 72.2+/-7.4 SD; 124 males / 96 females). 52 of them were normal elderly people, 113 had mild cognitive impairment (MCI) who were at an increased risk of progressing to AD, and 45 were AD patients. Each subject underwent cognitive evaluations and was given the Mini-Mental State Examination (MMSE) and the Clinical Dementia Rating - Sum of Boxes (CDR-SOB) tests.

DWI scans were acquired with 3-Tesla GE Medical Systems scanners at 14 sites across North America. Each 3-D volume consisted of 59 axial slices with isotropic voxel size 2.7 mm with 256 x 256 acquisition matrix. 46 image volumes were acquired per subject: 5 with T2-weighted b_0 images and 41 diffusion-weighted volumes (b = 1000 s/mm^2).

5.3. Probabilistic Tractography

Raw DWI data were corrected for eddy-current induced distortions with FSL (http://www.fmrib.ox.ac.uk/fsl/). We performed whole-brain tractography with Camino (http://cmic.cs.ucl.ac.uk/camino/). The diffusion tensor was fit to the data. We used the Probabilistic Index of Connectivity method (PICo) (Parker *et al*., 2003*b*) to generate probabilistic tractography. Seed points were chosen at those voxels whose FA values were greater than 0.3. Monte Carlo simulation was used to generate fibers proceeding from the seed points throughout the entire brain with 4th-order Runge-Kutta interpolation. The maximum fiber turning angle was set to 40°/voxel, and tracing stopped at any voxel whose FA was less than 0.2.

5.4. Fornix Atlas Construction

We manually constructed five fornix atlases from the healthy twins' data set as in **Section 4.2**. A single-subject template in the ICBM-152 space called the "Type II Eve Atlas" (a 32-year old healthy female) (Oishi *et al*., 2009) was registered to the FA images of each atlas with Advanced Normalization Tools (ANTs) (http://picsl.upenn.edu/software/ants/). The "Eve" fornix ROI was re-assigned to the five atlases with the resulting deformation fields by ANTs. Fibers that traversed the ROI were extracted and manually edited to form our fornix atlases. We opted to use data from healthy adults (twins) instead of elderly individuals from ADNI because their fornix tracts are intact and can be more completely extracted. The templates are also more likely to be reusable for different types of data sets, including data from younger adults.

5.5. Fiber Clustering

For each subject in our data set, the same registration registered the subject's FA image to each of the five fornix atlases' FA images and the "Eve" FA image, respectively. Each fornix atlas and the Eve's fornix ROI were then warped to the subject space with the corresponding deformation fields. Fiber alignment is known to be improved significantly with that type of registration (**Chapter 2** or Jin *et al*., 2011*a*).

We first chose the fibers that traversed the warped Eve fornix ROI. This quickly reduced the number of fibers from millions to only a few hundreds. To further refine the result, we defined a fiber distance metric to select the fibers whose distances were close to one of the warped atlas fibers, based on a validated empirical threshold (15 mm) in **Section 3.6.2**. For any pair of fibers γ_i and γ_j, the symmetric Hausdorff distance is defined in **Section 3.4.3** (Equation (3.2) and Equation (3.3)). The Hausdorff distance is conservative and keeps only the fibers whose shapes and locations are similar to the atlases. This is intended to facilitate large population studies.

5.6. Label Fusion

Due to the variability of individual atlases, different atlases may nominate different candidates. We implemented a label fusion scheme to combine the results from individual atlases. A mean fiber distance was defined to rank the fibers nominated by individual atlases: $d_{mean} = \frac{\sum_{d_i<d_{cutoff}} d_i + \sum_{d_i>d_{cutoff}} d_{sup}}{n}$, where d_i is the Hausdorff distance between an unlabeled subject's fiber and the i-th atlas, d_{cutoff} is the empirical cutoff threshold chosen in **Section 5.5**, d_{sup} is the upper bound Hausdorff distance within which a subject fiber can be possibly considered a candidate for a given tract, and n is the number of atlases. We ranked all the candidate fibers from different atlases based on their d_{mean}'s. The smaller its d_{mean}, the higher its rank. A fusion percentage was defined to include fibers whose d_{mean}'s were among the top specified percentage. Here we set the fusion percentage to be 95% because no other confounding fibers are adjacent to the fornix and the number of false positive fibers is relatively low.

5.7. Fiber Matching

To perform group studies, we need to establish the correspondence between fibers of the segmented fornix tracts across the population. First, we chose a representative sample fornix tract from our ADNI population. Each point on that representative tract was mapped to the rest of the population. The point on each fornix tract in the population with the closest Euclidean distance to that sample point was considered the corresponding point. More specifically, the point on the representative tract (the representative point) was warped to each subject's space. It was then projected onto the fibers that intersect with the neighborhood of the representative

point. The projection point with the shortest distance to the representative point was taken as the corresponding point for that subject. If there were no fibers crossing the neighborhood (a sphere with the 10 mm radius), the warped representative point location is used as the correspondence point. **Figure 5-1** illustrates our fiber matching method.

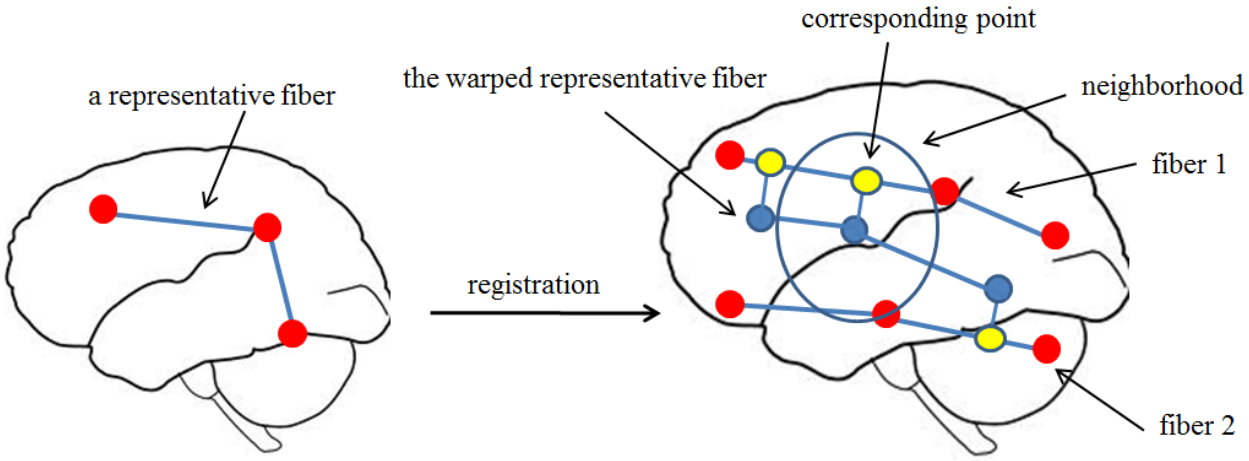

Figure 5-1. An illustration of fiber matching scheme.

5.8. Statistical Analysis

Statistical analysis was performed comparing groups with a variety of metrics based on the extracted tracts, such as the number of detected fibers, the mean FA or the mean diffusivity (MD) of the volume that those fibers cross, and the 3-D FA/MD profile, to demonstrate the utility of the technique.

5.9. Results

5.9.1. Fiber Count

Figure 5-2 shows a box plot of the number of detected fibers for the four groups. The five horizontal lines in each group represent the minimum, lower quartile, median, upper quartile, and the maximum. Outliers are marked with a +. Notches offer a rough guide to significance of the difference in medians. As hypothesized, the median of each group decreases from the normal to the MCIs and to the AD group. The group-wise Cohen's *d*'s (effect sizes) and p-values of the *t*-tests show that the group differences are all significant.

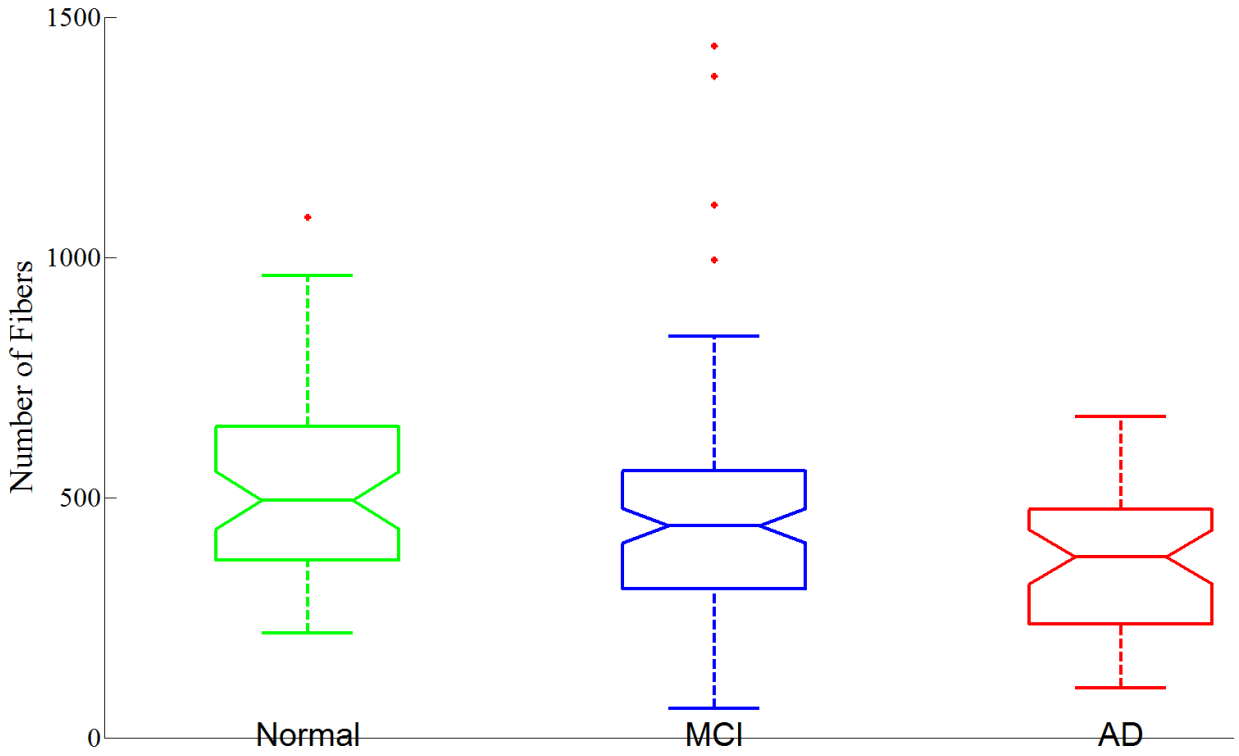

Number of Fibers (Cohen's *d*/*p*-value)	Normal	MCI	AD
Normal	n/a	n/a	n/a
MCI	0.35/0.04	n/a	n/a
AD	0.87/$6x10^{-5}$	0.41/0.04	n/a

Figure 5-2. A box plot shows the number of fibers detected in the fornix for normal controls (in *green*), MCI patients (in *blue*), and AD patients (in *red*). The group-wise Cohen's *d*'s and *p*-values of the *t*-tests are listed.

5.9.2. Mean FA and MD

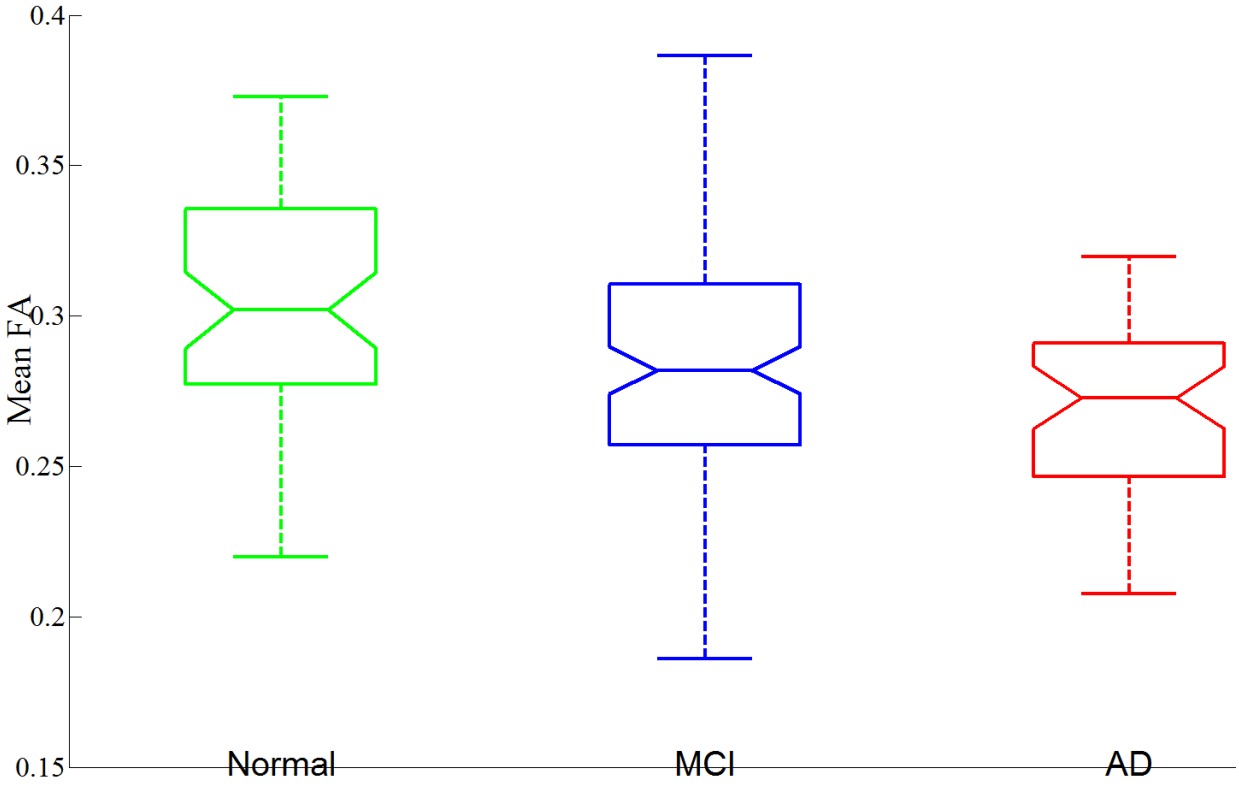

Mean FA (Cohen's *d*/*p*-value)	Normal	MCI	AD
Normal	n/a	n/a	n/a
MCI	0.56/0.001	n/a	n/a
AD	1.10/$5x10^{-7}$	0.48/0.01	n/a

Figure 5-3. A box plot shows the mean FA values of the fornix for normal controls (in *green*), MCI patients (in *blue*), and AD patients (in *red*). The group-wise Cohen's *d*'s and *p*-values of the *t*-tests are listed.

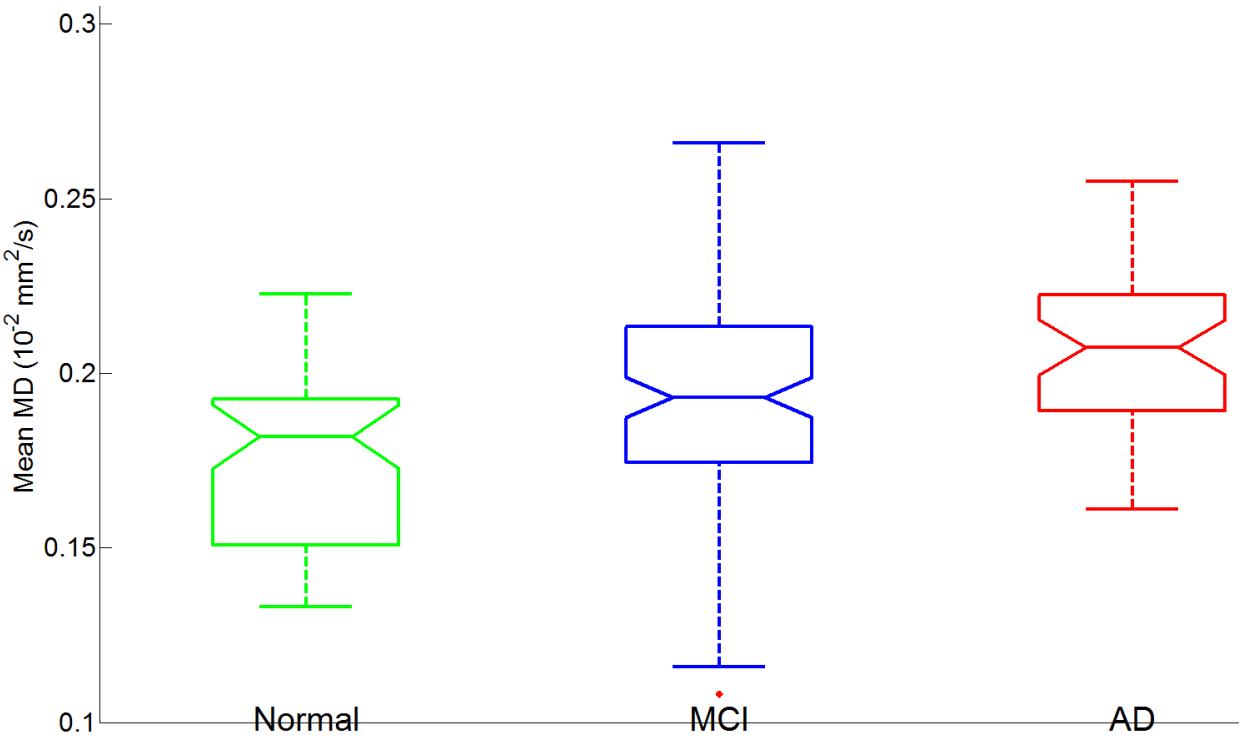

Mean MD (Cohen's *d*/*p*-value)	Normal	MCI	AD
Normal	n/a	n/a	n/a
MCI	0.57/0.001	n/a	n/a
AD	1.25/0	0.54/0.0042	n/a

Figure 5-4. A box plot shows the mean MD values of the fornix for normal controls (in *green*), MCI patients (in *blue*), and AD patients (in *red*). The associated group-wise Cohen's *d*'s and *p*-values of the *t*-tests are listed.

Figure 5-3 and **5-4** show box plots of the mean FA and MD values of the entire fornix for the three diagnostic groups and the Cohen's *d*'s and the *p*-values of the t-tests comparing groups.

Clearly, these tests could be covariated for age and sex, but the intent here is simply to show that statistical modeling is feasible and detects group differences. The mean FA or MD value for each subject was calculated by averaging the FA or MD values of all the voxels the labeled fornix tract traversed and the voxels which the corresponding fiber points were in (in case tractography was poor in some subjects). We used 10^{-2} mm^2/s as the unit for MD to make its values comparable to the range of FA values (which are dimensionless). The median of mean FA also decreases in the same trend as **Figure 5-2**, while the median of mean MD increases as expected. The diffusivity increase may be because myelin breaks down in AD and offers less hindrance to water diffusion. The mean MD difference is more marked than that of FA between groups in terms of both effect size (Cohen's *d*) and the associated *p*-values.

5.9.3. 3-D FA and MD Profiles

Figure 5-5 shows the three individual representative fornix tracts for the three groups and the 3-D sub-voxel profiles (a point-wise *t*-test between different diagnostic groups) of the differences in FA and MD values between the normal group and the AD group, respectively. Results are corrected for multiple comparisons. Again, MD is more sensitive in detecting the changes between the two groups, at least in this sample.

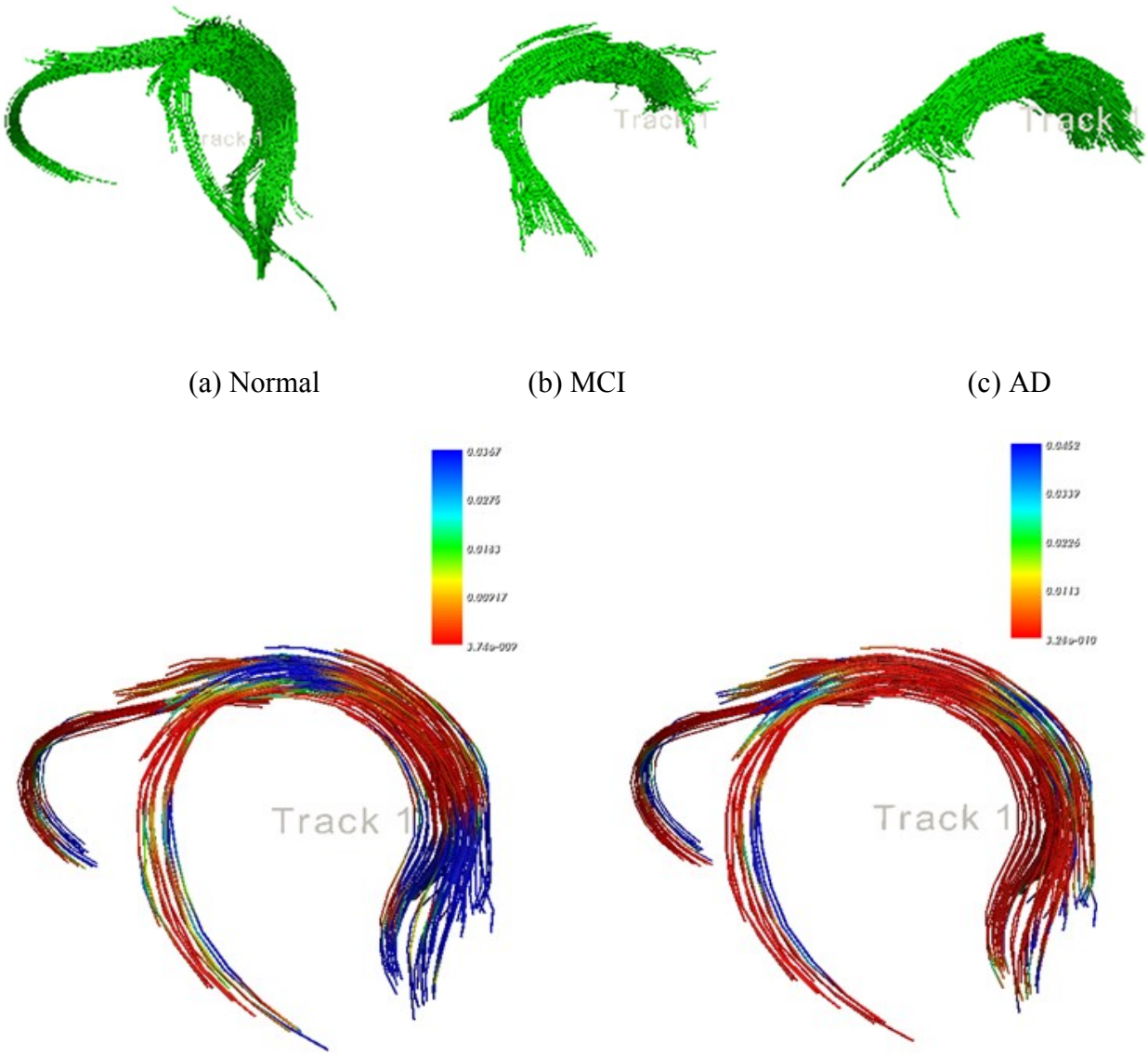

(a) Normal (b) MCI (c) AD

(d) Normal vs. AD (FA) (e) Normal vs. AD (MD)

Figure 5-5. A representative fornix tract is shown for each group and 3-D color maps reveal differences in FA and MD values between normal elderly and AD groups, respectively. Redder colors show greater group differences in FA or MD values at those points.

5.9.4. Correlations with Clinical Scores

We performed a linear regression analysis on the MMSE and CDR-SOB scores for each subject versus the mean FA and MD values of their fornix tracts, adjusting for age and sex. The statistics are shown in **Table 5-1**. The mean FA/MD of the fornix explains about 10%/12% (R^2) of the variance in MMSE scores and 10%/11% in CDR-SOB, respectively. The relationships between clinical scores and mean FA/MD are both statistically significant.

Table 5-1. Regression statistics relating MMSE and CDR-SOB scores (measures of clinical decline) to mean FA and MD of the fornix, after adjusting for age and sex.

Clinical Score	Variable	R^2	*p*-value	Variable	R^2	*p*-value
	mean FA		**1.8×10^{-3}**	mean MD		**1.5×10^{-4}**
MMSE	age	0.10	**0.02**	age	0.12	0.10
	sex		0.69	sex		0.56
	mean FA		**2×10^{-5}**	mean MD		**7.7×10^{-6}**
CDR-SOB	age	0.10	0.59	age	0.11	0.97
	sex		0.84	sex		0.76

5.9.5. ROC Curve

We used the mean MD as features to classify the normal and the AD groups. The receiver operating characteristic (ROC) curve is plotted in **Figure 5-6**. The cutoff MD value is 0.0019 mm^2/s with 71% sensitivity and 71% specificity. The area under the curve (AUC) is 0.78 (AUC > 0.75 is clinically useful). This is a new diffusion feature we may be able to use to combine

with those classical anatomical features to improve the accuracy of classifying different stages of Alzheimer's disease.

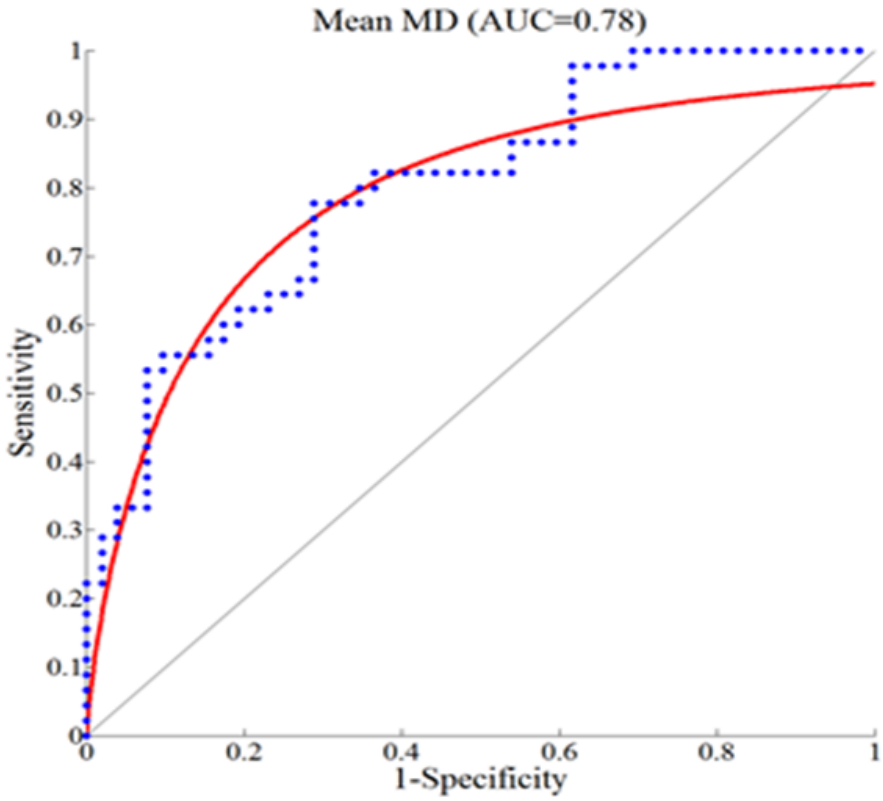

Figure 5-6. The ROC curve is shown for the mean MD for classifying AD patients versus the normal group.

5.10. Discussion and Conclusion

Here we presented an automatic tract labeling technique that uses anatomical information from multiple manual atlases. We implemented it to segment the fornix in 210 subjects. We then proposed a point-wise fiber matching scheme to illustrate how to establish tract correspondence in a population and perform large-scale group studies.

We studied the fornix in detail by comparing how Alzheimer's disease affects different DTI-derived measures as AD progresses. Our results are consistent with prior findings that fornix degeneration is associated with cognitive decline (Oishi *et al*., 2012; Fletcher *et al*., 2013) and MD seems to be a better measure for detecting AD-related differences than FA (Nir *et al*., 2013).

The contribution of our work is to present a reliable general workflow for large population studies and provide extra information (such as 3-D sub-voxel profiles) for tract analysis. It will be extended to group studies of various neurological and psychiatric conditions, as well as for research in imaging genetics.

Chapter 6

Voxelwise Spectral Diffusional Connectivity

6.1 Introduction

The human brain is a complex network of structurally connected regions that interact functionally. Brain connectivity can be studied from different perspectives. Functional MRI, can reveal correlated activity and even causal relationships that underlie the communication of distributed brain systems. On the other hand, diffusion weighted MRI (DWI) measures the local profile of water diffusion in tissues, yielding information on white matter (WM) integrity and connectivity that traditional structural MRI cannot provide. DWI is non-invasive, and is increasingly used to study macro-scale anatomical connections linking brain regions through fiber pathways.

Brain networks are commonly described as a mathematical graph, consisting of a collection of nodes, representing a parcellation of the brain regions of interest (ROIs), and a set of edges between pairs of nodes, describing some property of the connection between that pair of regions. The brain exhibits several organization principles, including “small-worldness”, characterized by the coexistence of dense local clustering between neighboring nodes and high global efficiency (short average path length) due to few long-range connections (Bassett and Bullmore, 2006). This property results in a sparse connectivity matrix that can be explored using graph theory. A typical way to construct the connectivity matrix is to group adjacent voxels into ROIs (anatomically meaningful gray matter regions) or nodes, and count the fibers passing through

each pair of nodes. Then standard measures of connectivity including small worldness, clustering, path length, and efficiency can be computed to reveal how the brain is affected by genetic factors (Jahanshad *et al*., 2012*b*) and neurological diseases such as Alzheimer's disease (Daianu *et al*., 2012).

However, this classical approach has limitations. First, there is lack of validation of WM fibers generated by tractography. Based on different reconstruction or tracking models (tensor vs. orientation distribution function and deterministic vs. probabilistic), different tractography algorithms and variations in their parameters can lead to large differences in the resulting network measures (Bastiani *et al*., 2012). Automatic cortical gray matter segmentation from an atlas is also susceptible to registration error. Furthermore, the spatial scale of the parcellation of the gray matter into nodes of the connectivity graph may affect connectivity measures by as much as 95% (Zalesky *et al*., 2010). Finally, parameter thresholding in graph analysis also influences the interpretation of the results (Dennis *et al*., 2012).

To avoid these problems, we propose a novel mathematical formulation to explore brain connectivity from a different perspective. Instead of investigating linkages among sub-regions of the brain, we use the tensor information from DWI at the voxel level. In this way, we avoid making further assumptions on tractography that diffusion images do not intrinsically provide. Then we show that the diffusion equation can be characterized by the Laplacian matrix of the tensor field. In graph theory, the Laplacian matrix is a matrix representation of a graph. It can be used to calculate the number of spanning trees for a given graph. We, therefore, circumvent the

nodal parcellation problem by studying voxelwise linkage. Although others have studied voxel connectivity in its local neighborhood (Zalesky and Fornito, 2009), our work focuses more on studying the brain as a whole entity. Finally, we present two important characteristics of a graph, the number of spanning trees (Kirchhoff complexity) and the eigen-spectrum, both of which can be computed without any parameter tuning. As there may be well over a million voxels in a typical image volume, the Kirchhoff complexity and eigen-spectrum can be challenging to compute. We therefore present an algorithm to calculate them efficiently. In the Experimental Section, we illustrate how to evaluate these measures in two biomedical applications (Alzheimer's disease and intelligence prediction).

6.2 Voxelwise Spectral Diffusional Connectivity

6.2.1 Diffusion Equation and Tensor

DWI yields information on WM fibers by measuring signals sensitive to the directional diffusion of water molecules. A diffusion process is usually described by the diffusion equation, which is a partial differential equation as follows

$$\frac{\partial f(x,t)}{\partial t} = < \nabla, T(x)\nabla f(x,t) > \tag{6.1}$$

where $f(x,t)$ is the density of the diffusing material at time t and at location x (in the continuous domain), $T(x)$ is the diffusion tensor at location x, and ∇ represents the spatial derivative operator. Here $-T(x)\nabla f(x,t)$ can be understood as the "flux", the amount of diffusing material moving through a unit surface at location x, and over a unit time interval starting at time t.

$T(x)$ fully characterizes the diffusion properties of a field. The diffusion tensor images reconstructed from DWI are voxel estimates of the diffusion field $T(x)$. To make $T(x)$ reflect the spatial density of WM fibers, we modulate diffusion tensors with its fractional anisotropy (FA).

6.2.2. Laplacian Matrix and Graph

To study $T(x)$ numerically, the spatially and temporally continuous process defined by Equation (6.1) should be discretized. As we are interested in T(x) itself, not the diffusion process $f(x,t)$, we discretize it only spatially with the finite difference method. Then the discretized version of Equation (6.1) becomes $\frac{\partial f(x,t)}{\partial t} = -Af$, where A is a square matrix of size n, where n is the number of voxels of interest. A should satisfy the following criteria: (1) It is self-adjoint because the diffusivity between two voxels should be independent of the direction of the flux that crosses them. (2) The sum of each row or each column needs to be zero because the total volume of the diffusion material should be preserved. (3) Its off-diagonal elements are non-positive because the molecules diffuse from high concentration to low concentration. Matrices that satisfy all the three properties are called Laplacian matrices.

Laplacian matrices and graphs have a one-to-one mapping relationship. Given the adjacency matrix of an undirected and weighted graph G whose elements $\{g_{ij}\}$ indicate the edge weight between two adjacent vertices i and j, its Laplacian matrix $A = \{a_{ij}\}$ is defined as

$$a_{ij} = \begin{cases} -g_{ij}, if\ i \neq j, \\ \sum_{k=1}^{n} g_{ik}, if\ i = j. \end{cases} \tag{6.2}$$

We can see that how the Laplacian matrix is constructed also implies that a graph can be inversely constructed from its Laplacian matrix. It is worth noting that the Laplacian matrix A of a connected graph is positive semi-definite. There is one and only one zero eigenvalue and the rest of the eigenvalues are all positive.

With this one-to-one correspondence relationship, we claim that a diffusion field can be studied via its Laplacian matrix or its corresponding graph. For example, we can study its connectivity complexity, as addressed in **Section 6.2.3**, its eigen-spectrum, as addressed in **Section 6.2.4**, or its vertex centrality in future work.

6.2.3. Spanning Trees and Kirchhoff Complexity

A spanning tree of a connected graph G is a sub-graph connecting all the vertices in G, which does not contain any circular path. Adding one edge to a spanning tree creates a circle and deleting one edge from a spanning tree partitions the tree into two disjoint sets. Spanning trees play important roles in graph theory. It is also related to fundamental circles and fundamental cut sets of a graph. One measurement of the complexity of a graph is the number of its spanning trees, which is called the Kirchhoff complexity (Tutte, 2001). The extended Kirchhoff complexity for weighted graphs is defined as

$$K(G) = \sum_{\pi \in T(G)} \omega(\pi), \omega(\pi) = \prod_{i,j \in \pi} g_{ij} \tag{6.3}$$

where $T(G)$ is the set of spanning trees of an undirected weighted graph $G = \{g_{ij}\}$, π is a spanning tree, and $\omega(\pi)$ is the weight associated with π by multiplying all the weights of its edges.

We choose $K(G)$ to indicate the complexity of a connectivity network because it enumerates all the possible ways to connect all the vertices in a graph without circles and it also considers the effectiveness of the connection by weighting with its edge weights.

Although $K(G)$ is defined by enumeration, its calculation does not require enumeration. It can be solved with the Kirchhoff Matrix-Tree theorem (Chaiken, 1982) as follows.

Kirchhoff's Matrix-Tree Theorem: Given a connected undirected weighted graph G, its Kirchhoff complexity is

$$K(G) = \frac{1}{n}\lambda_1\lambda_2 \cdots \lambda_{n-1} = \det(A_{-i}) \tag{6.4}$$

where $\lambda_1, \lambda_2, \cdots, \lambda_{n-1}$ are the non-zero eigenvalues of the Laplacian matrix of G, A_{-i} is the matrix derived by removing the ith row and the ith column from the Laplacian matrix, and n is the number of vertices of G. Interestingly, no matter what value i takes, the result is the same.

Equation (6.4) requires the calculation of the matrix determinant, but direct and exact calculation of the determinant of large matrices is not currently feasible, as it may lead to numerical overflow. Fortunately, we can calculate the logarithm of the determinant very

efficiently with matrix factorization. Given a symmetric A_{-i}, we first decompose it as $A_{-i} = LDL^T$ by the LDL decomposition where L is a square lower uni-triangular matrix and D is a diagonal matrix with rank $n-1$. Now we have two properties:

(1) $\det(A_{-i}) = \det(L)\det(D)\det(L^T) = \det(D)$

(2) $\det(D) = \prod_{i=1}^{n-1} d_{ii}$

where d_{ii} is the ith diagonal element of D. Then we can calculate the logarithm of Kirchhoff complexity as

$$lnK = \ln\det(A_{-i}) = \sum_{i=1}^{n-1} lnd_{ii} \tag{6.5}$$

6.2.4. Estimation of Eigenvalue Spectrum

The eigenvalues of a Laplacian matrix A not only decide the complexity of a graph (see Equation (6.4)) but also convey important information on the temporal responses of the differential equation $\frac{\partial f(x,t)}{\partial t} = -Af$. However, calculating the eigenvalues of a large sparse matrix demands cumbersome computation and can be impractical. For example, at the 128 x 128 x 128 image volume size, the Laplacian matrix derived from the diffusion tensor images has approximately 2 x 10^6 rows and columns. For such a large matrix, direct and exact calculation of their eigenvalues is practically impossible. As we are only interested in the distribution of the eigenvalues instead of their exact values, we can estimate the cumulative distribution function (CDF) of the eigenvalues with Sylvester's Law of Inertia.

Sylvester's Law of Inertia: Given a symmetric and real-valued matrix A, its transformation $B = SAS^T$ where S is an invertible square matrix, has the same number of positive/negative eigenvalues as A does.

Let $h(\beta)$ be the number of A's eigenvalues which are equal or smaller than β, that is, $h(\beta) = |\{\lambda_i \leq \beta\}|$ where λ_i's are the eigenvalues of A. To calculate $h(\beta)$, we first factorize $A_\beta = A - \beta I$ as $A_\beta = LDL^T$ by the LDL decomposition, where I is the identity matrix, and L and D are denoted as in **Section 6.2.3**. Now we have three properties: (1) if λ is an eigenvalue of A, then $\lambda - \beta$ is an eigenvalue of A_β; (2) D has the same number of positive/negative eigenvalues as A_β does; (3) The eigenvalues of D are its diagonal elements. These properties implies that $h(\beta)$ equals the number of the diagonal elements of D which are less than or equal to 0, even though the diagonal elements of D are not necessarily the eigenvalues of A_β. The detailed eigen-spectrum computation algorithm is summarized in **Algorithm 1**.

Algorithm 1 Estimation of Eigen-Spectrum with m Bins

1. Calculate the largest eigenvalue λ_{max} of A with the power iteration method.
2. Set bin positions $\{\beta_i = \frac{i}{m}\lambda_{max}, i = 1, \dots, m\}$ for estimating $h(\beta_i)$.
3. For each β_i:
   (a) Decompose $A - \beta_i I$ as LDL^T.
   (b) $h(\beta_i) = |\{d_{kk} \leq 0\}|$ where d_{kk}'s are diagonal elements of D.

6.3 Experiments

In this section, we show how to apply the theory we derived in **Section 6.2** to two real biomedical problems.

6.3.1. Graph Construction and Connectivity Computation

The raw diffusion images were corrected for eddy-current induced distortions with FMRIB Software Library (FSL) and then skull-stripped using the FSL tool, BET. The FA modulated tensor field was reconstructed using our own C++ diffusion tool package developed with Segmentation & Registration Toolkit (ITK). Negative eigenvalues of the reconstructed tensors were rectified to their absolute values. Next, the FA image of each subject was linearly aligned to a single-subject FA atlas ("Eve" atlas) from Johns Hopkins University (Oishi *et al*., 2009) (the atlas was downsampled to the 2 x 2 x 2 mm^3 resolution to facilitate the computation). The purpose of registration was to reduce the possible bias in graph construction introduced by individual volumetric differences. Tensors were linearly interpolated and re-oriented with the preservation-of-principal-direction method (Alexander *et al*., 2001) when the affine transformation was applied. The discretized Laplacian matrix of the transformed tensor field was constructed. Finally, the logarithm of Kirchhoff complexity was computed as described in **Section 6.2.3** and the logarithmic eigen-spectrum was estimated according to **Algorithm 1** in **Section 6.2.4**. The Laplacian matrices were sparse and it took about 5 minutes to perform one LDL routine for a square matrix of size $2x10^6$ with a 2.8 GHz Xeon CPU.

6.3.2. Alzheimer's Disease

AD is an irreversible, progressive brain disease that destroys memory and cognition, and is the most common cause of dementia in older people. All of our subjects were recruited as part of phase 2 of the Alzheimer's Disease Neuroimaging Initiative (ADNI2) - an ongoing, longitudinal, multi-center study designed to find biomarkers for the early detection of AD. 155 subjects were categorized into four groups: normal (sex/average age: 22 male (M)/22 female (F)/72.7 years), early mild cognitive impairment (eMCI) (38M/24F/74.0), late mild cognitive impairment (lMCI) (15M/11F/73.0), and AD (15M/8F/75.8). MCI is an intermediate stage between normal aging and AD. 46 DWI volumes were acquired per subject: 5 T2-weighted b_0 image volumes and 41 diffusion-weighted volumes (b = 1000 s/mm^2). Each volume dimension was 256 x 256 x 59 and the voxel size was 1.37 x 1.37 x 2.7 mm^3.

Figure 6-1(a) shows a box plot of the logarithm of Kirchhoff complexity of the four groups. The minimum and the maximum of each group are displayed in black, the lower quartile and the upper quartile in blue, and the median in red. All outliers are marked with "+". The median logarithm of Kirchhoff complexity decreases from the normal group to both MCI groups and to the AD group. In **Figure 6-1(b)**, we show ten normalized logarithmic eigen-spectra of the AD group and the normal controls (5 people from each group were randomly selected). The peaks of the spectra are shifted towards the right in the AD patients, relative to the normal controls. After excluding outliers indicated by the box plot, we also performed a t-test on the logarithm of Kirchhoff complexity between each pair of groups, and the t-statistic between AD and normal group was -3.24 (p=0.0019). The trend of decreasing global structural network connectivity from

the normal group to the AD group is consistent with similar findings in functional (Supekar *et al*., 2008) and anatomical connectivity studies (Daianu *et al*., 2012).

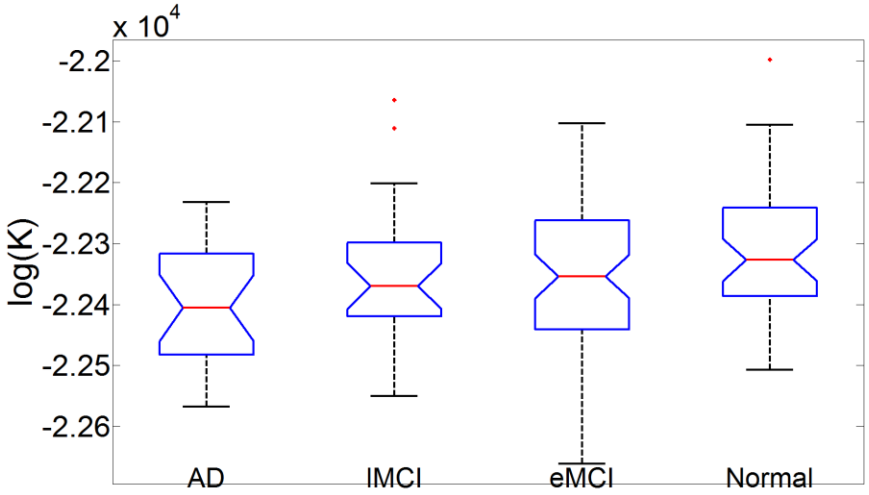

(a)

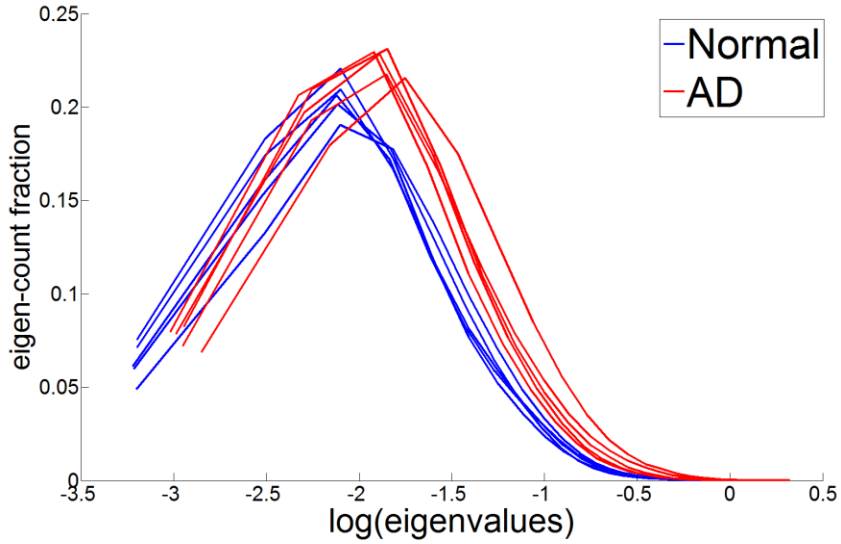

(b)

Figure 6-1. The figure (a) shows the box plot of the logarithm of Kirchhoff complexity of the four groups and (b) illustrates 5 representative normalized logarithmic eigen-spectra for AD patients (in *red*) and normal controls (in *blue*), respectively.

6.3.3. Intelligence

80 pediatric subjects were included in this study, from 7 to 17 years old with an average age of 12.2 years. 30-direction DWI data was collected (b = 1000 s/mm^2). The voxel dimension was 128 x 128 x 128, with an isotropic voxel size of 2 mm.

Regression analysis was applied to study the correlation between the subjects' performance intelligence quotient (PIQ) and the logarithm of Kirchhoff complexity, in conjunction with their age variability. The response variable was PIQ, and the regressors were the logarithm of Kirchhoff complexity and age. Scatter plots relating the variables are shown in **Figure 6-2**. Both one-factor and two-factor regressions were performed. Statistics from the regression analysis are listed in **Table 6-1**. PIQ and the logarithm of Kirchhoff complexity show statistically significant correlation (r^2=0.066 or 6.6%) at the 5% significance level. Our result is consistent with Cole *et al*.'s study (2012) with functional MRI in which measures of global brain connectivity were found to explain about 5% of the normal variance in intellectual function.

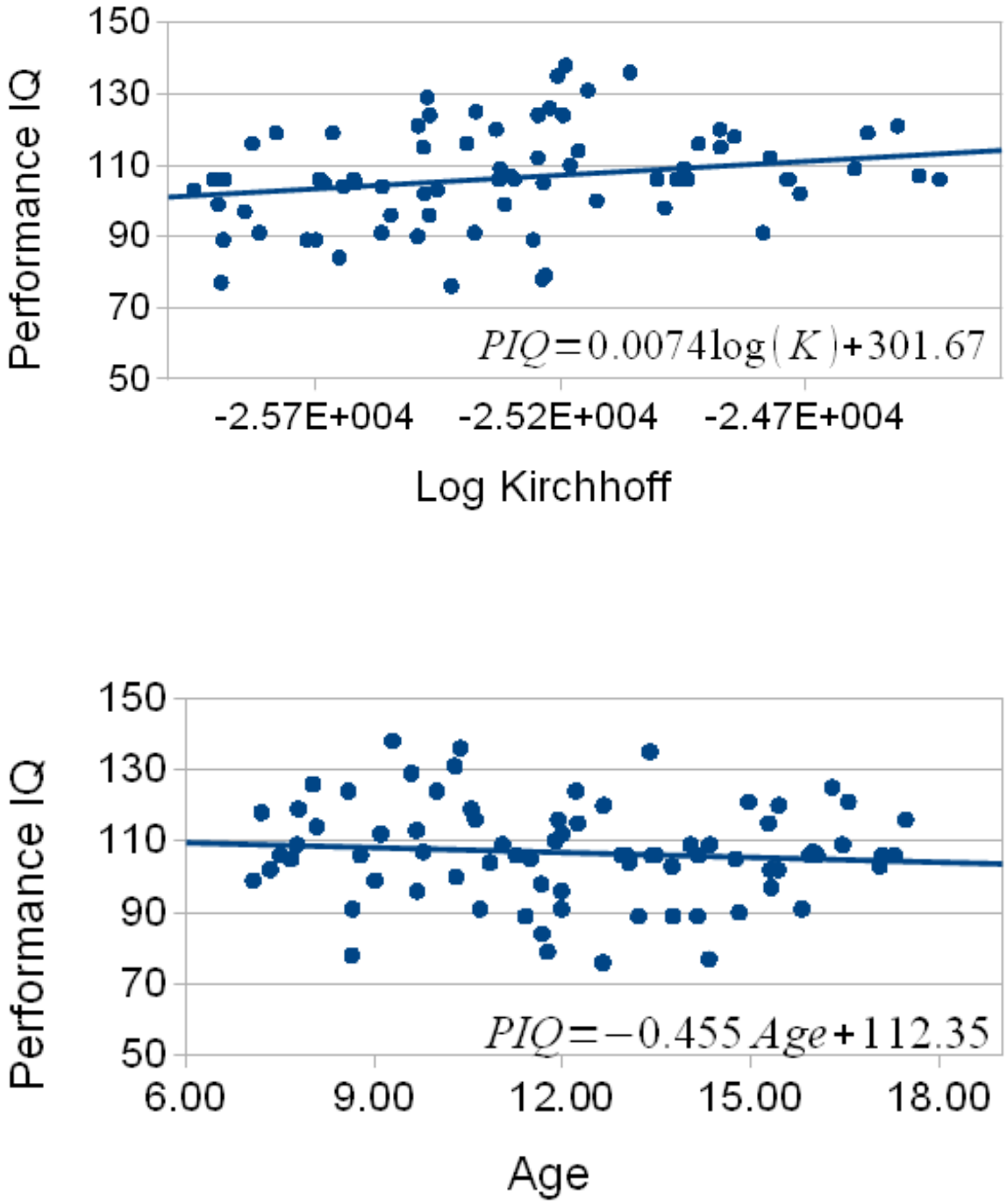

Figure 6-2. Scatter plots and regression equations of PIQ against the logarithm of Kirchhoff complexity and age, respectively.

Table 6-1. Regression statistics. The logarithm of Kirchhoff complexity is statistically significant as a predictor of PIQ in both one-factor and two-factor linear regression models.

Regression Model	Variable	Coefficient (95% CI)	r^2	t-statistic	p-value
One-factor	ln(K)	$7.41 \pm 6.43 \times 10^{-3}$	0.066	2.30	**0.025**
	Age	-0.46 ± 1.08	0.009	-0.84	0.40
Two-factor	ln(K)	$7.41 \pm 6.48 \times 10^{-3}$	0.071	2.22	**0.029**
	Age	-0.36 ± 1.06		-0.68	0.50

6.4. Conclusion and Future Work

Here we presented a new method to study overall brain connectivity at the voxel level instead of defining ROI-based nodes and using fiber guidance from tractography. Laplacian matrix of the diffusion tensor field has been proven to have a one-to-one correspondence with its connectivity graph. The voxelwise matrix is high dimensional - making a brute force solution impossible with normal laboratory computing resources. Instead, our measures, the Kirchhoff complexity and eigen-spectrum, can be computed efficiently without an unreasonable computational burden. We illustrate how to apply our measures to biological and medical questions. In our experiments, our estimates have a reasonable interpretation as indices of brain connectivity for disease characterization and intelligence prediction. Future work on voxelwise diffusion connectivity shows promise. For example, we can study the betweenness centrality of a vertex (voxel) and determine the relative importance of a voxel within the network. Or we can perform eigen-embedding to project voxels to higher-dimensional space and invent a new way to define ROIs.

BIBLIOGRAPHY

Aganj, I., Lenglet, C., Jahanshad, N., Yacoub, E., Harel, N., Thompson, P.M., Sapiro, G., 2011. A Hough transform global probabilistic approach to multiple-subject diffusion MRI tractography. Medical Image Analysis 15(4), 414-425.

Alexander, D.C., Pierpaoli, C., Basser, P.J., Gee, J.C., 2001. Spatial transformations of diffusion tensor magnetic resonance images. IEEE Transactions on Medical Imaging 20(11), 1131-1139.

Avants, B.B., Epstein, C.L., Grossman, M., Gee, J.C., 2008. Symmetric diffeomorphic image registration with cross-correlation: evaluating automated labeling of elderly and neurodegenerative brain. Medical Image Analysis 12(1), 26-41.

Benjamini, Y. and Hochberg, Y., 1995. Controlling the false discovery rate: a practical and powerful approach to multiple testing. Journal of the Royal Statistical Society, Series B (Methodological) 57(1), 289-300.

Basser, P.J., Mattiello, J., LeBihan, D., 1994. MR diffusion tensor spectroscopy and imaging. Biophysical Journal 66(1), 259-267.

Basser, P.J., Pajevic, S., Pierpaoli, C., Duda, J., Aldroubi, A., 2000. In vivo fiber tractography using DT-MRI data. Magnetic Resonance in Medicine 44(4), 625-632.

Bassett, D.S. and Bullmore, E., 2006. Small-world brain networks. Neuroscientist 12(6), 512-523.

Bastiani, M., Shan, N.J., Goebel, R., Roebroeck, A., 2012. Human cortical connectome reconstruction from diffusion weighted MRI: the effect of tractography algorithm. NeuroImage 62(3), 1732-1749.

Behrens, T.E.J., Woolrich, M.W., Jenkinson, M., Johansen-Berg, H., Nunes, R.G., Clare, S., Matthews, P.M., Brady, J.M, Smith, S.M., 2003. Characterization and propagation of uncertainty in diffusion-weighted MR imaging. Magnetic Resonance in Medicine 50(5), 1077-1088.

Braskie, M.N., Jahanshad, N., Stein, J.L., Barysheva, M., McMahon, K.L., de Zubicaray, G.I., Martin, N.G., Wright, M.J., Ringman, J.M., Toga, A.W., Thompson, P.M., 2011. Common Alzheimer's disease risk variant within the CLU gene affects white matter microstructure in young adults. The Journal of Neuroscience 31(18), 6764-6770.

Bodini, B., Khaleeli, Z., Cercignani, M., Miller, D.H., Thompson, A.J., Ciccarelli, O., 2009. Exploring the relationship between white matter and gray matter damage in early primary progressive multiple sclerosis: an in vivo study with TBSS and VBM. Human Brain Mapping 30(9), 2852-2861.

Brouwer, R.M., Mandl, R.C.W., Peper, J.S., van Baal, G.C.M., Kahn, R.S., Boomsma, D.I., Hulshoff Pol, H.E., 2010. Heritability of DTI and MTR in Nine-year-old children. NeuroImage 53(3), 1085-1092.

Brun, A., Knutsson, H., Park, H.J., Shenton, M.E., Westin, C.F., 2004. Clustering fiber traces using normalized cuts. 7th International Conference on Medical Image Computing and Computer-Assisted Intervention LNCS 3216, 368-375.

Catani, M., Allin, M.P., Husain, M., Pugliese, L., Mesulam, M.M., Murray, R.M., Jones, D.K., 2007. Symmetries in human brain language pathways correlate with verbal recall. Proceedings of the National Academy of Sciences 104(43), 17163-17168.

Colby, J.B., Soderberg, L., Lebel, C., Dinov, I.D., Thompson, P.M., Sowell, E.R. 2011. Along-tract statistics allow for enhanced tractography analysis. NeuroImage 59(4), 3227-3342.

Chaiken, S., 1982. A combinatorial proof of the all minors matrix tree theorem. SIAM Journal on Algebraic and Discrete Methods 3(3), 319-329.

Chiang, M.C., McMahon, K.L., de Zubicaray, G., Martin, N., Hickie, I., Toga, A., Wright, M., Thompson, P.M., 2011. Genetics of white matter development: a DTI study of 705 twins and their siblings aged 12 to 29. NeuroImage 54(3), 2308-2317.

Chou, Y.Y., Leporé, N., de Zubicaray, G.I., Rose, S.E., Carmichael, O.T., Becker, J.T., Toga, A.W., Thompson, P.M., 2007. Automatic 3D mapping & analysis of the lateral ventricles using fluid registration of multiple labeled atlases. 4th IEEE International Symposium on Biomedical Imaging: From Nano to Macro, Washington, D.C., USA, 1288-1291.

Chou, Y.Y., Leporé, N., de Zubicaray, G.I., Carmichael, O.T., Becker, J.T., Toga, A.W., Thompson, P.M., 2008. Automated ventricular mapping with multi-atlas fluid image alignment reveals genetic effects in Alzheimer's disease. NeuroImage 40(2), 615-630.

Chou, Y.Y., Leporé, N., Chiang, M.C., Avedissian, C., Barysheva, M., McMahon, K.L., de Zubicaray, G.I., Meredith, M., Wright, M.J., Toga, A.W., Thompson, P.M., 2009. Mapping genetic influences on ventricular structure in twins. NeuroImage 44(4), 1312-1323.

Cole, M.W., Yarkoni, T., Repovs, G., Anticevic, A., Braver, T.S., 2012. Global connectivity of prefrontal cortex predicts cognitive control and intelligence. Journal of Neuroscience 32(26), 8988-8999.

Conturo, T.E., Lori, N.F., Cull, T.S., Akbudak, E., Snyder, A.Z., Shimony, J.S., McKinstry, R.C., Burton, H., Raichle, M.E., 1999. Tracking neuronal fiber pathways in the living human brain. Proceedings of the National Academy of Sciences 96(18), 10422-10427.

Corouge, I., Fletcher, P.T., Joshi, S., Gouttard, S., Gerig, G., 2006. Fiber tract-oriented statistics for quantitative diffusion tensor MRI analysis. Medical Image Analysis 10(5), 786-798.

Descoteaux, M., Angelino, E., Fitzgibbons, S., Deriche, R., 2007. Regularized, fast, and robust analytical Q-ball imaging. Magnetic Resonance in Medicine 58(3), 497-510.

Daianu, M., Dennis, E.L., Jahanshad, N., Nir, T.M., Toga, A.W., Jack, C.R. Jr., Weiner, M.W., Thompson, P.M., Alzheimer's Disease NeuroImaging Initiative, 2012. Analyzing the structural *k*-core of brain connectivity networks in normal Aging and Alzheimer's disease. Novel Neuroimaging Biomarkers for Alzheimer's Disease Workshop at 15th International Conference on Medical Image Computing and Computer-Assisted Intervention, Nice, France, 52-62.

Daianu, M., Jahanshad, N., Nir, T.M., Toga, A.W., Jack, C.R. Jr., Weiner, M.W., Thompson, P.M., Alzheimer's Disease Neuroimaging Initiative, 2013. Breakdown of brain connectivity between normal aging and Alzheimer's disease: a structural k-core network analysis. Brain Connectivity 3(4), 407-422.

Dennis, E.L., Jahanshad, N., Toga, A.W., McMahon, K.L., de Zubicaray, G.I., Martin, N.G., Wright, M.J., Thompson, P.M., 2012. Test-retest reliability of graph theory measures of structural brain connectivity. 15th International Conference on Medical Image Computing and Computer-Assisted Intervention, Nice, France, LNCS 7512, 305–312.

Ding, Z., Gore, J.C., Anderson, A.W., 2003. Classification and quantification of neuronal fiber pathways using diffusion tensor MRI. Magnetic Resonance in Medicine 49(4), 716-721.

Falconer D. and Mackay, T.F., 1996. Introduction to quantitative genetics, 4th ed. Benjamin Cummings.

Fletcher, E., Raman, M., Huebner, P., Liu, A., Mungas, D., Carmichael, O., DeCarli, C., 2013. Loss of fornix white matter volume as a predictor of cognitive impairment in cognitively normal elderly individuals. JAMA Neurology 70(11), 1389-1395.

Gerig, G., Gouttard, S., Corouge, S., 2004. Analysis of brain white matter via fiber tract modeling. 26th Annual International Conference of IEEE Engineering in Medicine and Biology Society 6, 4421-4424.

Guevara, P., Duclap, D., Poupon, C., Marrakchi-Kacem, L., Fillard, P., Le Bihan, D., Leboyer, M., Houenou, J., Mangin, J.F., 2012. Automatic fiber bundle segmentation in massive tractography datasets using a multi-subject bundle atlas. NeuroImage 61(4), 1083-1099.

Heckemann, R.A., Hajnal, J.V., Aljabar, P., Rueckert, D., Hammers, A., 2006. Automatic anatomical brain MRI segmentation combining label propagation and decision fusion. NeuroImage 33(1), 115-126.

Hofer, S. and Frahm, J., 2006. Topography of the human corpus callosum revisited – comprehensive fiber tractography using diffusion tensor magnetic resonance imaging. NeuroImage 32(3), 989-994.

Holmes, C.J., Hoge, R., Collins, L., Woods, R., Toga, A.W., Evans, A.C., 1998. Enhancement of MR images using registration for signal averaging. Journal of Computer Assisted Tomography 22(2), 324-333.

Hulshoff Pol, H.E., Schnack, H.G., Posthuma, D., Mandl, R.C.W., Baaré, W.F., van Oel, C., van Haren, N.E.M., Collins, D.L., Evans,A.C., Amunts, K., Bürgel, U., Zilles, K., de Geus, E.J., Boomsma, D.I., Kahn, R.S., 2006. Genetic contributions to human brain morphology and intelligence. Journal of Neuroscience 26(40), 10235-10242.

Ingalhalikar, M., Smith, A., Parker, D., Satterthwaite, T.D., Elliott, M.A., Ruparel, K., Hakonarson, H., Gur, R.E., Gur, R.C., Verma, R., 2013. Sex differences in the structural connectome of the human brain. Proceedings of the National Academy of Sciences of the United States of America, doi:10.1073/pnas.1316909110.

Jahanshad, N., Lee, A.D., Barysheva, M., McMahon, K.L., de Zubicaray, G.I., Martin, N.G., Wright, M.J., Toga, A.W., Thompson, P.M., 2010. Genetic influences on brain asymmetry: a DTI study of 374 twins and siblings. NeuroImage 52(2), 455-469.

Jahanshad, N., Aganj, I., Lenglet, C., Joshi, A., Jin, Y., Barysheva, M., McMahon, K.L., de Zubicaray, G.I., Martin, N.G., Wright, M.J., Toga, A.W., Sapiro, G., Thompson, P.M., 2011. Sex differences in the human connetome: 4-Tesla high angular resolution diffusion imaging (HARDI) tractography in 234 young adult twins. 14th Congress of IEEE International Symposium on Biomedical Imaging: From Nano to Macro, Chicago, IL, USA, 939-943.

Jahanshad, N., Valcour, V.G., Nir, T.M., Kohannim, O., Busovaca, E., Nicolas, K., Thompson, P.M., 2012a. Disrupted brain networks in the aging HIV+ population. Brain Connectivity 2(6), 335-344.

Jahanshad, N., Prasad, G., Toga, A.W., McMahon, K.L., de Zubicaray, G.I., Martin,N.G.,Wright, M.J., Thompson, P.M., 2012b. Genetics of path lengths in brain connectivity networks: HARDI-based maps in 457 adults. Multimodal Brain Image Analysis Workshop at 15th International Conference on Medical Image Computing and Computer-Assisted Intervention, LNCS 7509, 29-40.

Jahanshad, N., Kochunov, P.V., Sprooten, E., Mandl, R.C., Nichols, T.E., Almasy, L., Blangero, J., Brouwer, R.M., Curran, J.E., de Zubicaray, G.I., Duggirala, R., Fox, P.T., Hong, L.E., Landman, B.A., Martin, N.G., McMahon, K.L., Medland, S.E., Mitchell, B.D., Olvera, R.L., Peterson, C.P., Starr, J.M., Sussmann, J.E., Toga, A.W., Wardlaw, J.M., Wright, M.J., Hulshoff Pol, H.E., Bastin, M.E., McIntosh, A.M., Deary, I.J., Thompson, P.M., Glahn, D.C., 2013. Multi-site genetic analysis of diffusion images and voxelwise heritability analysis: a pilot project of the ENIGMA–DTI working group. NeuroImage 81, 455-469.doi:10.1016/j.neuroimage.2013.04.061.

Jahanshad, N., Kochunov, P., Nichols, T.E., Sprooten, E., Mandl, R.C., Almasy, L., Brouwer, R.M., Curran, J.E., de Zubicaray, G.I., Dimitrova, R., Duggirala, R., Fox, P.T., Hong, L.E., Landman, B.A., Lemaitre, H., Lopez, L., Martin, N.G., McMahon, K.L., Mitchell, B.D., Olvera,

R.L., Peterson, C.P., Starr, J.M., Sussmann, J.E., Toga, A.W., Wardlaw, J.M., Wright, M.J., Wright, S.N., Bastin, M.E., McIntosh, A.M., Boomsma, D.I., Kahn., R.S., Braber, A.den, de Geus, E.J.C., Deary, I.J., Hulshoff Pol, H.E., Williamson, D., Blangero, J., van 't Ent, D., Glahn, D.C., Thompson, P.M., 2014. Combining meta- and mega- analytic approaches for multi-site diffusion imaging based genetic studies: from the ENIGMA-DTI working group. 11th IEEE International Symposium on Biomedical Imaging: From Nano to Macro, Beijing, China, in press.

Jin, Y., Shi, Y., Jahanshad, N., Aganj, I., Sapiro, G., Toga, A.W., Thompson, P.M., 2011a. 3D elastic registration improves HARDI-derived fiber alignment and automated tract clustering. 8th IEEE International Symposium on Biomedical Imaging: From Nano to Macro, Chicago, IL, USA, 822-826.

Jin, Y., Shi, Y., Joshi, S.H., Jahanshad, N., Zhan, L., de Zubicaray, G.I., McMahon, K.L., Martin, N.G., Wright, M.J., Toga, A.W., Thompson, P.M., 2011b. Heritability of white matter fiber tract shapes: a HARDI study of 198 twins. Multimodal Brain Image Analysis Workshop at 14th International Conference on Medical Image Computing and Computer-Assisted Intervention, LNCS 7012, 35-43.

Jonasson, L., Hagmann, P., Thiran, J.P., Wedeen, V.J., 2004. Fiber tracts of high angular resolution diffusion MRI are easily segmented with spectral clustering. 13th Annual Meeting of International Society for Magnetic Resonance in Medicine, Miami, FL, USA.

Kochunov, P., Glahn, D.C., Nichols, T.E., Winkler, A.M., Hong, E.L., Holcomb, H.H., Stein, J.L., Thompson, P.M., Curran, J.E., Carless, M.A., Olvera, R.L., Johnson, M.P., Cole, S.A., Kochunov, V., Kent, J., Blangero, J., 2011. Genetic analysis of cortical thickness and fractional anisotropy of water diffusion in the brain. Frontiers in Neuroscience 5, article 120.

Klingberg, T., Hedehus, M., Temple, E., Salz, T., Gabrieli, J.D., Moseley, M.E., Poldrack, R.A., 2000. Microstructure of temporo-parietal white matter as a basis for reading ability: evidence from diffusion tensor magnetic resonance imaging. Neuron 25(2), 493-500.

Lazar, M., Weinstein, D.M., Tsuruda, J.S., Hasan, K.M., Arfanakis, K., Meverand, M.E., Badie, B., Rowley, H.A., Haughton, V., Field, A., Alexander, A.L., 2003. White matter tractography using diffusion tensor deflection. Human Brain Mapping 18(4), 306-321.

LeBihan, D., Breton, E., Lallemand, D., Grenier, P., Cabanis, E., Laval-Jeantet, M., 1986. MR imaging of intravoxel incoherent motions: application to diffusion and perfusion in neurologic disorders. Radiology 161(2), 401-407.

Lee, A.D., Lepore, N., de Leeuw, J., Brun, C.C., Barysheva, M., McMahon, K.L., de Zubicaray, G.I., Martin, N.G., Wright, M.J., Thompson, P.M., 2010. Multivariate variance-components

analysis in DTI. 13th IEEE International Symposium on Biomedical Imaging: From Nano to Macro, Rotterdam, The Netherlands, 1157-1160.

Leow, A.D., Yanovsky, I., Chiang, M.C., Lee, A.D., Klunder, A.D., Lu, A., Becker, J.T., Davis, S.W., Toga, A.W., Thompson, P.M., 2007. Statistical properties of Jacobian maps and the realization of unbiased large-deformation nonlinear image registration. IEEE Transactions on Medical Imaging 26(6), 822-832.

Leporé, N., Chou, Y.Y., Lopez, O.L., Aizenstein, H.J., Becker, J.T., Toga, A.W., Thompson, P.M., 2008a. Fast 3D fluid registration of brain magnetic resonance images. Proceedings of the international society for optics and photonics (SPIE) – Medical Imaging, 6916, article ID. 69160Z, doi:10.1117/12.774338.

Leporé, N., Brun, C.C., Chou, Y.Y., Lee, A.D., Barysheva, M., de Zubicaray, G.I., Meredith, M., McMahon, K., Wright, M.J., Toga, A.W., Thompson, P.M., 2008b. Multi-atlas tensor-based morphometry and its application to a genetic study of 92 twins. Mathematical Foundations of Computational Anatomy Workshop at 11th International Conference on Medical Image Computing and Computer-Assisted Intervention, New York, NY, USA.

Leporé, N., Brun, C.C., Descoteaux, M., Lee, A.D., Barysheva, M., Chou, Y.Y., de Zubicaray, G.I., McMahon, K., Wright, M.J., Martin, N.G., Gee, J.C., Thompson, P.M., 2010. A multivariate group-wise genetic analysis of white matter integrity using orientation distribution function. Computational Diffusion MRI Workshop at 13th International Conference on Medical Image Computing and Computer-Assisted Intervention, Beijing, China.

Li, H., Xue, Z., Guo, L., Liu, T., Hunter, J., Wong, S.T., 2010. A hybrid approach to automatic clustering of white matter fibers. NeuroImage 49(2), 1249-1258.

Lötjönen, J.M., Wolz, R., Koikkalainen, J.R., Thurfjell, L., Waldemar, G., Soininen, H., Rueckert, D.; Alzheimer's Disease Neuroimaging Initiative, 2010. Fast and robust multi-atlas segmentation of brain magnetic resonance images. NeuroImage 49(3), 2352-2365.

Maddah, M., Grimson, W.E.L., Warfield, S.K., Wells, W.M., 2008. A unified framework for clustering and quantitative analysis of white matter fiber tracts. Medical Image Analysis 12(2), 191-202.

Merboldt, K.D., Hanicke, W., Frahm, J., 1985. Self-diffusion NMR imaging using stimulated echoes. Journal of Magnetic Resonance 64(3), 479-486.

Morra, J.H., Tu, Z., Apostolova, L.G., Green, A.E., Avedissian, C., Madsen, S.K., Parikshak, N., Hua, X., Toga, A.W., Jack, C.R. Jr., Weiner, M.W., Thompson, P.M., Alzheimer's Disease Neuroimaging Initiative, 2009. Validation of a fully automated 3D hippocampal segmentation method using subjects with Alzheimer's disease mild cognitive impairment, and elderly controls. NeuroImage 43(1), 59-68.

Mori, S., Crain, B.J., Chacko, V. P., Van Zijl, P.C.M., 1999. Three-dimensional tracking of axonal projections in the brain by magnetic resonance imaging. Annals of Neurology 45(2), 265-269.

Nir, T.M., Jahanshad, N., Villalon-Reina, J.E., Toga, A.W., Jack, C.R. Jr., Weiner, M.W., Thompson, P.M.; Alzheimer's Disease Neuroimaging Initiative (ADNI), 2013. Effectiveness of regional DTI measures in distinguishing Alzheimer's disease, MCI, and normal aging. NeuroImage Clinical 3, 180-195.

O'Donnell, L.J., Kubicki, M., Shenton, M.E., Dreusicke, M.H., Grimson, W.E., Westin, C.F., 2006. A method for clustering white matter fiber tracts. American Journal of Neuroradiology 25(5), 1032-1036.

O'Donnell L.J. and Westin, C.F., 2007. Automatic tractography segmentation using a high-dimensional white matter atlas. IEEE Transactions on Medical Imaging 26(11), 1562-1575.

Oishi, K., Faria, A., Jiang, H., Li, X., Akhter, K., Zhang, J., Hsu, J.T., Miller, M.I., van Zijl, P.C., Albert, M., Lyketsos, C.G., Woods, R., Toga, A.W., Pike, G.B., Rosa-Neto, P., Evans, A., Mazziotta, J., Mori, S., 2009. Atlas-based whole brain white matter analysis using large deformation diffeomorphic metric mapping: application to normal elderly and Alzheimer's disease participants. NeuroImage 46(2), 486-499.

Oishi, K., Mielke, M.M., Albert, M., Lyketsos, C.G., Mori, S., 2012. The fornix sign: a potential sign for Alzheimer's disease based on diffusion tensor imaging. Journal of Neuroimaging 22(4), 365-374.

Parker, G.J.M. and Alexander, D.C., 2003a. Probabilistic monte carlo based mapping of cerebral connections utilising whole-brain crossing fibre information. Information Processing in Medical Imaging, LNCS 2732, 684-695.

Parker, G.J.M., Haroon, H.A., Wheeler-Kingshott, C.A.M., 2003b. A framework for a streamline-based probabilistic index of connectivity (PICo) using a structural interpretation of MRI diffusion measurements. Journal of Magnetic Resonance Imaging 18(2), 242-254.

Prasad, G., Jahanshad, N., Aganj, I., Lenglet, C., Sapiro, G., Toga, A.W., Thompson, P.M., 2011. Atlas-based fiber clustering for multi-subject analysis of high angular resolution diffusion imaging tractography. 14th IEEE International Symposium on Biomedical Imaging: From Nano to Macro, Chicago, IL, USA, 276-280.

Price, G., Cercignani, M., Parker, G.J., Altmann, D.R., Barnes, T.R., Barker, G.J., Joyce, E.M., Ron, M.A., 2007. Abnormal brain connectivity in first-episode psychosis: a diffusion MRI tractography study of the corpus callosum. NeuroImage 35(2), 458-466.

Price G, Cercignani, M, Parker, G.J., Altmann, D.R., Barnes, T.R., Barker, G.J., Joyce, E.M., Ron, M.A., 2008. White matter tracts in first-episode psychosis: a DTI tractography study of the uncinate fasciculus. NeuroImage 39(3), 949-955.

Rohlfing, T., Russakoff, D.B., Maurer, C.R. Jr., 2004. Performance-based classifier combination in atlas-based image segmentation using expectation-maximization parameter estimation. IEEE Transactions on Medical Imaging 23(8), 983-994.

Sabuncu, M.R., Yeo, B.T., Van Leemput, K., Fischl, B., Golland, P., 2010. A generative model for image segmentation based on label fusion. IEEE Transactions on Medical Imaging 29(10), 1714-1729.

Smith, S.M., Johansen-Berg, H., Jenkinson, M., Rueckert, D., Nichols, T.E., Miller, K.L., Robson, M.D., Jones, D.K., Klein, J.C., Bartsch, A.J., Behrens, T.E., 2007. Acquisition and voxelwise analysis of multi-subject diffusion data with tract-based spatial statistics. Nature Protocols 2(3), 499-503.

Supekar, K., Menon, V., Rubin, D., Musen, M., Greicius, M.D., 2008. Network analysis of intrinsic functional brain connectivity in Alzheimer's disease. PLOS Computational Biology 4(6), doi:10.1371/journal.pcbi.1000100.

Studholme, C., 2007. Incorporating DTI data as a constraint in deformation tensor morphometry between T1 MR images. 20th International Conference on Information Processing in Medical Imaging, Kerkrade, The Netherlands, LNCS 4584, 223-232.

Taylor, D.G. and Bushell, M.C., 1985. The spatial mapping of translational diffusion coefficients by the NMR imaging technique. Physics in Medicine and Biology 30(4), 345-349.

Teipel, S.J., Stahl, R., Dietrich, O., Schoenberg, S.O., Pemeczky, R., Bokde, A.L., Reiser, M.F., Möller, H.J., Hampel, H., 2007. Multivariate network analysis of fiber tract integrity in Alzheimer's disease. NeuroImage 34(3), 985-995.

Thiebaut de Schotten, M., Ffytche, D.H., Bizzi, A., Dell'Acqua, F., Allin, M., Walshe, M., Murray, R., Williams, S.C., Murphy, D.G., Catani, M., 2011. Atlasing location, asymmetry and inter-subject variability of white matter tracts in the human brain with MR diffusion tractography. Neuroimage 54(1), 49-59.

Thompson, P.M., Cannon, T.D., Narr, K.L., van Erp, T., Poutanen, V.P., Huttunen, M., Lönnqvist, J., Standertskjöld-Nordenstam, C.G., Kaprio, J., Khaledy, M., Dail, R., Zoumalan, C.I., Toga, A.W., 2001. Genetic influence on brain structure. Nature Neuroscience 4, 1253-1258.

Thomason, M.E. and Thompson, P.M., 2011. Diffusion imaging, white matter, and psychopathology. Annual Review of Clinical Psychology 7, 63-85.

Tournier, J.D., Calamante, F., Gadian, D.G., Connelly, A., 2004. Direct estimation of the fiber orientation density function from diffusion-weighted MRI data using spherical deconvolution. NeuroImage 23(3), 1176-1185.

Tsai, A., Westin, C.F., Hero, A.O., Willsky, A.S., 2007. Fiber tract clustering on manifolds with dual rooted-graphs. IEEE International Conference on Computer Vision and Pattern Recognition, Minneapolis, MN, USA, 1-6.

Tuch, D., 2004. Q-ball imaging. Magnetic Resonance in Medicine 52(6), 1358-1372.

Tutte, W.T., 2001. Graph theory. Cambridge University Press.

Visser, E., Nijhuis, E.H., Buitelaar, J.K., Zwiers, M.P., 2011. Partition-based mass clustering of tractography streamlines. NeuroImage 54(1), 303-312.

Von Luxburg, U., 2007. A tutorial on spectral clustering. Statistics and Computing 17(4), 395-416.

Wakana, S., Caprihan, A., Panzenboeck, M.M., Fallon, J.H., Perry, M., Gollub, R.L., Hua, K., Zhang, J., Jiang, H., Dubey, P., Blitz, A., van Zijl, P., Mori, S., 2007. Reproducibility of quantitative tractography methods applied to cerebral white matter. NeuroImage 36(3), 630-644.

Wang, Q., Yap, P.T., Wu, G., Shen, D., 2012. Application of neuroanatomical features to tractography clustering. Human Brain Mapping. doi:10.1002/hbm.22051.

Wassermann, D., Descoteaux, M., Deriche, R., 2008. Diffusion maps clustering for magnetic resonance *q*-ball imaging segmentation. International Journal of Biomedical Imaging 2008:526906. doi:10.1155/2008/526906.

Wassermann, D., Bloy, L., Kanterakis, E., Verma, R., Deriche, R., 2010. Unsupervised white matter fiber clustering and tract probability map generation: applications of a Gaussian process framework for white matter fibers. NeuroImage 51(1), 228-241.

Wedeen, V.J., Hagmann, P., Tseng, W.Y., Reese, T.G., Weisskoff, R.M., 2005. Mapping complex tissue architecture with diffusion spectrum magnetic resonance imaging. Magnetic Resonance in Medicine 54(6), 1377-1386.

Wright, I.C., Sham, P., Murray, R.M., Weinberger, D.R., Bullmore, E.T., 2002. Genetic contribution to regional variability in human brain structure: methods and preliminary results. NeuroImage 17(1), 256-271.

Xia, Y., Turken, A.U., Whitfield-Gabrieli, S.L., Gabrieli, J.D., 2005. Knowledge-based classification of neuronal fibers in entire brain. 8th International Conference on Medical Image Computing and Computer-Assisted Intervention, LNCS 3749, 205-212.

Yushkevich, P.A., Zhang, H., Simon, T.J., Gee, J.C., 2008. Structure-specific statistical mapping of white matter tracts. NeuroImage 41(2), 448-461.

Zalesky, A., Fornito, A., Harding, I.H., Cocchi, L., Yücel, M., Pantelis, C., Bullmore, E.T., 2010. Whole-brain anatomical networks: does the choice of nodes matter? NeuroImage 50(3), 970-983.

Zalesky, A. and Fornito, A., 2009. A DTI-derived measure of cortico-cortical connectivity. IEEE Transactions on Medical Imaging 28(7), 1023-1036.

Zhan, L., Leow, A.D. ; Aganj, I.; Lenglet, C.; Sapiro, G.; Yacoub, E.; Harel, N.; Toga, A.W.; Thompson, P.M., 2011. Differential information content in staggered multiple shell HARDI measured by the tensor distribution function. 8th IEEE International Symposium on Biomedical Imaging: From Nano to Macro, Chicago, IL, USA, 305-209.

Zhang, Y., Zhang, J., Oishi, K., Faria, A.V., Jiang, H., Li, X., Akhter, K., Rosa-Neto, P., Pike, G.B., Evans, A., Toga, A.W., Woods, R., Mazziotta, J.C., Miller, M.I., van Zijl, P.C.M., Mori, S., 2010. Atlas-guided tract reconstruction for automated and comprehensive examination of the white matter anatomy. NeuroImage 52(4), 1289-1301.

Ziyan, U., Sabuncu, M.R., Grimson, W.E., Westin, C.F., 2009. Consistency clustering: a robust algorithm for group-wise registration, segmentation and automatic atlas construction in diffusion MRI. International Journal of Computer Vision 85(3), 279-290.